UNIVERSITÀ DEGLI STUDI DI PALERMO

Scuola Politecnica

Dottorato congiunto in Information and Communication Technologies

Dipartimento di Ingegneria

Settore Scientifico Disciplinare ING-INF01

Doctorat en cotutelle en sciences de l'énergie et des matériaux de l'INRS

TAPERING RESONANT NANOANTENNAS FOR ENHANCED THz LIGHT – NANOMATTER INTERACTIONS

IL DOTTORE

VINCENZO AGLIERI

LA COORDINATRICE

PROF.SSA ILENIA TINNIRELLO

IL TUTOR UNIPA

PROF. ROBERTO MACALUSO

IL TUTOR INRS

PROF. LUCA RAZZARI

IL TUTOR IIT

DR. ANDREA TOMA

CICLO XXXI – ANNO 2020

To my family

To all the people who fought and fight SARS-CoV-2

The unexamined life is not worth living
Plato, Apology of Socrates, 38a

ACKNOWLEDGEMENTS

First and foremost, I would like to thanks my three supervisors in the frame of the joint Ph.D. Program between the Institut National de la Recherche Scientifique - Énergie Matériaux Télécommunications (INRS-EMT) and Università degli Studi di Palermo (UniPa). I thank Prof. Luca Razzari from INRS-EMT for his invaluable support and constant guidance during my PhD period. He did not only transfer to me plasmonics concepts as part of his impressively wide knowledge on science but he also gave me the priceless opportunity to develop my passion for nanotechnology and nanofabrication. I thank Dr. Andrea Toma from Istituto Italiano di Tecnologia (IIT) that introduced me to the world of device fabrication; he taught me everything I know about technology making me a Process Engineer. Through his daily supervision, he concurred in further widening my knowledge about plasmonics and terahertz technology. I thank Dr. Roberto Macaluso from UniPa for accompanying me in the prosecution of my studies in this prestigious joint Ph.D. Program and for guiding me during my research in the master period and in pursue the research about memristors during the Ph.D. Thanks to him, today I can claim scientific publications on this field.

I would like to thank Prof. Roberto Morandotti from INRS-EMT and Prof. Alessandro Busacca from UniPa for their tremendous efforts in the organization and the establishment of the joint PhD Program between INRS and UniPa. Along with them, I would thank Dr. Francesco De Angelis for welcoming me in the facilities of IIT.

I obviously thank all the people who accompanied me during these Ph.D. years. My colleagues from INRS, Xin Jin, with whom I shared research and hard work, who helped me in the simulations, Andrea Rovere for his precious help on the characterization of the devices, Riccardo Piccoli, who gave me strenuous and fundamental help in many aspects of my research, as well as Younggyun Jeong, Diego Caraffini, Luca Zanotto, Atiye Pezeshki, Roya Mohajeri, Yuechen Jia, Giacomo Balistreri and Fuyong Yue. My colleagues from IIT, Vincenzo Caligiuri, Andrea Cerea, Marco Contardi, Marta d'Amora, Beatriz Martín-García, Marco Elvino Miali, Mario Miscuglio, Davide Spirito, and the amazing IIT staff: Marina Antonini, Claudio Biagini, Alessandro Bosca, Riccardo Carzino, Luca Goldoni, Marco Leonicini, Giorgio Mancini, Fabio Moia, Mirko Prato, Eliana Rondanina and Marco Salerno. The colleagues and Professors from UniPa, Claudio Calì, Alfonso Carmelo Cino, Isodiana Crupi, Francesco Di Franco, Giuseppe Lullo, Mauro Mosca, Monica Santamaria, Ilenia Tinnirello and Andrea Zaffora.

I thank the administrative staff at INRS-EMT, IIT and UniPa, and I wish to acknowledge for the financial support the Natural Sciences and Engineering Research Council of Canada (NSERC) for the program CREATE: Guided Light.

Finally, I would also say to all the people who were not mentioned here by mistake or by forgetfulness that I sincerely apologize for that and with as much sincerity I thank all of you.

RÉSUMÉ

Au cours des dernières décennies, la technologie Terahertz (THz) est devenue un domaine de recherche fructueux grâce à la promesse d'applications exceptionnelles. L'industrie, la biologie, la médecine et l'ingénierie ne sont qu'une partie des secteurs technologiques à la recherche de nouvelles avancées technologiques. Un tel intérêt trépidant, naît des propriétés particulières et uniques des ondes THz, telles que le caractère non ionisant, l'opacité de nombreux matériaux généralement transparents dans d'autres gammes de fréquences et le potentiel offert, entre autres, pour les technologies de l'information. Une des applications les plus prometteuses est la spectroscopie. En fait, des nombreux matériaux et composés présentent des caractéristiques d'excitation élémentaires dans le régime THz. Pendant de nombreuses années, de telles caractéristiques n'ont pas pu être étudiées en raison de la faible efficacité avec laquelle la longue longueur d'onde associée au rayonnement THz (~300 µm à 1 THz) interagit avec des objets de taille nanométrique (~10 nm). Cependant, grâce aux antennes plasmoniques, capables de localiser la lumière dans des volumes inférieurs à la longueur d'onde, il est possible de faire interagir l'onde THz avec les nanoparticules. Un tel procédé améliore considérablement l'efficacité de l'absorption de nanoparticules, permettant de récupérer des informations spectroscopiques de matières auparavant inaccessibles. De plus, des expériences d'interaction lumière-matière sont maintenant possibles dans le régime THz donnant accès, par exemple, à des études de couplage lumière-matière. Néanmoins, les performances des antennes plasmoniques peuvent encore être améliorées pour augmenter l'amélioration de champ et le volume de mode, ce qui, à son tour, accroît l'efficacité de la détection des impacts et du couplage lumière-matière. Dans cette thèse, une stratégie est présentée pour améliorer les performances de THz nanoantenne (NA) en termes d'amélioration de champ proche et de volume de mode. Tout d'abord, j'ai démontré qualitativement, par le biais d'un modèle quasi-analytique, qu'en augmentant de manière appréciable le champ proche à la pointe, il est possible d'obtenir une augmentation sensible du champ proche à la pointe. La méthode est également validée par le biais de simulations approfondies avec la méthode des éléments finis, dans lesquelles des paires NA coniques, appelées antennes «bowtie», en or, résonant à 1 THz et couplées par un intervalle de 30 nm (le gap), montrent un champ proche amélioré de plus de deux fois et un volume de mode réduit de sept fois dans l'espace lorsqu'il est effilé avec un angle de conicité optimal. Cinq échantillons à différents angles de conicité ont été fabriqués et caractérisés pour valider expérimentalement cette méthode. Les caractérisations par spectroscopie dans le domaine temporel THz (THz-TDS) ont révélé un bon accord avec les résultats de la simulation, confirmant la validité des études théoriques. Dans la dernière partie de cette thèse, nous montrons comment cette méthode peut être

efficacement utilisée pour réaliser des NAs en forme de lune (moon antennes), convenant à des expériences de couplage fort améliorées. De plus, il est également démontré numériquement l’applicabilité plus large de cette méthode dans la gamme de fréquences infrarouges (IR) et pour antennes fabriquée avec des matériaux alternatifs à l'or.

Mots-clés: nanoantennes, science et technologie térahertz, interaction renforcée lumière-matière.

SOMMARIO

Nel corso degli ultimi decenni la tecnologia terahertz (THz) è diventata un fruttuoso campo di ricerca grazie alla spinta ricevuta dal desiderio di sfruttarne le promettenti applicazioni in questa porzione dello spettro elettromagnetico. La biologia, la medicina e l'ingegneria sono soltanto alcuni dei settori che guardano con interesse alle ultime scoperte nella ricerca sulle onde THz. Questo enorme interesse nasce dalle peculiari proprietà di tali onde, come ad esempio: il carattere non ionizzante, l'opacità di svariati materiali solitamente trasparenti in altri intervalli di frequenze e per le potenziali ricadute positive nel campo della tecnologia dell'informazione. Una fra le applicazioni più interessanti consiste nell'uso delle onde THz per la spettroscopia. Infatti molti materiali presentano delle risonanze in questo campo di radiazione, e il loro studio darebbe accesso a molte e preziose informazioni che potrebbero svelare proprietà della materia ancora sconosciute. Per molti anni, tali risonanze non sono state studiate a causa della relativamente grande lunghezza d'onda corrispondente alla radiazione THz (~300 μm a 1 THz) da cui conseguiva una scarsa efficienza di accoppiamento con oggetti di dimensioni nanometriche. Tuttavia grazie alle antenne plasmoniche, che sono in grado di localizzare la luce assorbita in uno spazio il cui volume è inferiore alla lunghezza d'onda coinvolta, noto come volume modale, è possibile far interagire le onde THz con delle nano-particelle. Tale metodo ha migliorato a tal punto l'efficienza di assorbimento delle nano-particelle della radiazione THz che è stato reso possibile recuperare informazioni spettroscopiche della materia a cui prima non si aveva accesso. Inoltre grazie a questa tecnica è possibile effettuare proficuamente molti altri esperimenti nel regime THz, come ad esempio quelli sull'accoppiamento forte tra radiazione e materia. Cionondimeno le prestazioni delle antenne plasmoniche non sono ottimali e possono essere ulteriormente migliorate per aumentare il "*field enhancement*", cioè il tasso di incremento del campo elettrico ottenuto dal confinamento generato dalle antenne plasmoniche all'interno del volume modale, che a sua volta influisce fortemente sull'efficienza e la qualità degli esperimenti nel regime THz. In questa tesi viene presentata una strategia per il miglioramento delle prestazioni di nano-antenne (NA) THz sia in termini di *field enhancement* che di volume modale. Tale strategia consiste nell'attenta rastremazione di NA cilindriche in oro, così da formare dei coni troncati. Per prima cosa, mostro attraverso un modello quasi-analitico che tale strategia, per mezzo di un angolo *ottimo* di rastremazione, permette di ottenere un miglioramento considerevole delle prestazioni. Successivamente il metodo di rastremazione delle antenne viene validato attraverso l'uso di un simulatore software, col quale vengono simulate coppie di antenne a diversi angoli di rastremazione, separate da un gap di 30 nm e risonanti attorno a 1 THz. Da tale studio si trova che in corrispondenza dell'angolo *ottimo*, le NA rastremate mostrano il

doppio di *field enhancement* e un volume modale sette volte inferiore a quello offerto da una antenna non rastremata. Lo stesso software è utilizzato per ricavare il design di cinque campioni per la fabbricazione. Su tali campioni è stata eseguita una caratterizzazione ottica nel THz attraverso un sistema di spettroscopia THz nel dominio del tempo (THz-TDS), e il risultato è in accordo con i risultati simulati ottenuti durante il design degli stessi, confermando la validità degli studi teorici. Nell'ultima parte di questa tesi viene mostrata anche l'applicazione di questo metodo per il miglioramento della risposta delle antenne *moon* (caratterizzate da una geometria alternativa a forma di luna) realizzate nell'ambito di esperimenti di accoppiamento forte radiazione-materia. Inoltre lo stesso metodo viene qui mostrato essere valido anche in altri regimi di frequenza, in particolare nell'infrarosso.

Parole chiave: nano-antenne, scienza e tecnologia terahertz, interazione radiazione-materia migliorata.

ABSTRACT

In the last decades, Terahertz (THz) technology has become a fruitful research field thanks to the promise of outstanding applications. Industry, biology, medicine and engineering are only a part of the technological sectors looking into THz researches for the latest advances. Such hectic interest born from the peculiar and unique properties of the THz waves, such as the non-ionizing character, the transparency of many materials usually opaque in other frequency ranges, and the potentiality offered for information technologies, among others. One of the most promising application is spectroscopy. In fact, many materials and compounds present elementary excitation features in the THz regime. For many years, such features could not be exploited with nanosystems because of the poor efficiency with which the long wavelength associated to THz radiation (~300 μm at 1 THz) interacts with nano-sized objects (~10 nm). However, thanks to plasmonic antennas, capable of localizing light in sub-wavelength volumes, it has become possible to make the long THz wave interacting with nano-particles. Such method greatly enhances nano-particle absorption allowing to retrieve spectroscopic information of nanomatter previously not accessible. Moreover, light-nanomatter interaction experiments are now possible in THz regime giving access to, e.g., strong THz light-nanomatter coupling studies. Nevertheless, the performance of plasmonic antennas can be still improved to increase the field enhancement and reduce the mode volume, which in turn impact sensing and light-matter coupling efficiency. In this thesis, a strategy is presented to improve THz nanoantenna (NA) performance in terms of near field enhancement and mode volume reduction. First, I qualitatively show through a quasi-analytical model that by judiciously tapering gold NAs, an appreciable increase of the near field at the tip can be achieved. The method is also validated through extensive finite element method simulations, where gold bow-tie NA pairs, resonating at 1 THz and coupled by a 30-nm-wide gap, show a more than two-fold enhanced near field and a seven-fold reduced mode volume in the gap when tapered with an optimum angle. Five samples at different tapering angles have been fabricated and characterized to experimentally validate such method. The THz time domain spectroscopy (THz-TDS) characterizations revealed a good agreement with the simulation results, confirming the validity of the theoretical studies. In the last part of this thesis, it is shown how this method can be effectively extended to other geometries, in particular to realize “moon-shaped” NAs suitable for improved strong coupling experiments. Moreover, it is also numerically demonstrated the applicability of this method to higher frequencies, up to the infrared (IR) range.

Keywords: nanoantennas, terahertz science and technology, enhanced light-matter interaction.

TABLE OF CONTENTS

LIST OF FIGURES

LIST OF ABBREVIATIONS

THz	Terahertz
THz-TDS	Terahertz – Time Domain Spectroscopy
IR	Infrared
NA	Nanoantenna
CdSe	Cadmium Selenide
CdS	Cadmium Sulphide
SERS	Surface-Enhanced Raman Spectroscopy
SEIRA	Surface-Enhanced Infrared Absorption
ITO	Indium Tin Oxide
TM	Transverse Magnetic
TE	Transverse Electric
LSPR	Localized Surface Plasmon Resonance
FR	Fröhlich
FEM	Finite Element Method
PMMA	Poly(methyl methacrylate)
MIKB	Methyl isobutyl ketone
IPA	Isopropyl alcohol
rpm	round per minute
KOH	Potassium hydroxide
SEM	Scanning Electron Microscope
GaP	Gallium Phosphide
BS	Beam Splitter
OPM	Off-axis Parabolic Mirror
QWP	Quarter Wave-Plate
WP	Wollaston Prism
BPD	Balanced Photo-Detector

FWHM	Full Width at Half Maximum
TERS	Tip-Enhanced Raman Characterization

LIST OF PUBLICATIONS
(DURING THE DOCTORAL PERIOD)

Publications related to this Thesis work

Papers in refereed journals

1. **V. Aglieri**, X. Jin, A. Rovere, R. Piccoli, D. Caraffini, S. Tuccio, F. De Angelis, R. Morandotti, R. Macaluso, A. Toma, and L. Razzari, "Improving nanoscale terahertz field localization by means of sharply tapered resonant nanoantennas," **Nanophotonics**, 9(3), pp. 683-690 (2020)
2. X. Jin**†**, **V. Aglieri†**, et al., "Vibrational Strong Coupling between Semiconducting Nanocrystals and Moon-Shaped Nanoantennas," *in preparation*, **† Equal Contribution**

Refereed International Conferences

1. **V. Aglieri**, X. Jin, A. Rovere, R. Piccoli, R. Morandotti, R. Macaluso, A. Toma, and L. Razzari, "Antenna Tapering Strategy for Near-Field Enhancement Optimization in Terahertz Gold Nanocavities," CLEO/EUROPE-EQEC 2019, Munich, Germany (2019). *Oral Presentation*
2. **V. Aglieri**, G. Lullo, M. Mosca, R. Macaluso, U. Lo Cicero, A. Zaffora, F. Di Franco, M. Santamaria, and L. Razzari, "Forming-free and self-rectifying resistive switching effect in Anodic Titanium Dioxide-based Memristors," IEEE 4th International Forum on *Research and Technologies for Society and Industry* (RTSI), Palermo, Italy (2018). *Oral Presentation*
3. **V. Aglieri**, X. Jin, A. Rovere, R. Piccoli, A. Cerea, F. De Angelis, R. Morandotti, R. Macaluso, A. Toma, and L. Razzari, "Near-Field Enhancement Optimization by Tapering Terahertz Gold Nanoantennas," Photonic North 2018 IEEE. Montreal, Quebec, Canada (2018). *Oral Presentation*
4. G. Balistreri, A. Tomasino, **V. Aglieri**, R. Piccoli, C. Foucher, A. Markov, S. Stivala, A. Busacca, F. De Angelis, R. Carzino, A. Toma, L. Razzari, J. Azaña, R. Morandotti, "Design and Fabrication of Terahertz Bragg Gratings on a Two-Wire Waveguide," Photonic North 2018 IEEE. Montreal, Quebec, Canada (2018)

Other publications

1. F. Yue, **V. Aglieri**, R. Piccoli, R. Macaluso, A. Toma, L. Razzari, R. Morandotti, "Highly sensitive polarization rotation measurement through a high order vector beam generated by a metasurface." **Advanced Materials Technologies**, 1901008 (2020)

2. X. Jin, **V. Aglieri**, A. Pezeshki, Y. Jeong, Y. Jia, R. Macaluso, E. Orgiu, A. Toma, and L. Razzari, ”Extracting the Dipole-Active Phonon Resonance of a Tungsten Diselenide Monolayer from Enhanced Spectroscopy using X-Shaped Terahertz Nanoslots,” *in preparation*
3. F. Yue, A. Aadhi, R. Piccoli, **V. Aglieri**, R. Macaluso, A. Toma, R. Morandotti, L. Razzari, “Rotational Doppler frequency shift from time-evolving high-order Pancharatnam-Berry phase,” *in preparation*
4. **V. Aglieri**, G. Lullo, M. Mosca, R. Macaluso, U. Lo Cicero, A. Zaffora, F. Di Franco, M. Santamaria, and L. Razzari, “Forming-free and self-rectifying resistive switching effect in Anodic Titanium Dioxide-based Memristors,” IEEE 4th International Forum on *Research and Technologies for Society and Industry* (RTSI), Palermo, Italy (2018). *Conference paper*
5. **V. Aglieri**, A. Zaffora, G. Lullo, M. Santamaria, F. Di Franco, U. Lo Cicero, M. Mosca, R. Macaluso, “Resistive switching in microscale anodic titanium dioxide-based memristors”, Superlattices and Microstructures, **113**, 135-142 (2018)

LIST OF SCHOLARSHIPS AND AWARDS
(DURING THE DOCTORAL PERIOD)

NSERC CREATE – Guided Light – An International Training Program. Dec. 2016 to Dec. 2019, $ 15 000 CAD, funded by Natural Sciences and Engineering Research Council of Canada (NSERC).

1 INTRODUCTION

The electromagnetic waves in the frequency range between 0.1 and 10 terahertz (THz) are characterized by peculiar properties, such as the non-ionizing character (that allows to conduct non-destructive characterizations on biological samples, such as human tissue), the transparency of many materials generally opaque in other frequency regimes (e.g. wood, cloth, etc.) [1], and the frequency location between the electronics (GHz) and photonics (hundreds of THz, up to PHz) regimes [2], thus being particularly appealing to improve the current state of the art of information technology. However, because of the difficulty in the production of affordable and efficient sources and detectors at these frequencies, the THz regime has been called for many years the “THz-gap” [1], [2]. Such limitations have been somehow overcame in the last few decades [1] thanks to the advances driven by scientists and industry, stimulated by a plethora of promising applications: fast telecommunication technology [3], imaging and sensing for security control of sealed packages and personnel inspection [4], [5], and industrial process and quality control [6], to name a few examples.

Among all the possible applications of THz technology, spectroscopy represents a valuable tool for the study of fundamental physical processes as well as for the characterization/recognition of materials. indeed a large number of elementary excitations fall in the THz range, such as rotational transitions of small molecules [7], large amplitude motions of biological molecules [8], lattice vibrations in solids [9], intraband transitions in semiconductors [10], [11], among others [1], [2], making THz spectroscopy highly attractive for e.g. physicists, engineers, physicians and chemists. Nevertheless, because of the long wavelength associated to this spectral range (~300 μm at 1 THz), micro- and nano-sized particle are practically invisible to the long THz waves [12] [13] due to the low sensitivity and low spatial resolution that limit the THz use on bulk materials or large aggregates of small particles.

To overcome this hurdle, many attempts have been conducted. Gallot et al. [14] designed a THz sensing platform composed of circular and rectangular waveguides. It was found that for the rectangular waveguide it was possible to increase the measurement sensitivity up to 50 times when compared to a single-pass reflection measurement. Thus, such technique has been used for sensing of biological molecules [15], drugs and explosives solids [16]. Yet, even if it is possible to retrieve spectroscopic information of the specimen under study, the enhanced sensitivity offered by the waveguides is only achieved if the specimen is deposited all over the platform area.

Also metamaterials [17] and metasurfaces [18] have been employed as enhanced sensing platforms in the THz regime. For example, in [12] a metasurface composed of elements with a small gap in the center of a squared metallic structure and periodically distributed over a THz-transparent substrate has been used. The device has been functionalized to attract microorganisms, such as bacteria, and then probed by THz-time domain spectroscopy (THz-TDS) technique. By comparing the THz characterization of the sample with and without the microorganisms, a shift in the resonance of the metasurface has been detected. Such shift is due to the change of the refractive index of the medium surrounding the metasurface, caused in this case by the presence of microorganisms. Moreover, it was demonstrated that a refractive index change is detected even for very small amounts of microorganisms, thus finally obtaining a high-sensitivity sensor. However, the metasurfaces so designed are able to detect only a change in refractive index and not the spectroscopic information of the deposited species.

A further development in the study of enhanced THz light-matter interaction comes from the realization of nanoslots as a THz sensing platform. These devices have been used for the detection of very small amounts of materials, thanks to the high field enhancement achieved through their light-driven capacitive behavior [18], [19]. In fact, by exploiting the high field enhancement factor obtained in such structures, it is possible to greatly improve the THz absorption coefficient of materials in tiny amounts. Park et al. in [19] have shown that nanoslots designed to resonate in correspondence to the RDX (1,3,5-trinitroperhydro-1,3,5-triazine) and lactose absorption lines (in the THz regime) can successfully detect the targeted molecules when drop-casted over the sensor surface, even at the tens of nanograms level (which corresponds to few femtograms of material inside the nanoslots). Such presence is observed through a consistent drop of the nanoslot transmission value at resonance in comparison with the bare case. Moreover, in [20] the possibility to discriminate between different chemical compounds by using nanoslots was demonstrated. Exploiting the same technique used in [19], two nanoslots designs (i.e., different slot lengths) have been patterned on two separated samples. The two sets have been chosen in order to resonate close to the absorption line of the D-glucose and fructose sugars, respectively. Thus, covering the same sample with both D-glucose and fructose sugars (half sample covered with D-glucose and the other half covered with fructose), only the sugar molecules with absorption line close to the nanostructure resonance frequency are detected. This happens because the nanoslots accumulate a field enhancement able to greatly increase the absorption coefficient of the sugar with closer absorption line. In this way, the selectivity of such THz sensing platform was demonstrated, not only for sugar molecules but also for other chemical compounds. Nevertheless, even if these last cases have shown huge

improvement in the employment of THz waves for sensing, it was still not enough to retrieve the full spectroscopic information of the investigated specimen.

Surface enhancement effects have been widely employed for the improvement of the sensitivity of traditional spectroscopy, by utilizing corrugated surfaces and metal particles whose characteristic size is much smaller than the incoming excitation wavelength. As an example, Raman spectroscopy is known to be an inherently inefficient process [21], but by employing surface-enhanced Raman spectroscopy (SERS) [22], [23] it is possible to greatly improve its sensitivity and characterize few molecules or even single particles [24]–[26]. The same approach has been used to improve infrared spectroscopy. Surface-enhanced infrared absorption (SEIRA) is capable to achieve high sensitivity for direct absorption spectroscopy, again on small amounts of materials [27]–[29]. Both Raman and infrared absorption critically depend on the local field values, and thus take great advantage from surface enhancement effects because of the very high field that can be obtained in proximity of metallic nanostructures.

By following the recent advances in both metasurface-improved sensing in the THz regime and surface enhancement techniques, Razzari et al. in Ref. [30] proposed a new platform consisting of an array of gold dipolar NAs resonating in the THz range. They demonstrate high field enhancement values at the NA extremities that can be employed to greatly improve the sensitivity of THz-based spectroscopy techniques. Few years later, Toma et al. in Ref. [31], shown that by properly endowing the previous array structure with interparticle nanometric gaps, it is possible to obtain a greatly enhanced near field in the gap area. Thanks to the squeezing of the THz electric field into such gaps, the overall enhancement was increased at such a level that the absorption cross-section of nano-sized materials placed in the nanocavities was found to be more than a million times the case of non-assisted THz spectroscopy. Thus, by placing cadmium selenide (CdSe) quantum dots over the surface of the NA arrays, their spectroscopic information was promptly retrieved because of the coupling between the greatly enhanced NA field and the phonon resonance of CdSe quantum dots, finally resulting in a Fano-like resonance clearly visible in the THz transmission spectra. Such advances have been recently exploited by Jin et al. in Ref. [32] where they were not only able to detect the spectroscopic fingerprint of cadmium sulphide (CdS) nano-crystals, but also to reshape their phonon resonance under strong light-matter coupling (more information on this will be presented in Section (4.3)).

Such achievements have been obtained thanks to the unique ability of plasmonic NAs to convert the free-propagating radiation into strongly localized near fields [33]–[35], thus making very long wavelength THz waves interacting with nano-objects [13], [30], [31]. However, albeit the good results obtained so far, there is still room for improvement of the

plasmonic NA performances, because of the loss suffered by surface waves [36], [37] travelling over these devices. Nonetheless, by finely engineering plasmonic NAs it will be shown that it is possible to increase the near field and to reduce the mode volume (the equivalent volume occupied by the electromagnetic field), finally reaching improved performances, towards the ability to push the detection limit down to the single nano-object for THz interactions.

1.1 NA Performances Improvement

Despite the successful experiments just presented on the study of the spectroscopic information of materials and compounds in the THz regime, there is still room to improve NA performances in this frequency range. This is mainly related with the intrinsic lossy nature of metallic nanostructures in the THz region [36].

In order to improve NAs, many metals have been studied as material for NA fabrication, such as aluminum, silver, alkali metals, gold [38], etc. Also semiconductors have been investigated as alternative materials for NAs, due to the tunability of their carrier concentration through the introduction of impurities (doping), and for their higher melting temperature (desirable parameter especially for experiments involving intense sources). Nonetheless, also semiconductors suffer from very high loss [39]. Among these materials, one of the most widely used is gold because of its high conductivity [40], ease of processing and chemical stability (compared to other metals).

As seen in [31], by coupling two NAs end-to-end it is possible to greatly improve the field enhancement in the interparticle cavity. Further studies on the gap size have shown that by modifying the gap features, i.e. width and height, it is possible to improve the field enhancement. Suppose to have an end-to-end coupled NA pair. The gap width is determined by the distance between the NAs extremities forming the cavity. In order to achieve higher field enhancement values the NAs can be made closer to each other [41]. However, even if modern nano-fabrication techniques allow for the creation of tiny antenna gaps, too small gap width results in the tunneling of electrons through the gap, thus forming an equivalent longer antenna [42] and making this strategy ineffective. The gap height, determined by the NA lateral width, can also be modified to improve the field enhancement. In particular, by shrinking the antenna lateral width (or equivalently the gap height) a higher field enhancement is obtained, but too narrow NAs results in very high losses due to the increase in the imaginary part of the effective refractive index for the surface wave that leads to an enhanced absorption at the metal interface [43]. This last issue is particularly affecting the performance of NAs resonating in the THz regime, because of the very large aspect ratio of THz NAs. In fact, as it will be shown in detail in the following chapter, the NA length is

related to the resonance wavelength as $L \approx \lambda_{\mathrm{res}}/2n_{\mathrm{eff}}$, thus if the NA resonate at $1\ \mathrm{THz}$, that is $300\ \mu\mathrm{m}$, the aspect ratio $AS = L/w$, with w antenna width (the minimum dimension of which is fixed by nanofabrication technology constraints), results to be extremely large [44], [45].

It has to be noted that the gap width and height should be designed considering also the application in which the NAs will be used for. For instance, if NAs are employed for the study of specific nanocompounds spectroscopic features, the gap size has to be large enough to properly accommodate such nanosystems, finally introducing another constrain in the geometric features of the NAs. The improvement of the NA near field enhancement is then a great challenge. No low loss materials available and geometric constrains make the improvement strategies seen so far limited.

Nevertheless, in order to obtain a better field localization and higher field enhancement, in the past alternative geometries have been proposed for the improvement of NA performances. For example, tapered waveguides with *semi-infinite* length have been numerically shown to produce a 20 times higher plasmonic energy density at the tip [46], and *non-resonant* tapered gold rods have been simulated presenting strong near field enhancement while optimizing the tapering angle [47], [48]. Tapered geometries have thus attracted great attention thanks to the highly localized field at their smaller extremities [33], [46], which in principle allows to conduct improved nanoscale imaging and spectroscopy experiments [49]. However, *resonant* tapered NA pairs/dimers, known as “bow-tie” antennas, have been shown to produce in the IR regime larger resonace bandwidth at the expenses of a lower field enhancement, when compared with the straight dipolar configuration [34], [50]–[53].

In this thesis it is shown, both theoretically and experimentally, that an improvement in the near field performance can be obtained by carefully tapering THz resonant NAs. In fact, by choosing the correct values for the tapering angle, it is possible to optimize the trade-off between radiative and non-radiative loss, thus achieving a net improvement of the overall antenna performances. The tapering strategy adopted only involves a partial geometrical modification. In particular, the gap features remain unaltered, thus granting a large degree of freedom to the final antenna design, while improving the field enhancement and the mode volume produced by the NAs. Initially, here it will be shown how such approach affects the antenna performances in the THz regime, also highlighting the fact that it can be effectively applied to the IR frequency range. Our findings will then be used to improve the results of previously performed strong coupling experiment with straight, not optimized architectures [32]. Finally, thanks to the loss relaxation effect of the tapering strategy, it will be shown that it is possible to employ alternative materials for the NA fabrication. In fact, the indium tin

oxide (ITO) semiconductor material (a conductive oxide, transparent to visible radiation), usually too lossy for the fabrication of THz NAs, is demonstrated to resonate in the THz regime when a proper tapering strategy is applied. The ITO NAs have important potentialities, for example, in the nonlinear regime, as an alternative material to gold, which usually gets damaged during THz nonlinear experiments because of the high local THz electric fields.

1.2 Chapters Overview

In Chapter 2, a brief introduction of plasmons in bulk materials, surfaces and particles is presented. The theoretical treatment introduced here is then used to explain the plasmonic behavior of metallic NAs, schematically represented as elongated plasmonic particles. Finally, a simple Fabry-Perot model is introduced to qualitatively describe the NAs electromagnetic response.

In Chapter 3, the Fabry-Perot model is revisited to properly account for the response of tapered cylindrical NAs, and it is used to understand the underlying physical mechanism to optimize NA performances. Then simulations in COMSOL confirm that this strategy can be applied also in the planar gold NAs case and the results are used to design and fabricate five real NA samples. Moreover, it is numerically demonstrated the validity of the tapering strategy also in the IR regime.

In Chapter 4, the fabrication steps for THz NAs and the THz time domain spectroscopy characterizations are presented. Experimental and simulation results are compared to confirm the validity of the tapering strategy. The same strategy is then applied to ITO antennas resonating in the THz regime. By exploiting the loss relaxation property of the tapering method, ITO antennas are experimentally shown to resonate in this spectral window.

In Chapter 5, taking advantage of the beneficial effect offered by the tapering strategy, the application of this improvement method to strong coupling experiments is discussed. It is numerically and experimentally shown that strong coupling studies greatly benefit from the improved field localization obtained through tapered nanostructures.

In Chapter 6, the crucial points contained in this thesis are summarized.

In Chapter 7, a brief list of additional projects in the framework of the joint Ph.D. program is presented.

2 Plasmonics: Theoretical Background

Near field enhancement is the fundamental tool to make THz waves interacting with nano-sized objects, and results from the localization of the free-propagating radiation into a sub-wavelength volume by means of plasmonic NAs. Thus, it is important to give an introductory overview on plasmonic theory, here reported and based on [54], in order to understand how to exploit all the capabilities of plasmonic antennas to produce a higher field enhancement in smaller mode volumes.

2.1 Bulk Plasmons

In general, when an external electric field of sufficiently low frequency is applied to an "electron gas", the electrons can be pictured to move perfectly following the external stimulus. However, increasing the frequency results in an increasingly higher phase shift between electron position and field amplitude, until the electrons are no more capable to follow the external electric field excitation. The frequency depicting this transition is called *bulk plasma frequency* ω_p. For example, in the case of metals, as long as the frequency ω of the external excitation is lower than ω_p, metals result opaque, but when $\omega > \omega_p$ they become transparent to the external radiation.

In order to retrieve the plasma frequency, it is important to study the phase-shift between electron position and external field amplitude: the equation of motion of an electron under the influence of an electric external field can be written as

$$m\ddot{\mathbf{x}} + m\gamma\dot{\mathbf{x}} = -e\mathbf{E} \tag{2.1}$$

where m is the electron mass, $\gamma = 1/\tau$ is the collision frequency (while τ is known as carrier life time), e is the elementary charge, $\mathbf{x}$ is the electron position in space, and $\mathbf{E}$ is the external applied electric field. Assuming $\mathbf{E}(t) = \mathrm{E}_0 \mathrm{e}^{-j\omega t}$ and $\mathbf{x}(t) = \mathbf{x}_0 \mathrm{e}^{-j\omega t}$, we can write

$$\mathbf{x}(t) = \frac{e}{m(\omega^2 + j\gamma\omega)}\mathbf{E}(t). \tag{2.2}$$

The polarization vector $\mathbf{P} = -ne\mathbf{x}$ (being n number density of free electrons) depends on the displacement of the electrons, thus

$$\mathbf{P} = -\frac{ne^2}{m(\omega^2 + j\gamma\omega)}\mathbf{E}(t) \tag{2.3}$$

from which it is possible to calculate the dielectric displacement field $\mathbf{D} = \varepsilon_0\mathbf{E} + \mathbf{P}$ as

$$\mathbf{D} = \varepsilon_0 \left(1 - \frac{\omega_p^2}{\omega^2 + j\gamma\omega}\right)\mathbf{E}(t), \tag{2.4}$$

where $\omega_p^2 = ne^2/\varepsilon_0 m$, is the *bulk plasma frequency*. Finally, the dielectric permittivity of the electron gas can be calculated as:

$$\varepsilon(\omega) = 1 - \frac{\omega_p^2}{\omega^2 + j\gamma\omega}. \tag{2.5}$$

that is the Drude-Sommerfeld model. In the case when $\omega/\gamma \gg 1$, the permittivity is mainly real with negative value and the metal can be considered ideal allowing to simplify the Drude model as

$$\varepsilon(\omega) = 1 - \omega_p^2/\omega^2. \tag{2.6}$$

Thus, for $\omega > \omega_p$ the permittivity becomes positive and the metal results to be transparent to the incoming radiation. It has to be noted that in case of real metals, the Drude-Sommerfeld model has to be rewritten as

$$\varepsilon(\omega) = \varepsilon_\infty - \frac{\omega_p^2}{\omega^2 + j\gamma\omega} \tag{2.7}$$

where $1 \leq \varepsilon_\infty \leq 10$ [54] represent the residual polarization due to the positive background of the fixed positive charges in the metal.

In order to retrieve the dispersion relation of bulk plasmons, it is useful to examine the solutions of Maxwell's equation in the absence of external stimuli (i.e. $\rho_{ext} = 0$, $\boldsymbol{J}_{ext} = \mathbf{0}$). For a transverse wave the dielectric permittivity can be written as

$$\varepsilon(\mathbf{K}, \omega) = \frac{K^2 c^2}{\omega^2} \tag{2.8}$$

where $\mathbf{K}$ is the wave vector, and c the speed of light. Substituting this expression in the undamped permittivity of Equation (2.6), we obtain the dispersion relation:

$$\omega^2 = \omega_p^2 + Kc^2. \tag{2.9}$$

The trend of such relation is depicted in **Figure 2.1** for a generic metal. As it can be seen, the propagation of transverse waves is not allowed at frequency below the plasma frequency ω_p, where the incoming radiation is almost completely transferred to the free electrons. On the other hand, transverse waves can propagate trough metals when $\omega > \omega_p$.

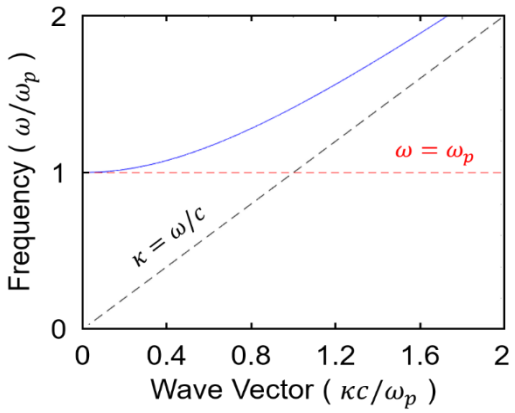

Figure 2.1 The dispersion relation of a bulk plasmon (blue solid curve), the light line $k = \omega/c$ (dashed black line), and the $\omega = \omega_p$ border between transparent and opaque metallic behavior (dashed red line).

In the particular case of $\omega = \omega_p$, the dispersion relation returns $\kappa = 0$, that correspond to a collective longitudinal oscillation of all the conduction electrons in metal. The quantum of such oscillation is called *bulk plasmon* or *volume plasmon*. Due to their longitudinal nature, bulk plasmons cannot be excited by transverse electromagnetic waves, but, e.g., through particle impact.

2.2 Surface plasmons

Surface plasmon is the quantum of energy of the surface wave established at the perfectly flat interface between two materials with opposite real dielectric permittivity (usually the interface between a metal and a dielectric). Such waves propagate along the interface plane exciting the electron gas of the metallic region, with evanescent tails inside both materials.

The description of the surface plasmons starts from the derivation of the wave equation in a general form. First, the Faraday and Ampere-Maxwell's laws can be combined considering the absence of external charges and currents ($\nabla \cdot \mathbf{D} = 0$), and considering a negligible variation of the dielectric permittivity over distance comparable to the wavelength involved, that is $\varepsilon(\mathbf{r}) = \varepsilon$, the general form of the wave equation can be obtained as

$$\nabla^2 \mathbf{E} - \frac{\varepsilon}{c^2} \frac{\partial^2 \mathbf{E}}{\partial t^2} = 0. \tag{2.10}$$

Now, the wave equation has to be solved for each material forming the interface, and the two solutions have to be matched at the interface by using the correct boundary conditions. Thus, it is first assumed an electric field in the form $\mathbf{E}(\mathbf{r},t) = \mathbf{E}(\mathbf{r})e^{-j\omega t}$, and inserting it in the Equation (2.10) leads to the Helmholtz equation

$$\nabla^2\mathbf{E} + \kappa_0\varepsilon\mathbf{E} = 0 \tag{2.11}$$

where $\kappa_0 = \omega/c$ is the wave vector of the wave propagating in vacuum. Here, it has been assumed that there are neither external charges nor external current density, and that the geometry is an infinitely extended interface whose plane corresponds to the $x-y$ plane, as shown in **Figure 2.2**. In such system, it is supposed that the surface plasmon wave travels along the x-axis ($z = 0$), while the dielectric permittivity changes only in the z coordinate ($\varepsilon = \varepsilon(z)$):

- for $z < 0$ the metallic region presents a negative real permittivity $\mathrm{Re}\{\varepsilon_1\} < 0$,
- for $z > 0$ the dielectric region is characterized by a positive real permittivity $\mathrm{Re}\{\varepsilon_2\} > 0$.

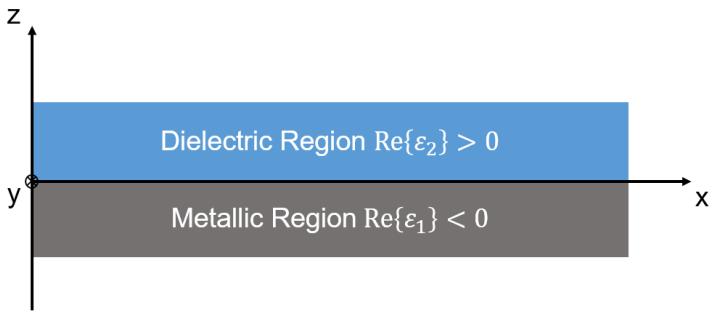

Figure 2.2 Sketch of a 2D plane interface between dielectric and metallic regions.

Metals show a negative permittivity for frequencies smaller than the plasma frequency of the metal itself ($\omega < \omega_p$). In this scenario the electric field of the travelling surface plasmon wave can be written as

$$\mathbf{E}(x,y,z) = \mathbf{E}(z)\mathrm{e}^{j\beta x}, \tag{2.12}$$

with $\beta = \kappa_x$ being the propagation constant. Substituting this expression in the Equation (2.11), we obtain:

$$\frac{\partial^2\mathbf{E}(z)}{\partial z^2} + (\kappa_0^2\varepsilon - \beta^2)\mathbf{E} = 0, \tag{2.13}$$

a similar expression exists for the magnetic field $\mathbf{H}$. From this equation, it is possible to determine the spatial field profile and dispersion of travelling surface plasmon waves. To this

end, Equation (2.13) has to be treated by means of the Faraday and Ampere-Maxwell's laws to obtain the expression of the electromagnetic field components. In fact, assuming a harmonic time dependence ($\partial/\partial t = -j\omega$), propagation along x-axis ($\partial/\partial x = j\beta$) and homogeneity in the y-axis ($\partial/\partial y = 0$), one obtains the two simplified sets of equations

$$\begin{aligned} \frac{\partial E_y}{\partial z} &= -j\omega\mu_0 H_x \\ \frac{\partial E_x}{\partial z} - j\beta E_z &= j\omega\mu_0 H_y \\ j\beta E_y &= j\omega\mu_0 H_y \end{aligned} \tag{2.14}$$

and

$$\begin{aligned} \frac{\partial H_y}{\partial z} &= -j\omega\varepsilon_0\varepsilon E_x \\ \frac{\partial H_x}{\partial z} - j\beta H_z &= j\omega\varepsilon_{0\varepsilon} E_y \\ j\beta H_y &= j\omega\varepsilon_0\varepsilon E_y \end{aligned} \tag{2.15}$$

From these two sets of equations, we can extrapolate other two sets regarding transverse magnetic (TM) and transverse electric (TE) modes, also known as p- and s-polarized modes, respectively. For the TE mode one obtains

$$\begin{aligned} H_x &= j\frac{1}{\omega\mu_0}\frac{\partial E_y}{\partial z} \\ H_z &= \frac{\beta}{\omega\mu_0} E_y \end{aligned} \tag{2.16}$$

and the TE wave equation

$$\frac{\partial^2 E_y}{\partial z^2} + (k_0^2\varepsilon - \beta^2)E_y = 0 \tag{2.17}$$

Calculating the TE modes for $z > 0$ (dielectric half space)

$$\begin{aligned} E_y(z) &= A_2 e^{i\beta x} e^{-\kappa_2 z} \\ H_x(z) &= -jA_2\frac{1}{\omega\mu_0} k_2 e^{i\beta x} e^{-\kappa_2 z} \\ H_z(z) &= A_2\frac{\beta}{\omega\mu_0} e^{i\beta x} e^{-\kappa_2 z} \end{aligned} \tag{2.18}$$

and for $z < 0$ (metallic half space)

$$E_y(z) = A_1 e^{i\beta x} e^{\kappa_1 z}$$

$$H_x(z) = jA_1 \frac{1}{\omega\mu_0} k_1 e^{i\beta x} e^{\kappa_1 z} \tag{2.19}$$

$$H_z(z) = A_1 \frac{\beta}{\omega\mu_0} e^{i\beta x} e^{\kappa_1 z}$$

with $\kappa_i \equiv \kappa_{z,i}$ $(i = 1, 2)$ being the wave vector component in the medium 1 (dielectric) and 2 (metal). The reciprocal value $\hat{z} = 1/|\kappa_z|$ defines the length of the field tails that evanescently decay in the two materials. The continuity at the interface requires for TE modes is $A_1(\kappa_1 + \kappa_2) = 0$, and confinement at the surface requires that the real part of the two wave numbers is positive, then $A_1 = 0$ and thus $A_1 = A_2 = 0$, finally revealing that no surface modes are possible for TE polarization.

TM polarization are then the only modes able to excite surface waves. Recalling Equations (2.14) and (2.15) one obtains for TM modes

$$H_y(z) = A_2 e^{i\beta x} e^{-\kappa_2 z}$$

$$E_x(z) = jA_2 \frac{1}{\omega\varepsilon_0\varepsilon_2} k_2 e^{i\beta x} e^{-\kappa_2 z} \tag{2.20}$$

$$E_z(z) = -A_2 \frac{\beta}{\omega\varepsilon_0\varepsilon_2} e^{i\beta x} e^{-\kappa_2 z}$$

for $z > 0$ (dielectric half space) and

$$H_y(z) = A_1 e^{i\beta x} e^{\kappa_1 z}$$

$$E_x(z) = -jA_1 \frac{1}{\omega\varepsilon_0\varepsilon_1} k_1 e^{i\beta x} e^{\kappa_1 z} \tag{2.21}$$

$$E_z(z) = -A_1 \frac{\beta}{\omega\varepsilon_0\varepsilon_1} e^{i\beta x} e^{\kappa_1 z}$$

for $z < 0$ (metallic half space). Continuity of the fields at the interface requires this time that $A_1 = A_2$ and then

$$\frac{\kappa_2}{\kappa_1} = -\frac{\varepsilon_2}{\varepsilon_1} \tag{2.22}$$

that is, the surface waves can exist at the interface of materials with real part of dielectric permittivity of opposite sign (being wavenumber non-negative values). Moreover, from the continuity condition it is also possible to extract the dispersion relation:

$$\beta = \kappa_0 \sqrt{\frac{\varepsilon_1 \varepsilon_2}{\varepsilon_1 + \varepsilon_2}}. \tag{2.23}$$

The dispersion relation is depicted in **Figure 2.3**, where the red solid line represents the dispersion relation of a TM mode at the interface between dielectric and metals. The dashed red horizontal line represents the condition $\omega = \omega_{sp}$ where:

$$\omega_{sp} = \frac{\omega_p}{\sqrt{1 + \varepsilon_2}} \tag{2.24}$$

is called *surface plasmon frequency*. When the frequency $\omega \to \omega_{sp}$, $\beta \to +\infty$ and the group velocity $v_g \to 0$, thus the mode that is excited at this interface has an electrostatic character and is called *surface plasmon*. Between the surface plasmon and bulk plasmon frequencies there is a gap where the propagation of surface plasmons is not allowed. This is due to the idealization of the dielectric permittivities, as it was supposed to be a pure real number, therefore without imaginary component. In a real situation, the materials forming the interface structure are lossy and thus the imaginary part of the dielectric permittivity of metals is non-zero, the propagation constant β is a complex number and the surface plasmons are travelling waves with propagation length $L = 1/(2\,\mathrm{Im}\{\beta\})$. Therefore, β does not diverge for $\omega \to \omega_{sp}$, while instead it assumes a finite value. Thanks to the complex character of the dielectric permittivities, the frequency region between ω_{sp} and ω_p is available for surface plasmon propagation. In fact, the finite value of the wave number β leads to a lower limit to the surface plasmon wavelength $\lambda_{sp} = 2\pi/\mathrm{Re}\{\beta\}$ and, in particular, to the mode confinement $\hat{z}$. The surface plasmon decay length over the z-axis falls off in the

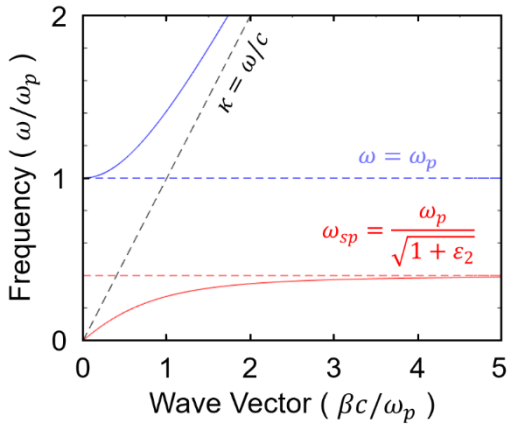

Figure 2.3 Dispersion relation for a TM mode at the interface between two material with opposite real dielectric permittivity (red solid curve) and the surface plasmon frequency (dashed red line). In the figure are also reported the dispersion relation for transverse waves in bulk metals (blue solid line), the light line (dashed black line) and the $\omega = \omega_p$ limit (dashed blue line).

dielectric as $e\text{^}|\kappa_z||z|$, with $\kappa_z = \sqrt{\beta^2 - \varepsilon_2\left(\frac{\omega}{c}\right)^2}$, thus recalling that the confinement is given by $\hat{z} = 1/|\kappa_z|$, the closer the frequency of the incoming radiation is to the surface plasmon frequency, the higher the confinement. The field confinement is one of the crucial points discussed in this thesis. It will be shown the importance of the volume where the field is confined and its implications on the field enhancement, that are two fundamental parameters in the use of surface enhancement effects.

2.2.1 Excitation of Surface Plasmons

As **Figure 2.3** shows, the light line is tangent in the origin to the dispersion relation of surface plasmon, while it strongly deviates as the frequency increases. The wave vector of a free-space wave illuminating the metal/dielectric interface has a propagation constant along the interface $\kappa_x < \beta$, being $\kappa_x = \kappa_0\sqrt{\varepsilon}\sin(\theta)$ (κ_0 is the wave number in vacuum and ε is the permittivity of the dielectric side of the interface). Thus, whatever incident angle θ is used, κ_x will never be enough high to reach the wave vector value of the surface plasmon. In other words, free-space propagating electromagnetic waves are not capable to deliver sufficient momentum at a perfect and infinitely extended interface to excite a surface plasmon. Nonetheless, it is possible to excite surface plasmons by using the Kretschmann [54], [55] or the Otto [54], [56] configurations that will not be shown here for the sake of brevity.

2.3 Localized Surface Plasmons

The discussion about plasmons has been conducted so far in the case of infinitely large structures, such as an infinitely extended interface or bulk (semi-infinite) materials. However, surface plasmons can be excited also on small isolated particles and structures. In this case, they are responsible for the so-called *localized surface plasmon resonances (LSPRs)*.

The simplest example of finite structure is a sphere with radius a much smaller than the wavelength of an external excitation field ($a \ll \lambda$). In such condition, the field induced inside the particle sphere can be approximated to be an electrostatic field, thus simplifying the calculation while maintaining good coherence between theoretical predictions and experimental evidences. Let's suppose that the sphere is made of a homogenous and isotropic material, immersed in a homogenous and non-absorbing surrounding material with permittivity ε_d. Assuming as electrostatic the electric field felt by the sphere, it is possible to calculate the dipole moment as

$$\mathbf{p} = 4\pi\varepsilon_0 a^3\left(\frac{\varepsilon - \varepsilon_d}{\varepsilon + 2\varepsilon_d}\right)\mathbf{E}_0. \tag{2.25}$$

The *polarizability* α is linked to $\mathbf{p} = \varepsilon\varepsilon_d\alpha\mathbf{E}_0$, thus obtaining

$$\alpha = 4\pi a^3 \left(\frac{\varepsilon - \varepsilon_d}{\varepsilon + 2\varepsilon_d}\right). \tag{2.26}$$

It is possible to observe that a resonant behavior occurs when $|\varepsilon + 2\varepsilon_d|$ experiences a minimum. In particular, assuming that the imaginary part of the dielectric permittivity of the sphere is characterized by an almost constant value around the resonance condition, the latter can be written as

$$\mathrm{Re}\{\varepsilon(\omega)\} = -2\varepsilon_d \tag{2.27}$$

called Fröhlich (FR) condition. At the frequency ω when such condition is satisfied, a localized surface plasmon mode is excited. Moreover, if the particle is made of a Drude metal, the resonance frequency can be calculated as

$$\omega_{lsp} = \frac{\omega_p}{\sqrt{1 + 2\varepsilon_d}}, \tag{2.28}$$

which indicates the dependence of the frequency position of the localized surface plasmon wave as a function of the dielectric permittivity of the surrounding medium. This means that particle spheres can be used as excellent detection tool for, e.g., composition changes in the surrounding medium.

Finally, it is important to show the electric field inside and outside the sphere when illuminated by an electrostatic field:

$$\mathbf{E}_{\mathrm{in}} = \frac{3\varepsilon_d}{\varepsilon + 2\varepsilon_d}\mathbf{E}_0 \tag{2.29}$$

$$\mathbf{E}_{\mathrm{out}} = \mathbf{E}_0 + \frac{3\mathbf{n}(\mathbf{n}\cdot\mathbf{p}) - \mathbf{p}}{4\pi\varepsilon_0\varepsilon_d}\frac{1}{r^3} \tag{2.30}$$

with r distance from the point P and $\mathbf{n}$ unit vector. In both cases, a resonance occurs again at the Fröhlich condition, thus, in case of excitation of a localized mode, an enhancement of the electric fields occurs. In particular, the field just outside the particle sphere $\mathbf{E}_{\mathrm{out}}$ is known as *near field*. Such local field is a fundamental property of plasmonic resonators, of paramount interest for all those applications that exploit the near field enhancement, such as surface-enhanced Raman spectroscopy, surface-enhanced infrared absorption [13], and NA-based THz technology as shown in the first part of this thesis.

In the following, it is presented a progressively accurate modeling of plasmonic particles to finally obtain a simple formula for the calculation of the near field produced by an elongated NA.

2.4 Elongated Plasmonic Particles: Nanoantennas prototype

Antennas are electric devices devoted to the detection and transmission of electromagnetic waves traveling through the atmosphere or other media. The electromagnetic field irradiated originates from the current flowing through the antenna that acts as a conductive wire. Vice versa, when an electromagnetic field approaches an antenna, it is able to induce an electric current in it. One of the most important parameters in antenna design is then the *conductivity* and for this reason, metals are generally employed as main material for the fabrication of antennas. For a large range of frequencies, metals can be considered perfect conductors, thus resulting to be a perfect material for antenna design. However, this concept does not hold when electromagnetic waves at very high frequencies are involved [33], such as IR and visible regimes. In fact, Drude metals at high frequencies suffer from very high loss.

In order to study antennas at high frequencies, they can be modeled as an elongated version of the plasmonic spheres shown in the previous section. In this case, the dipole moment of Equation (2.25) can be rewritten as

$$\mathbf{p} = V\varepsilon \frac{\varepsilon - \varepsilon_d}{P_j\varepsilon + (1 - P_j)\varepsilon_d}\mathbf{E}_0 \tag{2.31}$$

with V volume of the elongated sphere, P_j factor that depends of the aspect ratio $AS = \frac{d}{2}/r$, with d antenna length and r antenna radius. It has been shown that, by exciting with external light polarized along the main axis of the elongated sphere, the resonance frequency depends on the aspect ratio; in particular, an increased AS results to a red-shift of the resonance frequency [33].

To go deeper into the resonance characteristics of such structures, a mass-spring model can be employed [33], [57]. Suppose a resonance frequency $\omega_{\text{res}} = \sqrt{k/m}$, with k spring constant and m mass: the first relates with the restoring force due to an electron displacement inside the elongated sphere, and the second with the mass of the electron cloud of the metal. Assuming the elongated antenna to have a perfect cylindrical shape, as shown in **Figure 2.4 (a)**, if the electrons move towards one end of the cylindrical antenna with displacement Δx, the charge that such electrons create at this end is

$$q = n(-e)A\Delta x \tag{2.32}$$

Where n represents the number of electrons, e the elementary charge and A the cross-sectional area of the cylinder. At the same time an equal and opposite in sign charge is accumulated to the other cylinder end (**Figure 2.4 (a)**). This charge distribution create a Coulomb potential energy

$$W(\Delta x) = \frac{1}{4\pi\varepsilon_0}\frac{q^2}{d} = \frac{1}{4\pi\varepsilon_0}\frac{(neA)^2}{d}\,\Delta x^2, \tag{2.33}$$

from which it is possible to calculated the restoring force of the system as

$$F(\Delta x) = -\frac{\delta W}{\delta \Delta x} = -\frac{1}{2\pi\varepsilon_0}(ne)^2\frac{A^2}{d}\,\Delta x, \tag{2.34}$$

with spring constant

$$k = \frac{(ne)^2}{2\pi\varepsilon}\frac{A^2}{d}. \tag{2.35}$$

By substituting the spring constant value in the formula $\omega_{\text{res}} = \sqrt{k/m}$, and recalling the formula for bulk plasmon resonance, one obtains

$$\omega_{\text{res}} = \frac{\omega_p}{2\sqrt{2}}\frac{1}{AS}. \tag{2.36}$$

It is now clear that for an elongated plasmonic particle, the resonance depends on the

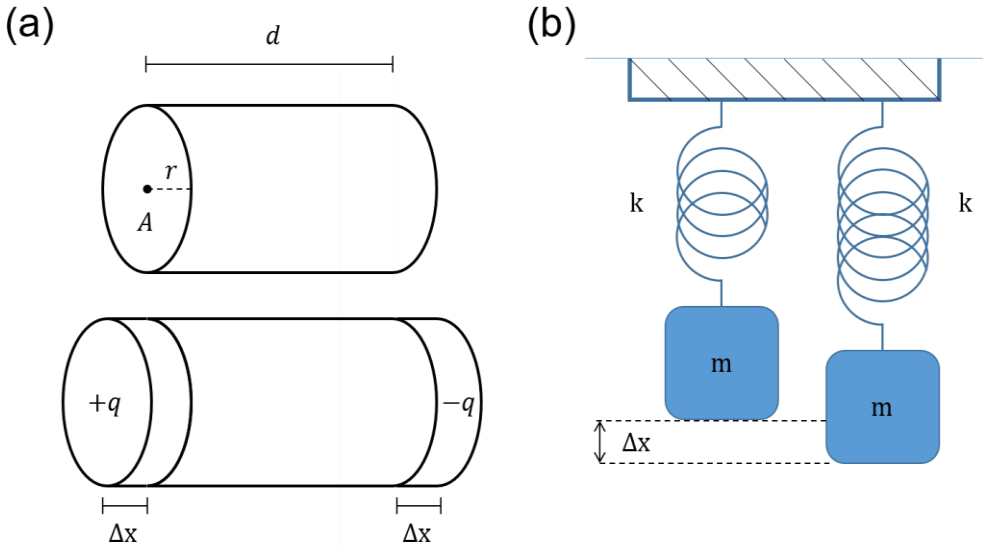

Figure 2.4 (a) At the top a sketch of cylindrical metallic plasmonic particle, with length d, radius r, and cross sectional area $A = \pi r^2$; at the bottom accumulated charges at the cylinder extremities, with $\pm q$ electric charge, and Δx displacement value of the charge carriers. (b) Spring-mass modeling of the charge displacement in the cylinder, with k elastic constant of the spring related to the restoring force due to the mutual attraction created by the charges at the two cylinder ends, m mass of the electron cloud inside the cylinder, and Δx representing the charge carrier displacement.

geometrical shape of the particle itself and not only on the relevant dielectric permittivities. Such dependence holds true as long as the aspect ratio AS remains smaller than the excitation wavelength [58], [59]. For this reason, antennas for very high frequencies have nanoscale lengths. As in the case of plasmonic spheres, also NAs generate a far field and a near field response enhanced under resonant conditions. In systems with significant loss, the measured near field resonance can result red-shifted when compared to the far field resonance [54].

A very interesting case of study is the end-to-end coupled NAs. Such configuration is very useful for light-matter interaction experiments, thanks to the very high near field enhancement confined in the gap between NAs. Assuming the case of two identical end-to-end coupled NAs: the two antennas can be modeled as two independent mass-spring systems while the gap can be represented by a third spring that connects the masses of the NAs electron clouds making them coupled. Thanks to the presence of this third spring, the previously independent NA modes of the two mass-spring models hybridize into two new eigenmodes, called anti-bonding (or dark) and bonding (or bright) mode. In the anti-boding case, the charge in the two NAs would oscillate out-of-phase, thus canceling each other in far field as long as the system and the external illumination paths are symmetric. This result translates into a dark resonance, where no signal is transmitted in far field. Instead, in the bonding configuration the charges in the two NAs oscillate in-phase, thus constructively interfering in the far field and resulting in a detectable signal. This can be obtained through external illumination with wave polarized along the NA long axis. The resonance frequency results red-shifted in far field compared to the one presented by the single NA, due to the gap interaction between the two structures.

For the purpose of this thesis, coupled NAs have been more extensively studied and employed in comparison to single antennas, because of their higher field enhancement. Moreover, we will study the far field detectable mode, i.e. the bonding resonance, because it is the mode of relevance for all the experimental characterizations presented here.

2.5 The Fabry-Peròt Model

Until now, it has been supposed that the electric field induced in these particles had an electrostatic character. This is true when the size of the particle considered is sufficiently small ($a \ll \lambda$). However, when elongated particles are taken into account, the electrostatic character of the ideal situation is not fully satisfied. A more accurate description is represented by a *propagating* surface wave. In order to study this situation, we have considered a surface wave propagating at the interface between metal and dielectric. The metal side can be imagined to form an infinitely long metallic wire, still sustaining the same

surface wave. If the wire is truncated to form a metallic cylinder, the surface mode still propagate over the cylinder, but - this time - it is reflected at the two ends, thus oscillating back and forth over the cylinder surface. Under this scenario, the NA resonance properties also depend on the (not perfect) reflections at the NA extremities. In order to comprehensively study such situation, a metal wire can be modeled as a Fabry-Perot resonator, where the two NA extremities act as partially reflecting mirrors [13], [33].

Let's suppose the NA to be a metallic cylinder, with radius r and length L, characterized by dielectric permittivity $\varepsilon_m(\omega)$, and embedded in a dielectric environment with dielectric constant ε_d. This configuration is known to support a TM_0 axially symmetric mode [13]. In this scenario, standing waves can be formed at the resonance wavelength λ_{res}, which can be approximated as:

$$\lambda_{\mathrm{res}} = 2(L + 2\delta)n_{\mathrm{eff}} \tag{2.37}$$

where n_{eff} is the effective index experienced by the TM_0 mode propagating along the antenna surface, and δ is the parameter that take into account the increase in antenna length L due to the reactance of the antenna ends [13], [60]. The complex effective refractive index n_{eff} for the TM_0 mode of a cylindrical wire can be derived from the Maxwell's equations by applying the proper boundary conditions at the dielectric-metallic cylinder interface [61]

$$\frac{\varepsilon_m}{\kappa_m}\frac{I_1(\psi_m r)}{I_0(\psi_m r)} + \frac{\varepsilon_d}{\kappa_d}\frac{K_1(\psi_d r)}{K_0(\psi_d r)} = 0, \tag{2.38}$$

where I_j and K_j $(j = 0, 1)$ are the modified Bessel functions, $\psi_{m,d} = \kappa_0\sqrt{n_{\mathrm{eff}}^2 - \varepsilon_{m,d}}$, $\kappa_0 = \omega/c$, $\kappa_{m,d} = \sqrt{n_{\mathrm{eff}}^2 - \varepsilon_{m,d}}$. In order to preserve the symmetry of the problem, the electric and magnetic fields outside the antenna are expanded in terms of rotationally invariant free-space modes. Then, the transverse electric and magnetic fields are matched at the end of the metal rod and the dielectric surrounding; thus the complex reflection coefficient (i.e. including phase and amplitude) is retrieved and calculated in closed form for a subwavelength system [61] without losing accuracy when considering a single mode dominating the whole behavior [62]. Finally, it is possible to calculate the electric field at one antenna tip E_{tip} as in the classical form of a Fabry-Perot resonator

$$E_{\mathrm{tip}} = E_0\frac{\left(1 - Re^{2j\phi}\right)\left(1 - e^{2j\phi}\right)}{1 - R^2e^{4j\phi}}, \tag{2.39}$$

where, E_0 is a reference input value for the surface wave field, and

$$\phi = \kappa_0 n_{\text{eff}} L \tag{2.40}$$

is the phase accumulated by the propagating surface mode in half a round trip.

The so calculated field gives a very accurate approximation and description on the behavior of surface waves propagating on cylindrical nanoantennas. Indeed, from this model one can identify two sources of loss in NA systems: the non-radiative loss due to the non-perfect conductivity of materials, and the radiative loss due to the reflections at the antenna ends. Thus, we have introduced now all the elements to proceed with the description of our strategy, which aims at investigating/finding an optimal trade-off between non-radiative and radiative loss to improve the near field enhancement properties of NAs.

2.5.1 Mode Volume

It is worth noticing another very important parameter strictly related to the near field of plasmonic antennas: the mode volume. Indeed, it is of great importance in light-matter coupling experiments since the factor G, called coupling strength (the higher the G factor, the stronger the coupling) is inversely proportional to the mode volume V_{mod}. Obviously, in order to conduct successful light-matter coupling experiments, the G factor must be maximized. In particular, $G = \sqrt{N}\,\mu_N |E_{\text{vac}}|$ [63], [64], where N is the number of particles contributing to the coupling process, μ_N the transition dipole moment of the single particle and

$$|E_{\text{vac}}| = \sqrt{\frac{\hbar\omega}{2}\frac{1}{\varepsilon\varepsilon_0 V_{\text{mod}}}} \tag{2.41}$$

the vacuum electric field, i.e. the field associated with quantum vacuum fluctuations. To maximize G, E_{vac} must be maximized as well, thus minimizing the mode volume V_{mod} defined as [65]

$$V_{\text{mod}} = \frac{\int (\varepsilon(\boldsymbol{r})|E(\boldsymbol{r})|^2)}{\max(\varepsilon(\boldsymbol{r})|E(\boldsymbol{r})|^2)}, \tag{2.42}$$

that is the ratio between the energy density and its maximum value in the whole physical domain, where ε and E are the dielectric permittivity and electric field at the point $\boldsymbol{r}$, respectively. The minimization of the mode volume, necessary to obtain higher vacuum field E_{vac} values and therefore higher coupling strength G, is connected to an increase in the near field enhancement produced by the NA. In fact, by increasing the local field enhancement the overall value of the above ratio decreases, resulting in a reduction of the mode volume. For this reason, strong coupling experiments usually rely on NAs able to achieve high value of field enhancement, such as the end-to-end coupled NAs.

2.6 THz Nanoantennas

As already said, THz spectroscopy is traditionally limited to the study of bulk materials or large aggregates of small particle: at $1\ \mathrm{THz}$ the wavelength is about $300\ \mu\mathrm{m}$, i.e. too large for nano-sized particles. However, thanks to the unique properties of NAs, it is possible to confine THz radiation into sub-wavelength volumes, thus making the interaction with few small particles possible. Such effects has been widely used in THz spectroscopy [31], [32], [35], with significant results.

Despite of the successful experiments conducted so far, the antenna performance, in particular regarding the achievable near field enhancement and mode volume, is not fully optimized, mainly because of the intrinsic lossy nature of metallic nanostructures at these frequencies [36]. As already widely discussed in Section (1.1), in order to improve the NA performance it is possible to

1. use materials characterized by low loss,
2. tune the gap width in end-to-end coupled systems and
3. tune the gap height

However, all cases have considerable constrains:

1. the choice of the metal is most of the times gold as one of the materials with limited loss [40] (but still not perfect) and good chemical stability;
2. NAs in an end-to-end coupled configuration allow for higher field enhancement [41], but too small gaps result in electrons tunneling between the NAs, which in turn reduces the local field [42]; and
3. the shrink of the gap height (i.e., NA width at the gap position) initially leads to higher field enhancement, but extremely small NA widths result in high loss [43].

The last consideration is particularly important at THz frequencies, because of the very large aspect ratio (in this case $AS = L/w$, with $L \approx \lambda/2\mathrm{n}_{\mathrm{eff}}$ antenna length and w antenna width) for NAs resonating in this frequency range [44], [45]. As anticipated, it will be shown in the following that a judicious design of NAs can improve the overall architecture performance.

3 Antenna Tapering Strategy for Near Field Enhancement Improvement[1]

Bow-tie NAs are typically known to produce a smaller field enhancement and larger resonance bandwidth with respect of straight dipolar antennas [34], [50], [51], [53], [67]. By using the Fabry-Perot model introduced in the last chapter, we will demonstrate that a judicious tapering of bow-tie NAs results instead in a beneficial effect for NAs at THz frequencies in terms of higher field enhancement and smaller mode volume. This occurs because tapering the NA structure leads to lower non-radiative loss and higher radiative loss, finally resulting in a positive trade-off that lowers the total power loss characterizing the NA at the optimum tapering angle configuration.

3.1 Quasi-Analytical Fabry-Perot Model for Tapered Nanoantennas

To develop a quasi-analytical model for the architecture under investigation, we have considered a truncated cone made of gold and schematically represented in **Figure 3.1**, with L cone length, θ tapering angle, r fixed radius of the smaller end, $r_\theta = r + L\tan(\theta)$ radius of the larger end that depends on the tapering angle, and $r' = r + z'\tan(\theta)$, local radius of the generic cross section at the coordinate z'. Equation (2.38) allows to calculate the effective refractive index of the mode propagating over the antenna surface of a metallic cylinder. This

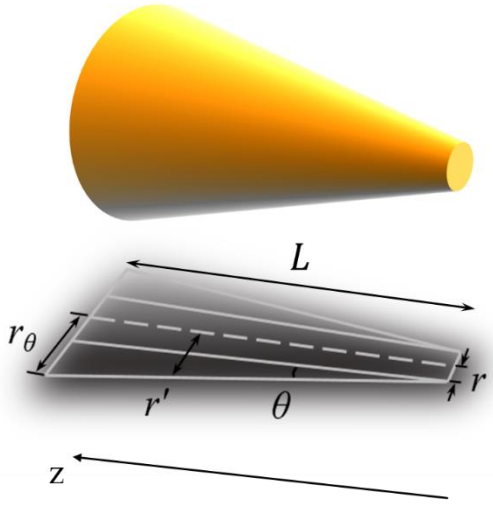

Figure 3.1 Scheme of truncated cone, with L antenna length, θ tapering angle, r radius of the small fixed end, r_θ radius of the larger end, and $r' = r + z'tan(\theta)$ is the radius at the arbitrary coordinate z'.

[1] The discussion and the images of this chapter were adapted from [66] V. Aglieri *et al.*, "Improving nanoscale terahertz field localization by means of sharply tapered resonant nanoantennas," Nanophotonics, vol. 9, no. 3, pp. 683–690, Feb. 2020, doi: 10.1515/nanoph-2019-0459. This article is licensed under the Creative Commons Attribution 4.0 International License.

time, the effective refractive index does not only depend on the dielectric permittivity of the two materials forming the interface, but also on the shape of the truncated cone through the local radius r' and thus varies along the NA. The complex phase-shift accumulated by the mode in a half round-trip can be calculated by integrating the local effective index over the antenna length as:

$$\phi = \kappa_0 \int_0^L n_{\text{eff}}(z)\, dz. \tag{3.1}$$

The electric field at the tip of the truncated cone can finally be calculated as

$$E_{\text{tip}} = E_0 \frac{\left(1 - Re^{2j\phi}\right)\left(1 - e^{2j\phi}\right)}{1 - RR_\theta e^{4j\phi}} \tag{3.2}$$

where $R_\theta \neq R$, when $\theta > 0$, is the reflection coefficient of the larger tip. By using this formula, it is possible to obtain accurate information on the behavior of a surface mode propagating over the truncated cone. Moreover, such model gives qualitatively good predictions on the response of NAs with planar cross-section as shown by the numerical simulation reported in Section (3.2).

The model has been implemented in a Matlab script. In the software, once the material permittivities and the tapering angle θ are specified, the effective index is calculated by evaluating the Equation (2.38) as a function of the local radius r'. The effective index so obtained is a complex quantity, and as widely known, its imaginary part determines the loss that the surface mode suffers during its propagation over the cone. Thus, the non-radiative loss α_{nr} in a round trip (supposing no radiative loss) can be calculated as

$$\alpha_{\text{nr}} = 1 - e^{-4\kappa_0 \int_0^L \text{Im}\{n_{\text{eff}}(z)\} dz} \tag{3.3}$$

The other parameters necessary to calculate the field enhancement of the truncated cone are the complex reflection coefficients R and R_θ at the cone extremities. In particular, such coefficients are calculated by using the effective indexes obtained by using Equation (2.38) in correspondence of the two cone extremities. The reflection at these ends is assumed to occur entirely into the same TM_0 mode, while the electric and azimuthal magnetic fields of the mode propagating over the cylinder and the free-space mode (the mode just outside the antenna) are matched at the antenna extremities with the surrounding medium. Finally, by considering the orthogonality of the cylinder and free-space modes, the reflection coefficient is calculated as

$$R = \frac{1 - U}{1 + U} \tag{3.4}$$

With the U factor containing the result of matching the cylinder and free-space modes at the cylinder end [61]. The mathematical procedure as implemented in the MatLab software is reported in detail in Section (2) of the Appendix of this thesis. The calculation of the reflection coefficient has been implemented in MatLab two times, the first one to calculate the reflection coefficient R at the smaller cylinder end with fixed radius, and the second one to calculate the reflection coefficient R_θ at the larger tip. The R and R_θ values give access to the radiative loss α_r per round trip (supposing no non-radiative loss) calculated as

$$\alpha_\mathrm{r} = (1 - R^2)(1 - R_\theta^2) \tag{3.5}$$

Once the effective index of the cone and the reflection coefficients at its extremities are obtained, the electric field at the tip is calculated following Equation (3.2).

The model has then been used to calculate the electric field at the small tip, for a truncated cone with length $L = 100\,\mu\mathrm{m}$ (resonating at around $1\,\mathrm{THz}$), small fixed radius $r = 50\,\mathrm{nm}$, made of gold with plasma frequency $f_\mathrm{p} = 2080\,\mathrm{THz}$, and carrier life time $\tau = 18\,\mathrm{fs}$ [68]. The result is shown in **Figure 3.2 (a)** as a function of the tapering angle θ. Here the field enhancement increases as the tapering angle θ increases until a maximum is reached that occurs in correspondence of the optimum angle θ_opt. For $\theta > \theta_\mathrm{opt}$ the field enhancement decreases. Such behavior is due to the trade-off between decreasing non-radiative loss α_nr and increasing radiative loss α_r. In **Figure 3.2 (b)** are shown the power coefficients trends for the non-radiative γ_nr (blue curve) and radiative γ_r (red curve) loss (not that these coefficients are equal to 1 for no non-radiative/radiative loss, respectively). These are introduced to calculate the total loss power $\Gamma = 1 - \gamma_\mathrm{r}\gamma_\mathrm{nr}$ (black curve), which gives a quantitative idea of the overall loss relaxation while tapering the structure, and can be related to the loss coefficients reported in Eqs. 3.4 and 3.5 as follows:

$$\gamma_\mathrm{nr} = e^{-4\kappa_0 \int_0^L \mathrm{Im}\{n_\mathrm{eff}(z)\}dz} = 1 - \alpha_\mathrm{nr}, \tag{3.6}$$

$$\gamma_\mathrm{r} = R^2 R_\theta^2 = R^2 + R_\theta^2 - 1 + \alpha_\mathrm{r}. \tag{3.7}$$

By increasing the tapering angle θ, the radiative loss α_{r} (γ_{r}) increases (decreases), but - at the same time – the non-radiative loss α_{nr} (γ_{nr}) decreases (increases) at a higher rate, thus resulting in the net reduction of the total power loss, as shown by the black curve in **Figure 3.2 (b)**, and consequently in the increasing of the field enhancement. The total power loss is minimized, at the optimum tapering angle θ_{opt} where the maximum in field enhancement is achieved. For large angles ($\theta > \theta_{\mathrm{opt}}$) the decrease in the non-radiative loss is not sufficient to compensate the increase in radiative loss, thus resulting in the net increase of the total power loss and the reduction of the field enhancement.

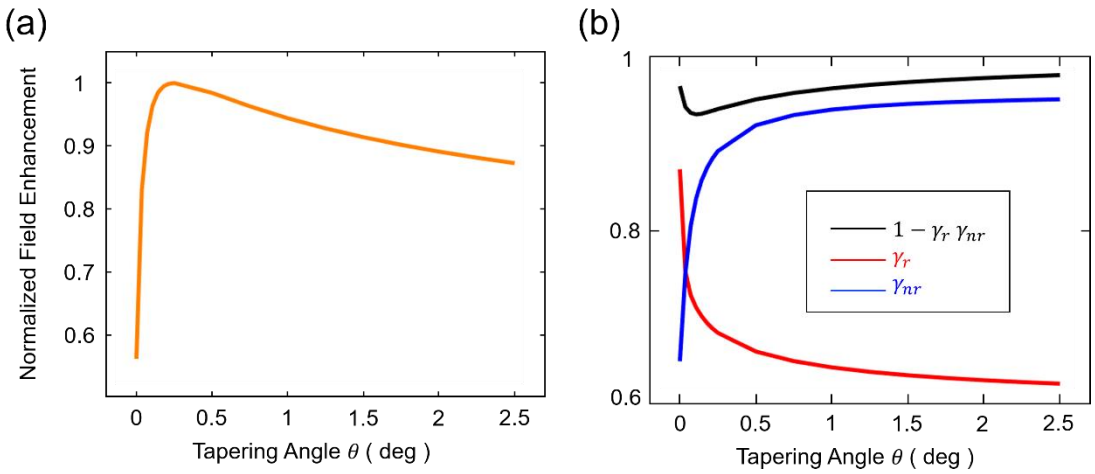

Figure 3.2 (a) Normalized near field enhancement for a $100\ \mu m$ long gold truncated cone, with $r = 50\ nm$ radius of the smaller tip and tapering angle θ varying between 0 and 2.5 deg. The near field initially increase by increasing the tapering angle, reaching a maximum. For larger tapering angles, the near field decreases. (b) Trend of the power coefficient for radiative (red) and non-radiative (blue) loss; in black the total power loss behavior reveals a minimum in the total loss due to an optimum trade-off between a decreasing non-radiative loss and an increasing radiative loss.

The tapering strategy affects both non-radiative and radiative loss factors because when the tapering angle is varied, both the effective index n_{eff} and the reflection coefficient at the larger end R_θ change. As **Figure 3.3** shows, the imaginary part of the effective refractive index n_{eff} decreases as the tapering angle increases (black curve), resulting in the decrease of the non-radiative loss (lower imaginary effective index values correspond to lower material losses). At the same time, the reflection coefficient R_θ decreases (red curve), and consequently the radiative loss in the free-space increases (lower reflection coefficient values correspond to a better transmission towards free space). Therefore, the parameters to consider are not only the values of the quantities $\mathrm{Im}\{n_{\mathrm{eff}}\}$ and R_θ but also the rate at which these two quantities change. To summarize:

- for $0 < \theta < \theta_{\mathrm{opt}}$ the non-radiative loss decreases, and it occurs at a faster rate than the one governing the increase of the radiative loss, resulting in a net decrease of the total power loss and thus to the increase of field enhancement.

- for $\theta = \theta_{\mathrm{opt}}$ the trade-off between the two loss factor is optimized obtaining the minimum achievable total power loss, that is, the maximum field enhancement.
- for $\theta > \theta_{\mathrm{opt}}$ the rate at which the radiative loss increases is higher than that governing the decreasing of non-radiative loss, leading to an increase in the total power loss and a reduction of the field enhancement.

In conclusion, if a metal cone is properly tapered, it is possible to improve the field enhancement accumulated at its smaller tip. Now, it is important to study the quantitative amount of field enhancement that is possible to achieve. The theoretical demonstration of field enhancement improvement is only the first step toward the more comprehensive study of such tapering strategy that will be extended on antennas that can be effectively prepared using planar fabrication technologies. In the following, the applicability of such method to such NAs (i.e., NAs characterized by squared cross-section geometry suitable for device fabrication) on a silicon substrate is presented by employing a simulation platform. Thanks to the simulation results, it is also possible to extract the design for the fabrication of real samples.

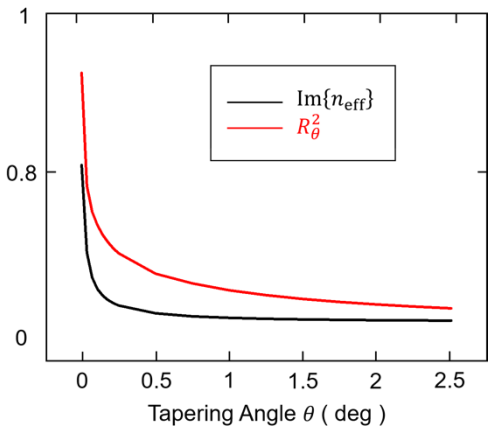

Figure 3.3 Imaginary part of the effective refractive index n_{eff} (black curve) and reflection coefficient at the larger end R_θ (red curve) trend as a function of the tapering angle θ.

3.2 Design of Tapered Gold Nanoantennas Resonating at THz frequencies

The quasi-analytical model presented above is an excellent tool that gives us access to the information regarding the behavior of gold NAs when the structure is tapered. Nonetheless, it produces only a qualitatively description of the NA response, not suitable for the design of actual planar antennas. In particular, planar gold NAs, characterized by squared cross-section, should be designed instead. For this reason, the design of resonant bow-tie NAs has been obtained by using the commercial software COMSOL Multiphysics. Such simulation platform is a Finite Element Method (FEM)–based software, which allows to numerically find solutions to partial differential equations to describe space- and time-

dependent problems, when an analytical method is not applicable. This method does not treat the antenna as a unique entity, but divides them in more pieces (meshing elements) and solve the equations for each piece. In this way, the results obtained are quantitatively precise, suitable for the fine design of actual devices. Moreover, in order to achieve the maximum field enhancement possible, the configuration chosen is the end-to-end coupled bow-tie. For this reason, paired bow-tie NAs are considered from now on.

The physical model implemented in COMSOL is formed by three elements: substrate, bow-tie NAs pair, and superstrate, as shown in **Figure 3.4**. The substrate material chosen is a high resistivity silicon because of its almost constant permittivity ($\varepsilon_{\mathrm{Si}} = 3.42$) and its low absorption in the THz regime. The substrate plane is around $130\ \mu\mathrm{m}$ wide and $40\ \mu\mathrm{m}$ long, while is $102\ \mu\mathrm{m}$ thick in the perpendicular direction of the bow-ties plane. The upper layer is composed by air with $\varepsilon_{\mathrm{air}} = 1$, still $130\ \mu\mathrm{m}$ wide and $40\ \mu\mathrm{m}$ long in the bow-ties plane, and $287\ \mu\mathrm{m}$ thick. The bow-tie NAs have been chosen to resonate around $1\ \mathrm{THz}$, they are $L = 45\ \mu\mathrm{m}$ long, $t = 60\ \mathrm{nm}$ thick and $w_{\mathrm{tip}} = 100\ \mathrm{nm}$ wide at the gap extremities. The gap size has been designed to be $30\ \mathrm{nm}$ in width. The outer ends width of bow-tie NAs depends on the tapering angle as $w_{\mathrm{ext}} = 2L \cdot \tan(\theta) + w_{\mathrm{tip}}$. The material chosen for the bow-tie NAs is gold with plasma frequency $f_{\mathrm{p}} = 2080\ \mathrm{THz}$ from Ref. [68], and a carrier life time $\tau = 5.8\ \mathrm{fs}$ obtained from the fitting of the experimental response of preliminary fabricated samples. The Floquet periodic conditions at the side-walls of the model have been set to emulate the situation of an infinitely extended array of bow-tie paired NAs, and the distances between

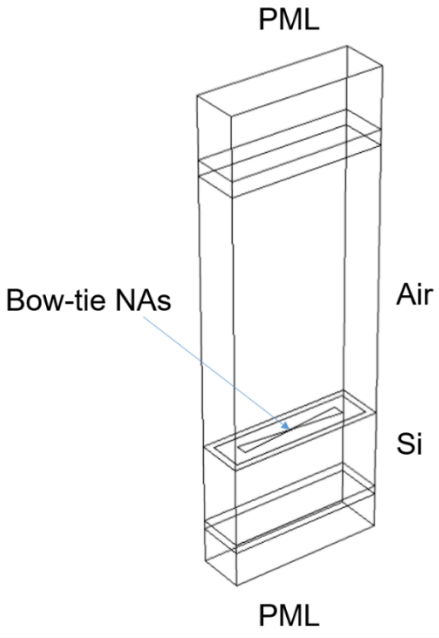

Figure 3.4 Sketch of the physical model used in COMSOL to simulate the bow-tie NA pair. Below and above the NA pair are placed the silicon substrate and air superstrate, respectively. At the bottom and top extremities of the system are placed the PML layers to avoid reflection artifacts.

adjacent bow-tie NAs ($130\,\mu m$ along the x-axis and $40\,\mu m$ along the y-axis) have been chosen to minimize the inevitable cross-talk in periodic structures [33]. At the bottom and at the top of the model, a perfectly matched layer (PML) has been introduced in order to eliminate spurious reflections. Finally, the system is illuminated from the top with THz radiation between 0.5 and $2\,THz$. The far field transmission is retrieved by placing a power detector below the substrate, while the near field is obtained from a probe placed exactly in the center of the gap between the NAs.

The NA pair sketch is shown in **Figure 3.5 (a)**. The simulated tapering angles are between 0 and 8 degrees. In **Figure 3.5 (b),** the simulated transmission curves as a function of the frequency and for several tapering angles are shown. The transmission value at resonance decreases as the tapering angle θ is increased. This is due to a better resonator behavior as well as a larger geometrical area of the gold bow-tie NA pair for large tapering angles.

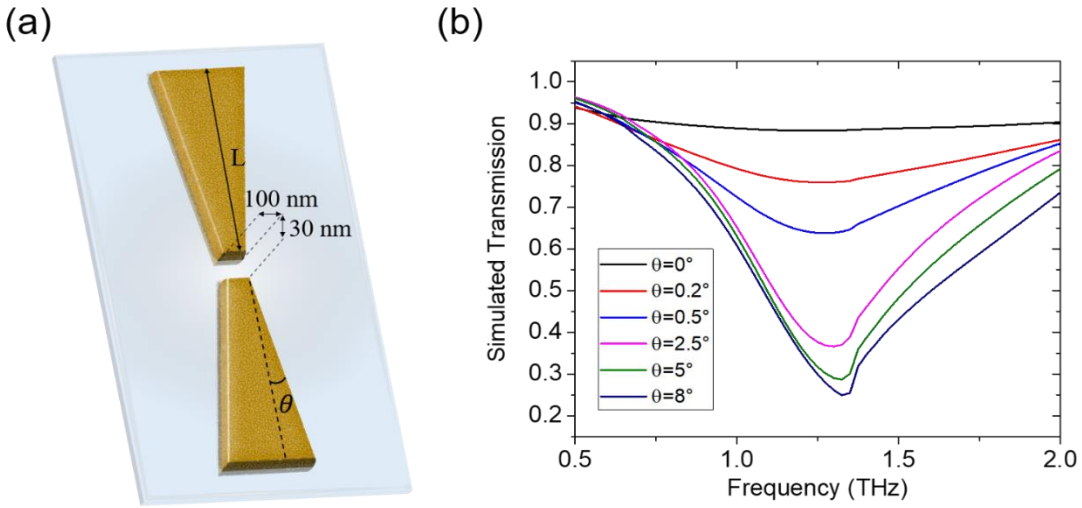

Figure 3.5 (a) Sketch of the NA pair on top of the silicon substrate. (b) Simulated transmission spectra for a selected number of tapering angles. The transmission at resonance decreases as the tapering angle increases.

The near field calculated at the very center of the gap is shown in **Figure 3.6 (a)** in a 2D map as a function of the tapering angle and the frequency. It can be seen that for the case of straight dipolar antenna ($\theta = 0$), the near field does not experience any resonance within the frequency range of study due to the very high loss that characterized such gold NAs with aspect ratio $AS \approx 450$. Thus, the non-tapered NA pair presents a field enhancement value only due to the so-called “lightning-rod effect” [69] and its response cannot be tuned by varying the antenna length. **Figure 3.6 (b)-(g)** shows the near field distribution at the resonance frequency for six selected angles ($\theta = 0°,\ 0.2°,\ 0.5°,\ 2.5°,\ 5°,\ 8°$). As already stated, in the case of straight dipolar antenna only a small amount of field is accumulated in the gap, while for larger angles the field enhancement is increasingly accumulated there. In

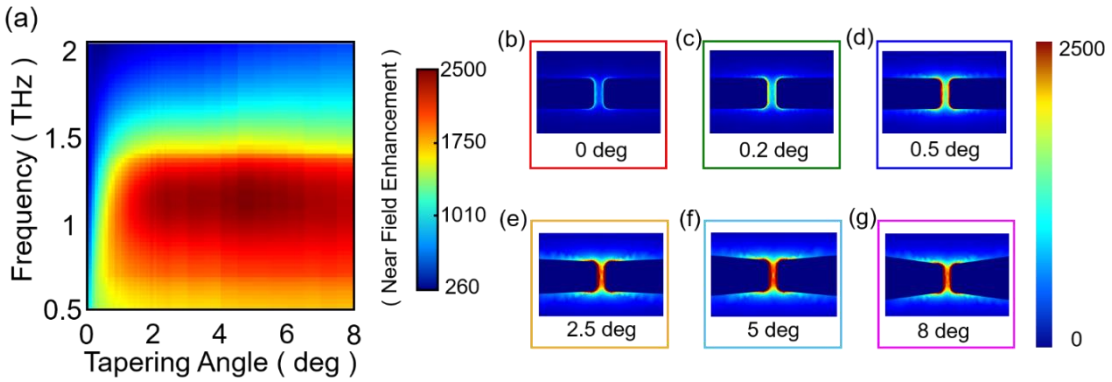

Figure 3.6 (a) Near field enhancement 2D map as a function of the tapering angle and frequency. (b)-(g) Near field distribution inside the gap between paired NAs at the resonance frequency.

fact, by increasing the angle at 0.2° the loss decreases and a resonance appears. By further increasing the tapering angle the field enhancement at the center of the gap also increases until a maximum is reached at the optimum angle, that for gold NA pair has been found to be $\theta_{\mathrm{opt}} = 3° - 5°$. For larger angles instead, the near field decreases. **Figure 3.7 (a)** shows the field enhancement peaks as a function of the tapering angle: the maximum near field enhancement is ~ 2.2 times higher than the enhancement obtained from the straight NAs pair, and ~ 1.7 times higher than the first resonant bow-tie NA pair at $\theta = 0.2°$. Thus, the tapering strategy first analyzed with the quasi-analytical model is here confirmed to improve the NA performances also in the case of simulated nanostructures with “rectangular” section. It should be underlined that the resonance frequency depends on the tapering angle as well. From the **Figure 3.7 (b)** the resonance frequency follows a similar trend of the field enhancement. Initially, the resonance frequency increases by increasing tapering angles due to a decrease in the effective optical path length for the surface wave, which results in a resonance blue-shift. For tapering angles greater than the optimum angle, the resonance

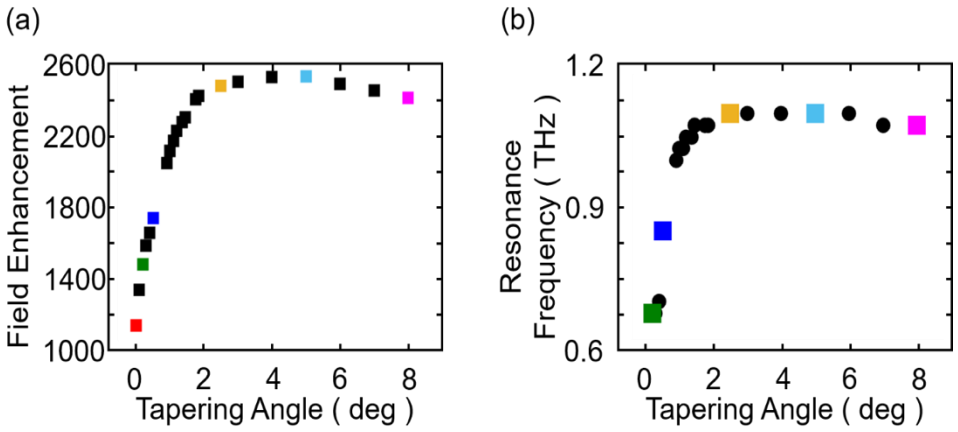

Figure 3.7 (a) Field enhancement peak as a function of the tapering angle. (b) the resonance frequency of the NA bow-ties as a function of the tapering angle.

frequency experiences a slight red-shift.

It is worth to be underlined that this method has been demonstrated to also improve the performance of antennas that are over-damped in their straight configuration, as it is the case of the antennas studied in this paragraph.

Along with the field enhancement, the second important improvement consists in the decrease of the mode volume. In **Figure 3.8 (a)** is depicted a sketch of the mode volume V_{mod} and the geometrical volume of the gap $V_{\mathrm{geo}}^{\mathrm{gap}}$ (that is, $30\times60\times100$ nm). A 2D map of the volume ratio $V_{\mathrm{ratio}} = V_{\mathrm{mod}}/V_{\mathrm{geo}}^{\mathrm{gap}}$ as a function of the tapering angle and resonance frequency is presented in **Figure 3.8 (b)**. The map reveals a reduction of the volume ratio of 7 times with respect to straight dipolar antennas, with a mode volume only slightly more than 100 times the geometrical volume $V_{\mathrm{geo}}^{\mathrm{gap}}$. This is a really impressive result considering that the NAs total volume $V_{\mathrm{geo}}^{\mathrm{tot}}$ is huge compared to the $V_{\mathrm{geo}}^{\mathrm{gap}}$ (varying between 3000 times the $V_{\mathrm{geo}}^{\mathrm{gap}}$, for NAs with $\theta = 0°$, to ~190000 times, for NAs with $\theta = 8°$). In **Figure 3.8 (c)** is presented the volume ratio as a function of the frequency close to the minimum value, while in **Figure 3.8 (d)** is presented the minimum peak behavior of the volume ratio as a function of the

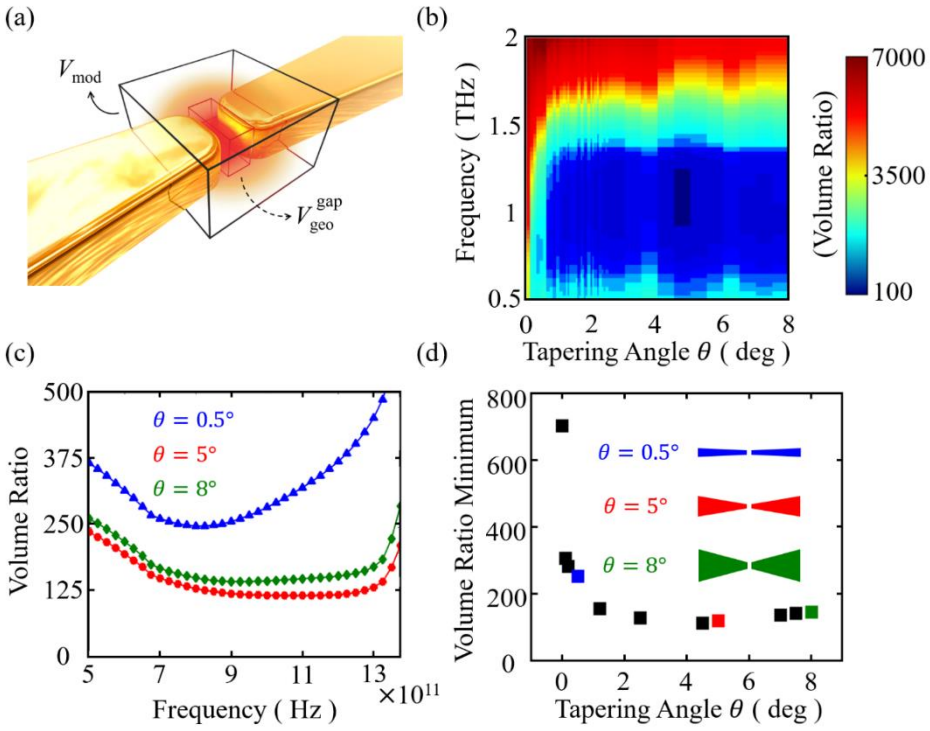

Figure 3.8 (a) Mode volume V_{mod} and geometrical volume of the gap V_{geo}^{gap} represented in the sketch of the gap between NAs. (b) 2D map of the volume ratio as a function of the tapering angle and frequency. (c) Volume ratio of the $\theta = 0.5, 5$ and $8°$ NA bow-tie as a function of frequency, in a range close to the resonance frequency. (d) Volume ratio minima as a function of the tapering angle.

tapering angle θ.

With these factors of improvement, the tapering strategy for gold bow-tie NAs appears to be an effective method to enhance light-matter interaction at the nanoscale in the THz regime. As a final step, to demonstrate the validity of the tapering approach and use it into real-world light-matter experiments, we have fabricated and characterized five representative samples. Details about this are given in Chapter 4.

3.3 Tapering Strategy at Higher Frequencies

The tapering strategy is a universal route towards the optimization of NAs also at higher frequencies. This can be shown simulating the bow-tie NAs performance by varying the tapering angle in the IR range. In **Figure 3.9 (a)** is shown the near field enhancement as a function of frequency produced in the $30\ \mathrm{nm}$ wide gap between two NAs, $2\ \mu\mathrm{m}$ long, $40\ \mathrm{nm}$ thick and $50\ \mathrm{nm}$ wide (at the gap), resonating around $\lambda_{\mathrm{res}} = 6.6\ \mu\mathrm{m}$, that is $f_{\mathrm{res}} = 45.5\ \mathrm{THz}$, on a calcium fluoride (CaF_2, with refractive index $n_{CaF_2} = 1.35$) substrate, with periodicity $4\ \mu\mathrm{m}$ along the y-axis and $8.03\ \mu\mathrm{m}$ along the x-axis. Note that the notches present on the field enhancement response at around $37\ \mathrm{THz}$ and $56\ \mathrm{THz}$ are the signature of lattice (array) modes [70], [71] in the periodic configuration considered here. In **Figure 3.9 (b)** is shown the near field enhancement peak behavior as a function of the tapering angle θ. As already seen for the THz NAs, the near field increases as the tapering angle increases until a maximum is reached. Again, for too large angles (larger than optimum angle) the near field enhancement decreases.

In this case, the near field enhancement value found for the optimum angle is 20% higher

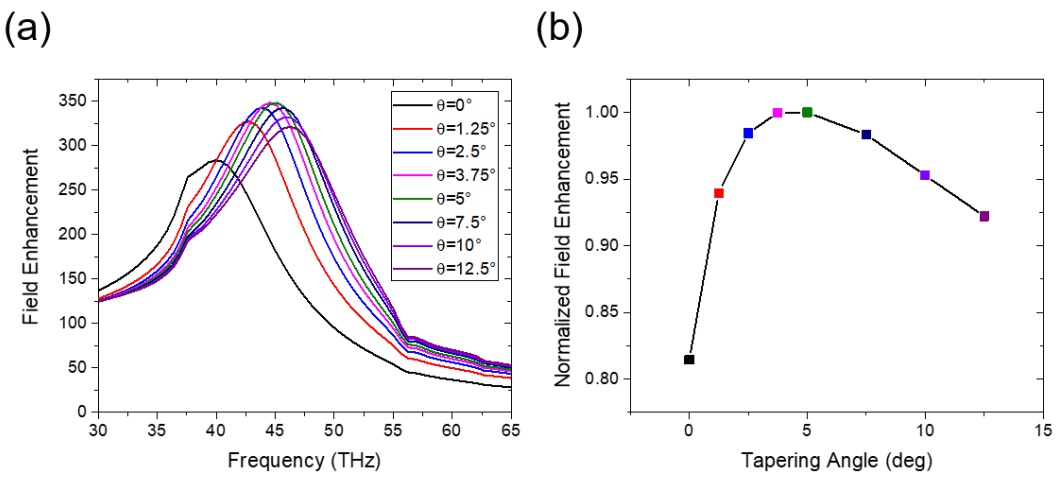

Figure 3.9 (a) Near Field enhancement as a function of the frequency and (b) near field enhancement peaks as a function of the tapering angle θ. The antenna is $2\ \mu m$ long, $40\ nm$ thick and $50\ nm$ wide. The resonance frequency is found to be around $\lambda = 6.6\ \mu m$.

than the straight antenna case. Therefore, the improvement factor is smaller than in the case of THz bow-tie NAs. This is connected to a significantly smaller aspect ratio of IR antenna, i.e. $AS_{\mathrm{IR}} = 40$, with respect to the one presented by a THz NA, that is, $AS_{\mathrm{THz}} = 450$, the aspect ratio giving an immediate idea about the mismatch between the radiation wavelength (connected with the resonant antenna length) and the lateral cross section of the NA. Another consequence of the smaller aspect ratio is that the $\theta = 0^\circ$ NA in the IR case still resonates, differently of what has been found in the THz regime for the specific case considered above, where the straight dipolar NAs present a near field enhancement only due to the lightning rod effect. Overall, we can conclude that the tapering strategy can be an effective tool to also improve NAs with high aspect ratios operating in the IR.

4 THz Nanoantennas: Fabrication and Characterization[2]

4.1 Gold Bow-tie Nanoantennas Fabrication

The fabrication processes have been conducted in the Clean Room Facility of the Istituto Italiano di Tecnologia (Genoa, Italy). Based on the simulation results, five samples design have been chosen for the experimental validation of the tapering strategy, that is, gold bow-tie NA pairs with tapering angle: 0, 0.2, 0.5, 2.5 and 5°. A 500-µm-thick silicon sample characterized by high resistivity (10000 Ω × cm) has been chosen as substrate because of its negligible loss and chromatic dispersion at THz frequencies.

The main equipment and materials employed for the fabrication of gold bow-tie NAs are

- Electronic Resist, aluminum, titanium and gold,
- Spin-Coater,
- Physical Vapor Deposition,
- Electron Beam Physical Vapor Deposition, and
- Electron Beam Lithography.

In the Appendix is reported a brief description of the clean room environment and the main equipment and materials used for the fabrication of gold bow-ties.

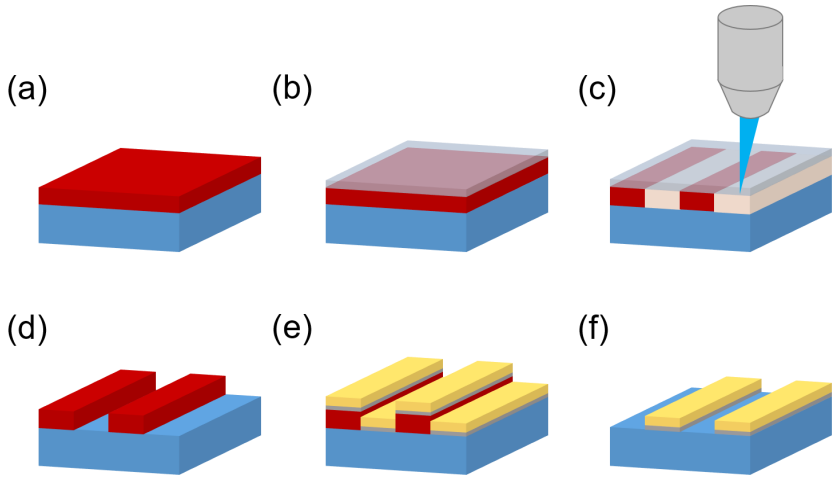

Figure 4.1 Process flow steps employed during the fabrication gold paired NAs. (a) A silicon substrate is cleaned and prepared for the lithography by depositing a PMMA layer. (b) On top of the electronic resist is deposited an aluminum thin film to avoid charging issues during the lithography step. (c) The PMMA layer is patterned by using the E-Beam lithography system. (d) The aluminum film is removed and the PMMA layer is developed obtaining the desired mask. (e) A titanium adhesion layer and a gold film are deposited on top of the mask. (f) The mask is removed and the gold structures are obtained.

[2] The discussion and the images of this chapter were adapted from [66] V. Aglieri *et al.*, "Improving nanoscale terahertz field localization by means of sharply tapered resonant nanoantennas," Nanophotonics, vol. 9, no. 3, pp. 683–690, Feb. 2020, doi: 10.1515/nanoph-2019-0459. This article is licensed under the Creative Commons Attribution 4.0 International License.

4.1.1 NAs Fabrication Process

The process steps followed for this fabrication are summarized in **Figure 4.1**.

The process starts by cutting a silicon wafer into $1 \times 1\ \mathrm{cm}^2$ substrates subsequently ultrasonic-cleaned in acetone, Isopropyl alcohol (IPA) and high-purified water (obtained from a Milli-Q® system). Then the substrates have been furtherly cleaned with an oxygen plasma treatment to remove the remaining impurities on the substrate surface.

PMMA A4/Anisole 2:1 electronic resist has been spin-coated, at 1800 rpm for 1 minute. Then the sample is baked at 180° for 7 minutes (**Figure 4.1 (a)**) to evaporate the remaining solvent. On top of the electronic resist is deposited a thin aluminum layer via vapor phase deposition (**Figure 4.1 (b)**) necessary to avoid charging effects due to the limited conductivity of the silicon substrate employed. Once the aluminum layer is deposited, the sample is loaded inside a Raith 150-two electron-beam direct writing system. The lithography has been performed with high resolution parameters, required by the small features of the gap. The beam was set to deliver $500\ \mu\mathrm{C/cm}^2$ at $20\ \mathrm{keV}$, with $10\ \mu\mathrm{m}$ large aperture and $100 \times 100\ \mu\mathrm{m}^2$ writing field size (**Figure 4.1 (c)**). After the lithography, the aluminum layer is removed in Potassium hydroxide (KOH) 1 molar (high-purified water has been used to rinse the sample). Then, the electronic resist is developed in MIBK:IPA 1:3 for 30 sec (**Figure 4.1 (d)**) and stopped in IPA. The sample was coated with a titanium adhesion layer of $5\ \mathrm{nm}$ and then with a 60-nm-thick gold film through e-beam vapor phase deposition

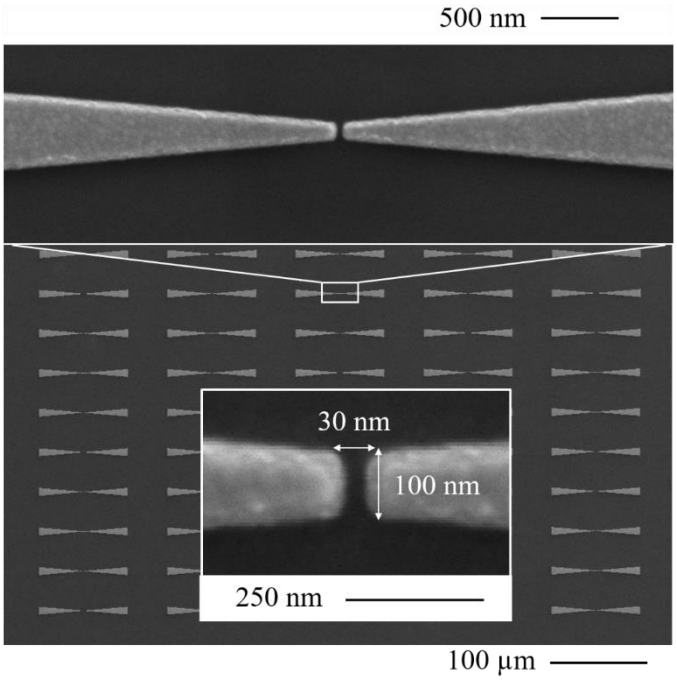

Figure 4.2 SEM image of part of the $5 \times 5\ mm^2$ sample covered with gold bow-ties with tapering angle $\theta = 5^\circ$. Top inset shows a NAs image close to the gap. Bottom inset shows a high magnification image of the 30-nm-wide and 100-nm-height gap between the bow-tie NAs.

(**Figure 4.1 (e)**). Then, the electronic resist has been lifted-off in hot acetone, and finally cleaned with an oxygen plasma treatment (**Figure 4.1 (f)**). The final result is shown in scanning electron microscope (SEM) images of **Figure 4.2**: the main image (bottom) shows the gold bow-tie NAs fabricated on top of a silicon substrate on an overall area $5 \times 5\ \mathrm{mm}^2$ wide. The top inset shows a closer view of the bow-ties near the gap, and the lower inset an high-magnification of the gap between NAs highlighting the geometrical sizes.

The great difficulty in the fabrication of gold bow-tie NAs resides in their huge aspect ratio. As already shown, in order to obtain antennas resonating around $1\ \mathrm{THz}$, NAs have to be designed to be $45\ \mu\mathrm{m}$ in length. At the same time, to obtain appreciable values of field enhancement, the NAs-coupled configuration presents gap features of nanometric scale. Therefore, in order to achieve nanometric precision during the lithography, the electron-beam system has to be set up properly, i.e., by choosing small beam aperture, small writing field, high electron voltage accelerations, etc. When the system is so programmed, also the large micrometric features are lithographically exposed with the same resolution and precision in an even extremely large area ($5 \times 5\ \mathrm{mm}^2$). For example, if the tapering angle $\theta = 5°$ is chosen, the large outer extremities of the bow-ties are $8\ \mu\mathrm{m}$ in length, making the lithography challenging (the e-beam lithography process take approximately 6 hours for the straight antenna patterning up to 26 hours for the larger tapering angles).

4.2 Experimental Characterization in the THz Regime

4.2.1 Experimental Setup

The experimental characterizations have been performed in a transmission mode using a THz time domain spectroscopy (TDS) setup at the Laboratory for IR and THz Photonics of

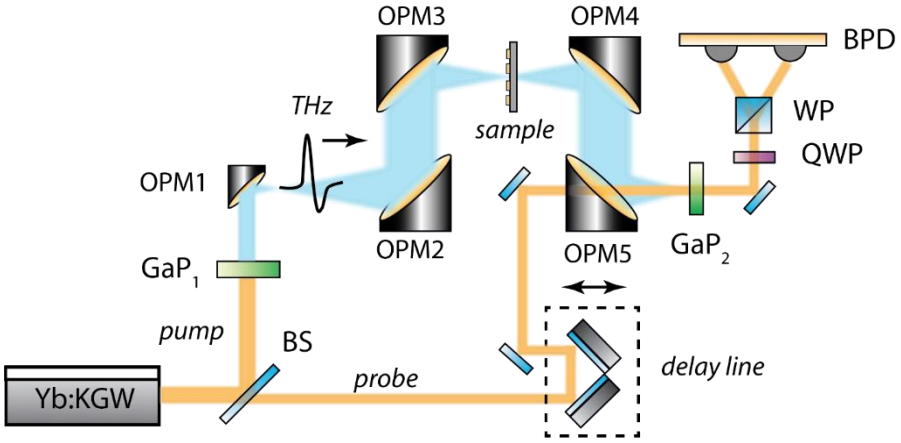

Figure 4.3 Schematic of the GaP-based time-domain spectroscopy setup used for the characterization of bow-tie NA samples.

INRS-EMT (Varennes, Quebec). The setup is sketched in the scheme of **Figure 4.3**. It consists of an amplified Ytterbium-based laser, emitting 170-fs-long pulses centered at 1030 nm with pulse energy of about 1 mJ. The pulse from the laser is divided, by means of a beam splitter 80:20 (BS), into two beams: the pump and the probe. The pump beam is directed onto a gallium phosphide (GaP1) generation crystal in order to generate THz radiation via optical rectification [2]. Once emitted, the THz beam is focused onto the sample under investigation. Passing through the sample, the THz beam is collected and finally focused on another 500-µm-thick GaP detection crystal (GaP2) by using off-axis parabolic mirrors (focal length OPM1: 0.5'', OPM2: 6'', OPM3 and OPM4: 3'', OPM5: 2''). The THz waveforms are retrieved as a function of relative delay between the THz beam and the probe pulses by employing the electro-optic sampling technique [2]. In the detection crystal, by exploiting the Pokels effect, the THz beam induces a change in refractive index proportional to its electric field strength. Thus, an optical probe beam sees its polarization state modified by passing through the GaP detection crystal when the THz electric field is also present. Finally, the polarization state of the probe beam is analyzed using a quarter-waveplate (QWP), a Wollaston prism (WP), which separates the main polarization components, and a balanced photo-detector (BPD) that analyses the difference in the two components. By doing so, as a function of the delay between the optical probe and the THz pulses, the THz electric field waveform in time is directly retrieved. The corresponding spectra is then numerically calculated by taking the Fourier transform of the corresponding temporal traces. In order to reduce the noise during the measurements, a lock-in amplifier is employed (not included in the scheme of **Figure 4.3** for the sake of simplicity) and the transmission spectra are collected purging the system with nitrogen (to avoid water vapor absorption) and by normalizing them to the transmission spectrum of a bare silicon substrate.

4.2.2 Experimental Transmission Spectra

The results for the $\theta = 0, 0.2, 0.5, 2.5$ and $5°$ gold bow-ties are shown in **Figure 4.4**. The straight dipolar NA pair ($\theta = 0°$) does not present any resonance (overdamped response), mainly due to the very high losses characterizing this case. Instead, starting from the bow-tie pair at $\theta = 0.2°$, a resonance appears at around $1.24\ \mathrm{THz}$. Increasing the tapering angle, the transmission experiences a decrease in correspondence of the resonance frequency, mainly due to the larger area of the antenna with increasingly larger angle that results in higher interaction with the THz radiation and thus in a lower THz transmission signal.

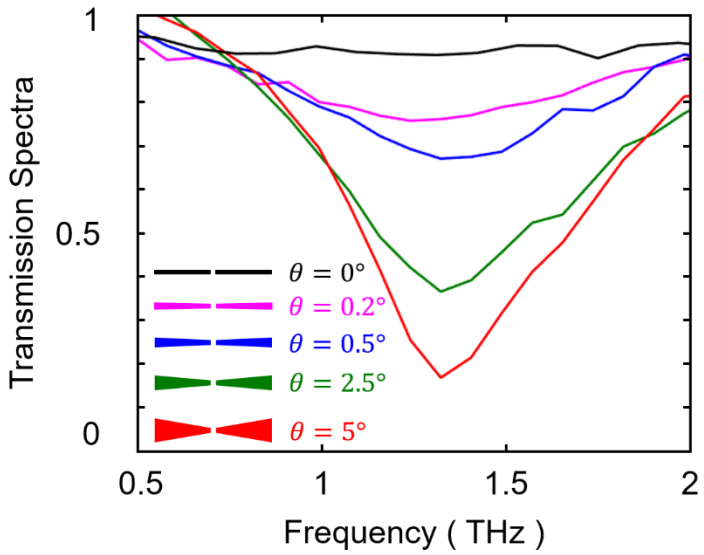

Figure 4.4 Experimental transmission spectra obtained by THz-TDS characterization of gold bow-ties. The transmission minimum decrease as the tapering angle increase, due to the larger gold area interacting with the incoming THz radiation.

THz-TDS is a valuable technique to retrieve information in the THz domain. However, it only gives far field information about the sample under study. Therefore, it is not possible to retrieve information about the near field behavior of the fabricated NAs. In order to extract valuable information from the experimental characterization, it is important to retrieve the full width at half maximum (FWHM) values for the resonance. This is because the FWHM is

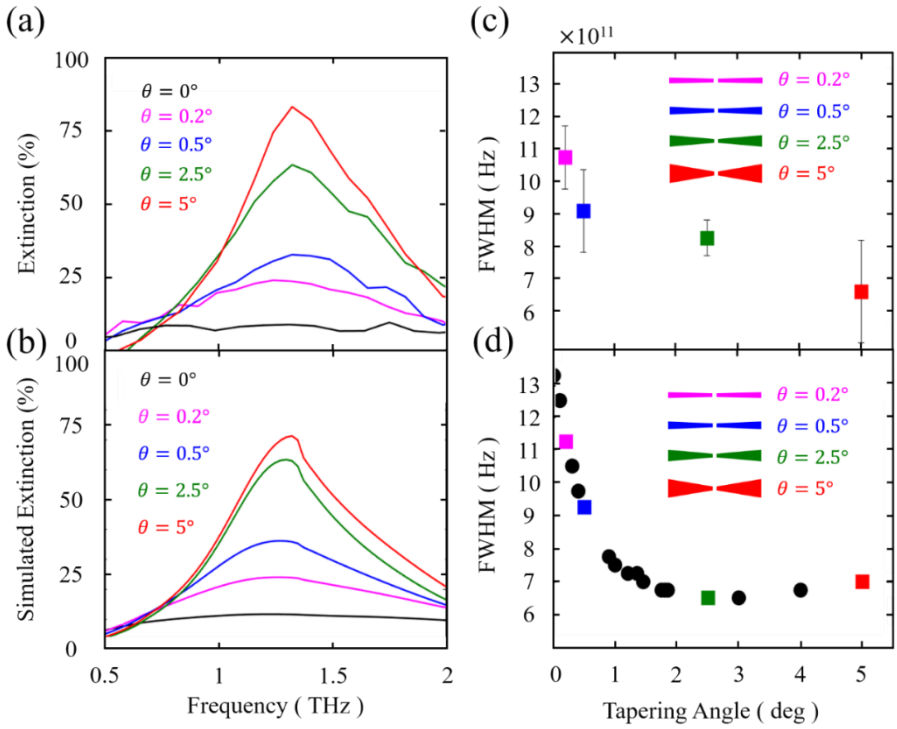

Figure 4.5 (a)-(b) Experimental and simulated extinction spectra, respectively. (c)-(d) FWHM values obtained from the extinction spectra: colored squares correspond to the fabricated sample with $\theta = 0.2, 0.5, 2.5$ and 5°. The configuration $\theta = 0^\circ$ has not been considered in figure (c) because it was not possible to retrieve a meaningful FWHM value for the experimental overdamped case.

directly related to the total loss of the system, and thus it can be employed to evaluate the performance of the fabricated antennas. In **Figure 4.5 (a)-(b)** are shown the extinction spectra, defined as $1-T$, with T the transmission spectrum, of the experimental and simulated results, respectively. The two series of spectra are very similar and present the same behavior varying the tapering angle. **Figure 4.5 (c)-(d)** show the FWHM values obtained from the experimental and simulation extinction spectra, respectively. As it can be seen, there is a good agreement on the behavior of the losses, in fact, in the experimental case a reduction of the FWHM occurs while the tapering angle is increased, revealing a reduction of the NAs total loss. Therefore, it can be stated that the prediction of the quasi-analytical model, and the results of the numerical simulations are experimentally confirmed.

Once the experimental validation of the tapering strategy beneficial effects has been obtained, this method has been applied for the design of ITO shuttle antennas and gold NAs for strong coupling experiments, as shown in the following.

4.3 Tapering Strategy for the Loss Relaxation in Conductive Oxide Antennas

ITO is a promising material for the fabrication of plasmonic antennas because of its robustness with respect of other common material for plasmonics. This property makes ITO a good substitute of gold to make plasmonic antenna for nonlinear experiments at THz frequencies. In fact, it is well known that gold antennas get damaged when exposed to intense THz light [72]. However, ITO is characterized by a much smaller charge carrier concentration, and even if properly doped, it is not possible to reach the same carrier concentration of gold [39]. Nevertheless, by means of the tapering strategy, ITO shuttle antennas are here shown to successfully resonate in the THz regime. First, the tapering angle has been calculated through simulations by using the CST Studio Suite software, and is a result of the balance between non-radiative and radiative loss, in this case including the

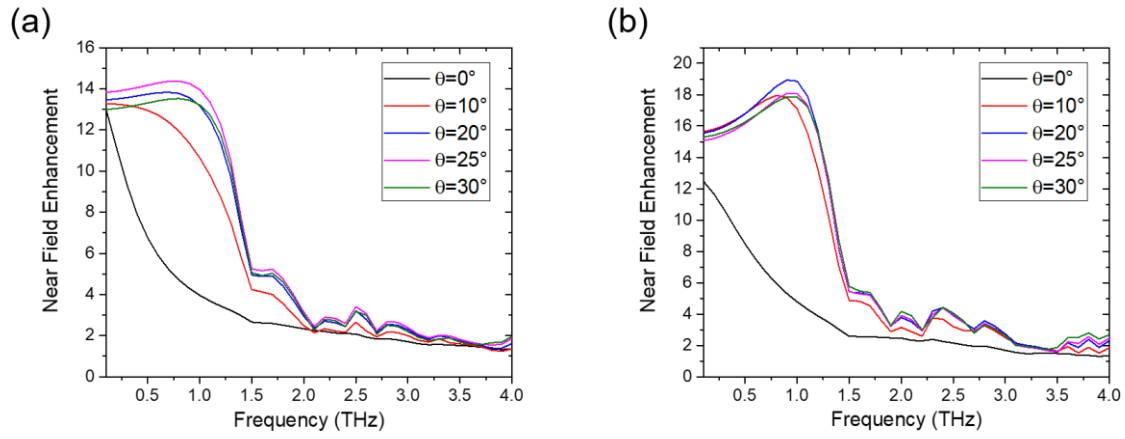

Figure 4.6 Near field enhancement of the (a) $200\,nm$ thick and (b) $400\,nm$ thick ITO shuttle antennas varying the tapering angle from $\theta = 0^\circ$ to $\theta = 30^\circ$.

scattering at the central larger section. The antennas have been designed to be $45\ \mu m$ long, characterized by an antenna width of $1\ \mu m$ at the smaller end, and separated by a $1\ \mu m$ wide gap. In **Figure 4.6 (a)** and **(b)**, the near field enhancements for the $200\ nm$ thick and the $400\ nm$ thick ITO shuttle antenna thickness are presented, respectively. As it can be seen, for the $200\ nm$ thick case the optimum angle is for $\theta = 25°$, whereas in the $400\ nm$ thick case the maximum is found at the tapering angle $\theta = 20°$. Thus, such parameter have been chosen to fabricate and characterize a shuttle antenna made of ITO. It has to be noted the considerable difference between the optimum tapering angles between gold and ITO antennas. In the latter case, the optimum angle results to be larger because of the much higher loss characterizing the ITO, that finally requires higher tapering angle to reduce the overall loss in order to resonate. Moreover, the difference in the tapering angle between the $200\ nm$ and the $400\ nm$ thick antennas is due to the higher loss of the $200\ nm$ thick shuttle caused by the smaller thickness. In **Figure 4.7 (a)** is reported an SEM image of a fabricated sample of ITO shuttle antennas. The results of experimental THz transmission spectroscopy are shown in **Figure 4.7 (b)**, for two ITO shuttle samples, characterized by a 200 nm (black line) and 400 nm (red line) thick antennas. As it can be seen, even if ITO still suffers from very high loss, a resonance occurs between 1 and $1.25\ THz$ thanks to the optimization of the structure. As a further confirmation of the beneficial effects of the tapering strategy on the overall performances of the ITO shuttle antennas, also antennas with tapering angle $\theta = 0°$ (straight dipolar antennas) have been fabricated and characterized. However, straight ITO antennas did not give any reasonable/clear frequency response. Further design optimization are still under investigation to obtain even better performances from antennas made of ITO. The results here shown can be easily extended to all the conductive oxides that are

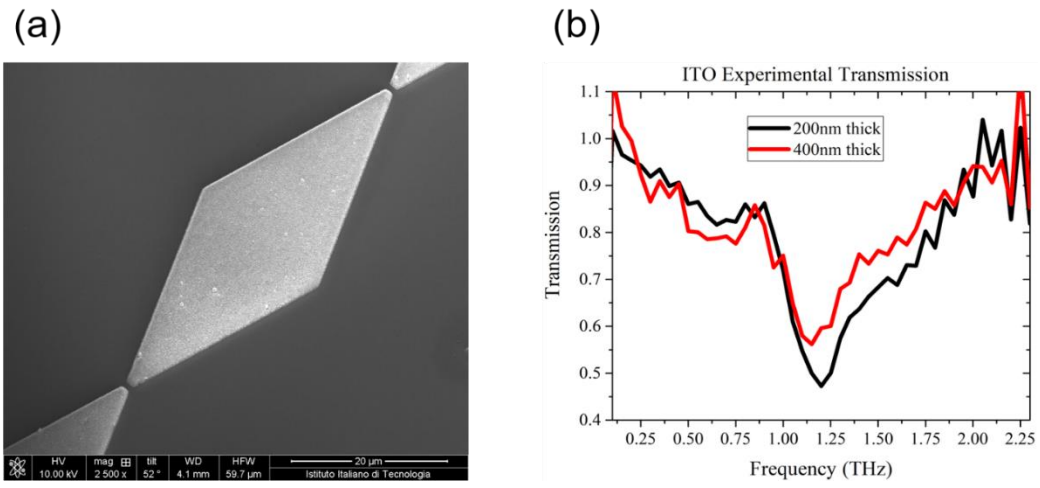

Figure 4.7 (a) ITO shuttle antenna in a SEM image. The gap dimension between the antennas is $1 \times 1\ \mu m^2$. (b) THz transmission spectra of the 200 nm (black solid line) and $400\ nm$ (red solid line) thick ITO shuttle antennas. A clear resonance occurs between 1 and 1.25 THz for both samples.

potentially good candidates as alternative materials for non-linear experiments.

5 Moon-Shaped Tapered Antenna for Improved Strong-Coupling Experiments

Condensed matter nanosystems, such as quantum dots and nano-crystals, can change their spontaneous emission rate when the electromagnetic properties of their surrounding environment are accurately engineered. This is possible by using resonant cavities, such as NAs placed closed to the nano-crystals [65], [73], where the system formed by the nano-crystals and NAs can give rise to a weak or strong interaction when the resonance frequencies of these two elements are properly matched. In particular, during the interaction an exchange of energy takes place between NAs and nano-crystals. If the exchange rate is too low to overcome the energy loss, the system is said to be in the *weak coupling regime*. Differently, when the energy exchange rate is high enough to equal or overcome the loss, the system enter the so called *strong coupling regime*. One of the currently studied strongly coupled systems involves the light-matter interaction inside resonant cavities [74]–[76] especially applied to nano-sized materials [74], [77], [78]. In this scenario, when the system enters the strongly coupled regime a hybridization of the cavity mode and the matter-related mode (e.g., exciton and phonon resonances) of the nano-sized materials under study is induced [31], [65], [74]–[78]. Recently, X. Jin and coworkers [32] used chains of gold end-to-end coupled straight NAs, resonating in the THz range, to study the hybridization state between NA plasmonic mode and the phonon mode of cadmium sulphide (CdS) nano-crystals, by exploiting the high field enhancement value reached in the nanocavity formed by the gap between NAs. So far in this thesis, the possibility to improve the NAs through a judicious modification of their shapes has been presented. Such study can be readily applied to develop new optimized NA designs for improving light-matter interaction for sensing of ultra-low concentrations of materials (e.g. 2D materials detection) and for the study of the modified physico-chemical properties of matter induced by the formation of new hybrid states (e.g. the modification of phonon-mediated energy dissipation in nano-systems).

5.1 Light-matter interaction: basic concepts

As already stated, strong light-matter coupling occurs if proper conditions regarding the exchange of energy between the two systems are met [74]–[76], [79]. In general, a coupled and damped two-oscillators system can be described by

$$\begin{aligned} \ddot{x}_1 + \gamma_1 \dot{x}_1 + \omega_1^2 x_1 + s^2 x_2 &= 0 \\ \ddot{x}_2 + \gamma_2 \dot{x}_2 + \omega_2^2 x_2 + s^2 x_1 &= 0, \end{aligned} \tag{5.1}$$

with s coupling factor between the two oscillators, γ_1 and γ_2 damping factors, and x_1 and x_2 the displacements. When an external driving force is applied to this coupled system the Eq. (5.1) can be rewritten as

$$\begin{cases} \ddot{x}_1 + \gamma_1 \dot{x}_1 + \omega_1^2 x_1 + s^2 x_2 = f \\ \ddot{x}_2 + \gamma_2 \dot{x}_2 + \omega_2^2 x_2 + s^2 x_1 = 0. \end{cases} \tag{5.2}$$

Thus, by externally exciting the system to enter a coupled state, the results of the interaction is the formation of two new hybrid resonance frequencies ω_+ and ω_-:

$$\omega_\pm = \omega_1 + \omega_2 - \frac{i(\gamma_1 + \gamma_2)}{4} \pm \sqrt{s_{\text{eff}}^2 - \frac{(\gamma_1 - \gamma_2)^2}{16}} \tag{5.3}$$

with $s_{\text{eff}} = \frac{s^2}{2\,\bar{\omega}}$, with $\bar{\omega} = (\omega_1 - \omega_2)/2$, the effective coupling constant [80]. The distance in frequency between these two new hybrid modes is called Rabi Splitting and, in the simplified scenario described above, is defined as

$$\Omega_R = (\omega_+ - \omega_-) = 2\sqrt{s_{\text{eff}}^2 - \frac{(\gamma_1 - \gamma_2)^2}{16}}. \tag{5.4}$$

The Rabi splitting Ω_R can be seen as the measure of the coupling strength between oscillators. Practically speaking, a system is said to be strongly coupled if the Rabi splitting can be experimentally observed [74]. As a rule of thumb, the onset of the strong coupling is sometimes positioned at

$$\Omega_R > \frac{\gamma_1}{2} + \frac{\gamma_2}{2}. \tag{5.5}$$

5.2 THz Nano-Cavities for Strongly Coupled Plasmon-Phonon Systems

As already said, THz nano-cavities have been successfully employed by X. Jin *et al.* [32] in the attempt to reach the strong coupling regime to obtain the formation of new hybridized phonon modes in CdS nanocrystals. The NAs have been designed to have variable length, an antenna width of $200\,\text{nm}$, gap width of $30\,\text{nm}$, and with a $8.5\,\mu\text{m}$ wide chain spacing, to form a $200 \times 200\,\mu\text{m}^2$ NAs matrix. The simulated transmission spectra, as reported in Ref. [32], are shown in **Figure 5.1 (a)**. If the sample is covered by two layers of CdS nanocrystals with optically-active phonon mode (Fröhlich resonance - FR) at around $8\,\text{THz}$, the simulated transmission spectra, reported in **Figure 5.1 (b)**, are modified and reveal the presence of two peaks resulting from the hybridization of the plasmonic NA resonance and the phonon nanocrystal mode. After the numerical calculations, several samples have been fabricated

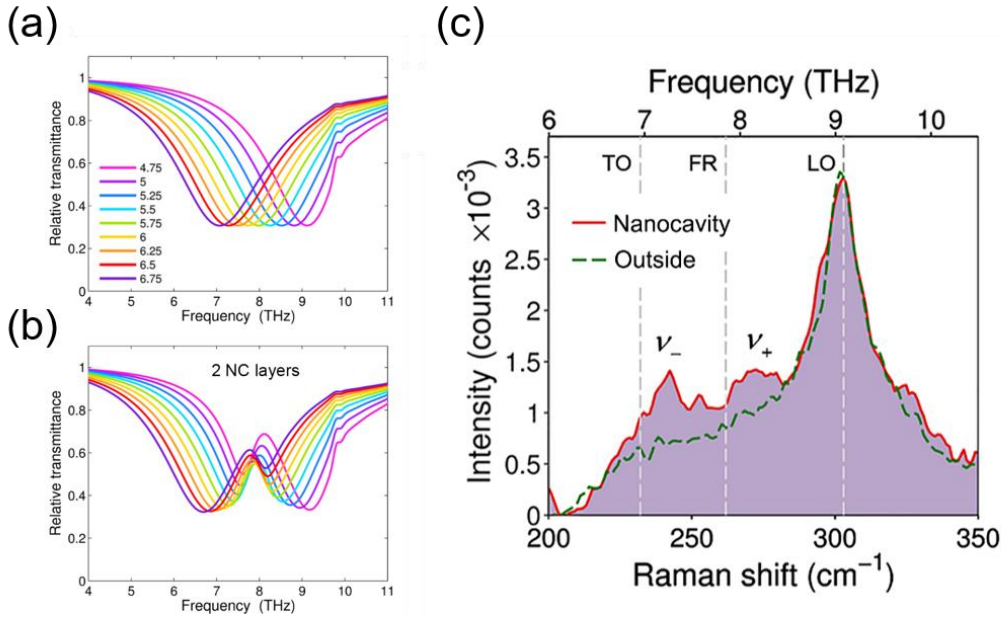

Figure 5.1 (a) Simulated transmission spectra of bare gold antenna chains with antenna length L varying from $4.75\ \mu m$ to $6.75\ \mu m$. (b) Simulated transmission spectra of gold antenna chains covered with 2 nano-crystals CdS layers varying the antenna length L from $4.75\ \mu m$ to $6.75\ \mu m$. (c) Experimental Raman spectrum inside (red solid line) and outside (green dashed line) the nanocavity between gold antennas covered with one layer of CdS nano-crystals and antenna length equal to $5.75\ \mu m$. The figure was adapted from [32] licensed under the Creative Commons Attribution 4.0 International License.

and characterized by means of transmission THz spectroscopy (not reported), experimentally confirming the hybridized states presence.

Raman spectroscopy is an optical characterization technique where inelastic scattering is evaluated to retrieve information on the phonon response of the material under study. It is a useful alternative characterization technique which does not employ THz radiation to reveal the hybrid states from in the cavity. The Raman spectra have been collected with a close-to-diffraction limit probe size and excitation wavelength at $\lambda = 632.8\ \mathrm{nm}$, on the NA samples covered with CdS nano-crystals. The result is shown in **Figure 5.1 (c)**. The green dashed line represents the Raman spectrum outside the cavity, while the red solid line is the Raman characterization performed inside the nanocavity. It has to be noted that the excitation wavelength is too small to excite the NAs as they resonate at THz frequency. Nonetheless, the Raman spectrum recorded while illuminating the gap between NAs shows the two hybridized modes ν^+ and ν^- (or ω^+ and ω^- following our notation) due to the strong coupling between the plasmonic mode and the phonon mode of CdS nano-crystals at around $8\ \mathrm{THz}$ ($\sim 260\ \mathrm{cm}^{-1}$), meaning that the coupling is achieved without any external THz excitation. Such hybridization state, also visible in “dark conditions”, is made possible thanks to the small mode volume reached in the gap between coupled NAs. In fact, as already shown in Section (2.5.1), small mode volumes result in a very high THz vacuum field, which

in this case couples to the Frohlich phonon mode of the nano-crystals [81], [82], leading to the splitting of the specific phonon resonance, as clearly visible in the Raman spectrum.

5.3 Moon-shaped Nanoantenna

The experimental confirmation of the tapering strategy effectiveness gives us the opportunity to improve the performance of the devices applied to phonon strong coupling experiments (as the one presented in the last section). Indeed, in order to further increase the coupling strength in such nanocavity system, the mode volume reached inside the antenna gap has to be reduced. In this scenario, the tapering strategy is the perfect tool to achieve this goal. However, instead of using pairs of coupled bow-tie gold NAs, another antenna geometry has been chosen for this purpose: the moon-shaped antenna, shown in the sketch of **Figure 5.2**. The shape is the result of the study on two antenna designs, that is, the split-ring (top right of **Figure 5.2**) and the shuttle antenna (bottom right of **Figure 5.2**). On one hand, the split-ring shape offers low radiative loss [83]–[85] while presents high non-radiative loss when designed with small lateral cross sections (as required in our case to obtain a nano-sized cavity). On the other hand, the shuttle layout guarantees low non-radiative loss, thanks to tapering, yet presents high radiative loss due to its dipole-like structure. By merging these two configurations, the obtained moon-antenna (i.e., a tapered split-ring resonator) is characterized by low ohmic (non-radiative) and scattering (radiative) loss. In practical terms, the tapering strategy is here applied by varying the parameter $W2$ (see **Figure 5.2**) that corresponds to the outer end of the tapered bow-tie, in turn related to the tapering angle.

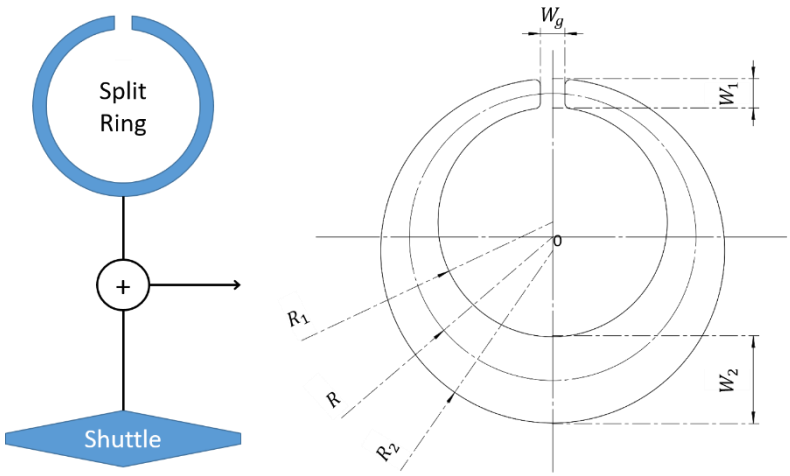

Figure 5.2 Scheme of moon-shaped NAs (left) for vibrational strong coupling obtained as the mix of the split ring antenna (top right) and the shuttle antenna (bottom right). The parameter W_g is the gap width, W_1 the gap height, W_2 the larger width of the moon, R, R_1 and R_2 are the radius of the central, internal and external circumferences, respectively.

5.3.1 Moon-shaped NA Design and Simulations

Simulations have been conducted by X. Jin at INRS-EMT using COMSOL. The NAs made of gold have been designed to be $100\,\mathrm{nm}$ in thickness, with a periodicity $g_x = g_y = 9\,\mu\mathrm{m}$ in order to move the lattice resonance far from the NAs resonance frequency and thus avoid the influence of the latter in the study of the NA characteristics. The moon-shaped antenna is sketched in **Figure 5.2** along with the most relevant design parameters. In particular, the NA features at the gap are fixed at $W_g = 20\,\mathrm{nm}$ and $W_1 = 200\,\mathrm{nm}$. The length of the NA L is defined as the length of the circumference of the central circle with center at the point $O(0,0)$ and radius R, thus $L = 2\pi R$. The radii of the inner and outer circles are $R_1 = R - \frac{W_1}{2} - \frac{h}{2}$, $R_2 = R + \frac{W_1}{2} + \frac{h}{2}$, where $h = (W_2 - W_1)/2$ with center $O_1 = h/2$ and $O_2 = -h/2$, respectively. Moreover, the quantity $f_\mathrm{m} = W_2/W_1$ has been defined as "moon factor" and quantifies the tapering. Thus, by judiciously varying the moon factor f_m and the antenna length L it is possible to optimize the NA response. In particular, it has been found, by performing simulation at a fixed antenna length $L = 8\,\mu\mathrm{m}$, that the optimal value for the moon factor is $f_\mathrm{m} = 6$ at the resonance frequency of $7.8\,\mathrm{THz}$, that is close to the FR mode frequency of the CdS nanocrystals. Furthermore, the FWHM of such antennas for $f_\mathrm{m} = 6$ is around $0.5\,\mathrm{THz}$,

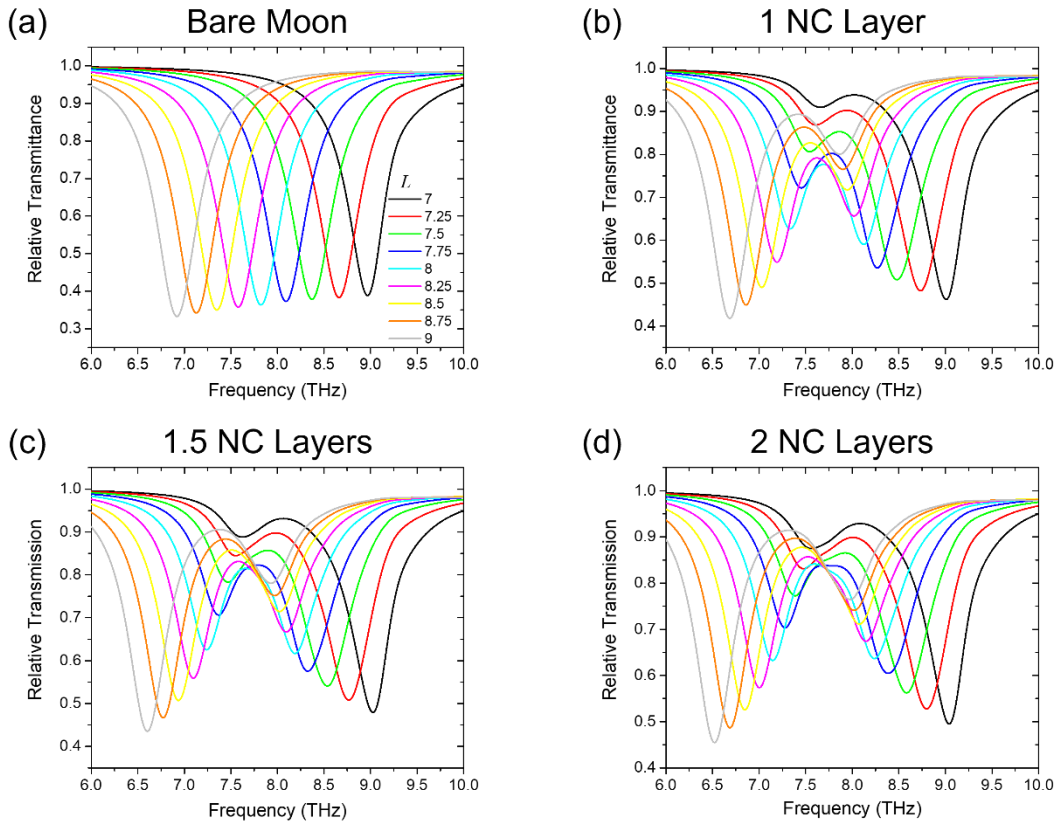

Figure 5.3 (a) Simulated transmission spectra of bare gold moon NAs with antenna length L varying between 7 μm to 9 μm. (b) Simulated transmission spectra of moon NAs covered with 1 (c) 1.5 and (d) 2 CdS nano-crystal layers varying the antenna length L between 7 μm to 9 μm.

that is, ~1/5 of the FWHM presented by the dipolar antennas used in Ref. [32] (~2.3 THz) as it can be seen in **Figure 5.3 (a)**. Finally, also the mode volume for the optimized moon-shaped NA results higher. In fact, in the case of NA length $L = 8\,\mu\text{m}$ and resonance frequency around $f_{\text{res}} = 7.8\,\text{THz}$, the mode volume equals $2.16 \times 10^5\,\text{nm}^3$, thus becoming even smaller than geometrical volume of the gap ($4 \times 10^5\,\text{nm}^3$), which directly shows the significant performance improvement of this kind of antennas [86]. As a consequence, the simulations conducted on arrays of moon NAs covered with nano-crystal layers show a more pronounced splitting of the two hybridized modes with respect to the already studied dipolar NA chains, as it can be seen from **Figure 5.3** for **(b)** 1, **(c)** 1.5, and **(d)** 2 NC layers, by varying the antenna length L from 7 to $9\,\mu\text{m}$.

5.3.2 Moon-Shaped NAs Fabrication and Characterization

Moon-shaped antennas have then been fabricated and spin-coated with CdS nano-crystals, $10\,\text{nm}$ in diameter, by following the fabrication technique shown in Section (4.1) of this Thesis. The moon-shaped NAs have been fabricated over large areas ($225 \times 225\,\mu\text{m}^2$) to allow retrieving a measurable transmission signal during the far-field THz characterizations. **Figure 5.4 (a)** illustrates a dark-field optical microscope image of an array of moon-shaped NAs on a silicon substrate. In **Figure 5.4 (b)** is shown a magnified view of the moon apical gap, characterized by a width between 10 and 20 nm. Moreover, **Figure 5.4 (c)** and **(d)**

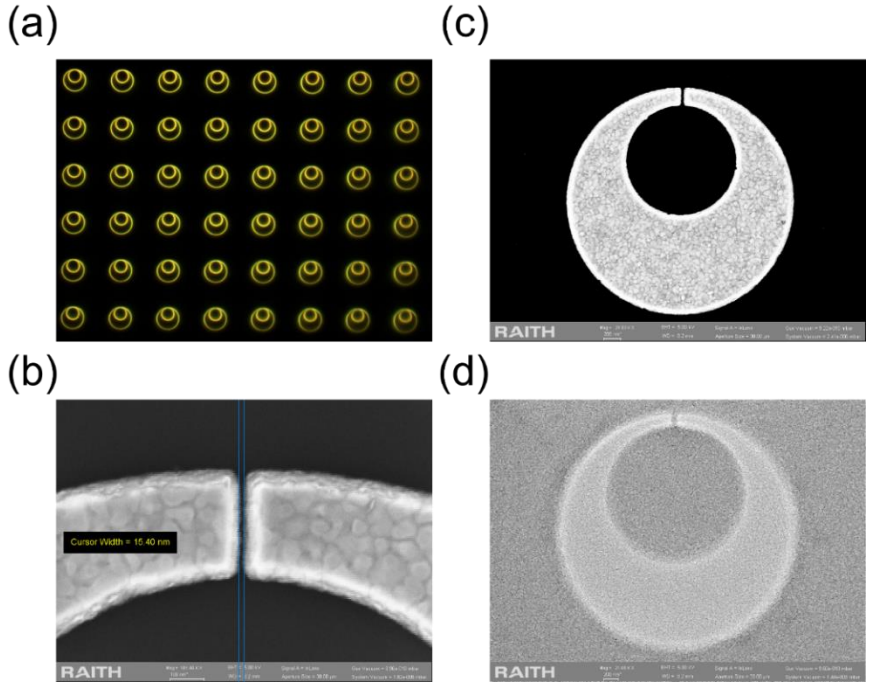

Figure 5.4 (a) Optical microscope image in dark field mode of an array of moon-shaped NAs fabricated on a silicon substrate. (b) SEM image of the gap in a moon-shaped NA. The obtained gap width varies between 10 and 20 nm. (c) SEM images before and (d) after the nano-crystal layers deposition.

report SEM images of the moon-shaped NAs with and without the nano-crystal layer, respectively.

First, silicon substrates spin-coated with CdS nano-crystals have been characterized in the SISSI-mat beamline of the "Elettra Sincrotrone Trieste" light source (Italy), to determine the FR resonance frequency. The experimental spectra obtained illuminating a single mono-layer of CdS nano-crystals have been analyzed and modeled by using COMSOL software. By fitting the experimental curves, the filling factor f (a dimensionless quantity representing the filling ratio of the mixture) has been found to be 0.81, with a FR optical phonon frequency at $7.73\ \mathrm{THz}$ and linewidth $0.45\ \mathrm{THz}$. Then, the transmission spectra of the bare arrays and of arrays covered with 1, 1.5 and 2 CdS nano-crystals layers have been characterized again at the SISSI-mat beam line. The results are shown in **Figure 5.5** and are in good agreement with the simulated results reported in **Figure 5.3**. In general, the simulated results present deeper transmission minima than the measured spectra, mainly due to the fact that the THz spot size on the sample was slightly larger than the array size in our experiments. Yet, both the frequency position of the hybridized resonances and their separation in the experimental curves closely resemble those obtained during the simulations.

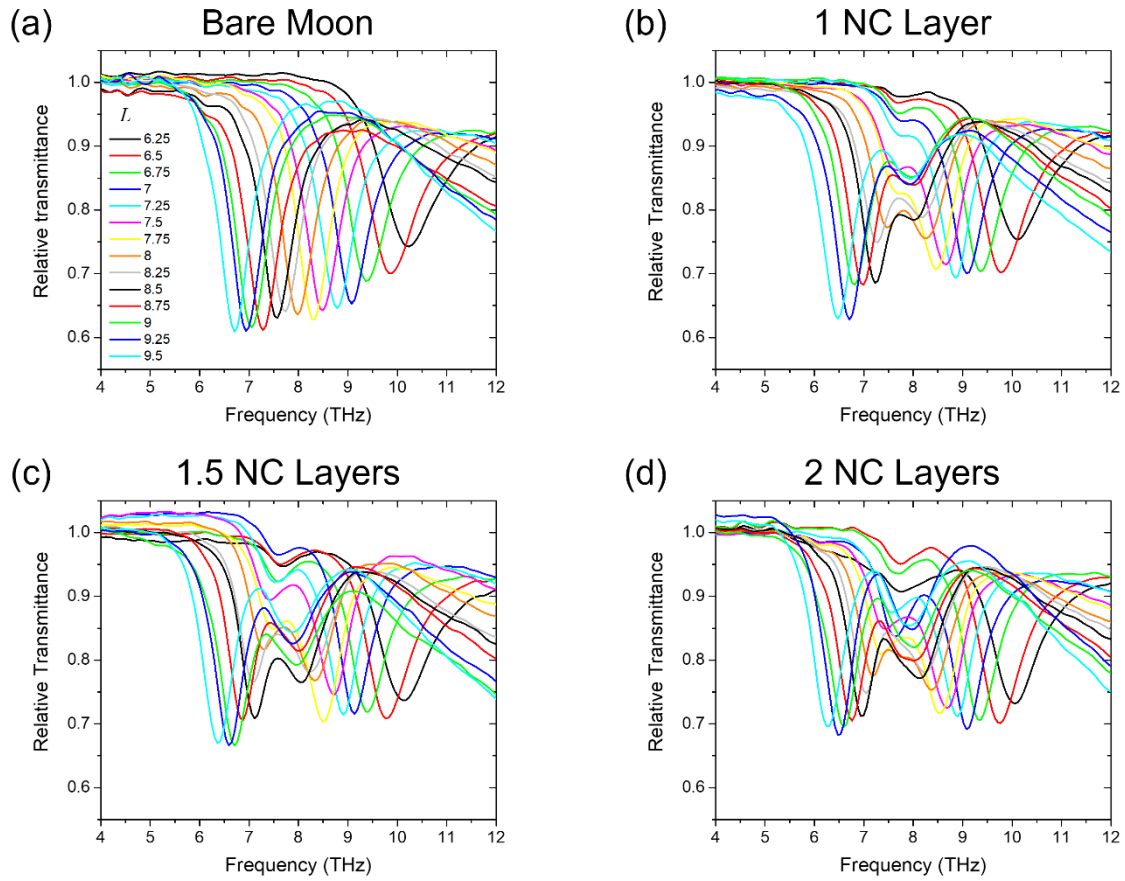

Figure 5.5 Experimental transmission spectra obtained from (a) bare, (b) 1, (c) 1.5 and (d) 2 NC layers covered moon-shaped NAs samples. The moon-shaped NAs length varies from $6.25\ \mu m$ to $9.25 \mu m$.

From the experimental results, it can be noticed that the Rabi splitting increases as more mono-layers of CdS nano-crystals are deposited over the moon-shaped NAs. In particular, as can be seen from **Table 1**, such splitting results to be larger than the corresponding case of the dipolar NAs of Ref. [32] with the same number of deposited monolayer, although the gap area is smaller in the fabricated moon-shaped NAs (2/3 of the gap area of the dipolar antennas of Ref. [32]), and consequently a smaller number of NCs are present in the gap. These evidences confirms the usefulness of this kind of devices (implementing the tapering strategy) also in applications involving strong THz light - matter coupling.

As already shown above, Raman spectroscopy can been used as a complementary tool, along with far-field THz characterization, for the study of the phonon response of nano-crystals in nanocavities [32]. Thus, thanks to this alternative spectroscopy method, it has been possible to study and demonstrate that the nano-crystals phonon response is intrinsically modified when they are placed inside a nano-cavity characterized by an extremely small mode volume. Such important result is of great interest as it shows a way (via the engineering of the electromagnetic environment) to modify the vibrational spectrum of a material without directly intervening on its chemical composition or physical structure. We were thus also interested in evaluating the NC Raman response for the moon-shaped antenna substrate, since such structures present an even smaller mode volume and greater field enhancement with respect to dipolar antenna.

	1 Layer (# NCs)	1.5 Layer (# NCs)	2 Layer (# NCs)
Moon Antenna	0.91 (40)	1.15 (60)	1.22 (80)
End to End Antenna	0.8 (60)	0.98 (90)	1.13 (120)

Table 1 Comparison of moon antenna (with $L = 8\ \mu m$) and end to end antenna (with $L = 5.75\ \mu m$) Rabi splitting values (the estimated number of NCs inside the antenna gaps are in parenthesis) varying the number of deposited layers. The moon antenna presents larger Rabi splitting for the same number of NCs layers, even in the presence of less NCs in the active area, due to the smaller gap when compared to the end to end antennas of Ref. [32].

The characterization has been conducted in a backscattering configuration by using a He:Ne laser with wavelength $\lambda = 632.8\ \mathrm{nm}$, which was chosen to minimize the fluorescence from CdS nano-crystals (bandgap of $2.4\ \mathrm{eV}$) as well as scattering. The system used for the characterizations is a Raman Renishaw inVia, that allows for micro-Raman illumination by using a 150× LEICA PL APO objective, with numerical aperture that equals 0.95. The Raman spectrum of a 2 layers covered moon-shaped antenna with $L = 8\ \mu\mathrm{m}$ is presented in **Figure 5.6**. As for the end to end antennas, also the Raman spectrum recorded here reveals the modification of the phonon response of the CdS nano-crystals, with evidence of a clear formation of two hybridized bands, marked as ω^+ and ω^- in figure. Moreover, in the case of

moon-shaped NAs, the response appears to be more pronounced when compared to the Raman spectrum of **Figure 5.1 (c),** related to the end-to-end coupled dipolar antennas. Although further studies and experiments will be conducted on the moon antennas, the results obtained so far confirm the superior performance of moon antennas, which promises to open new perspectives in strong coupling experiments involving THz radiation.

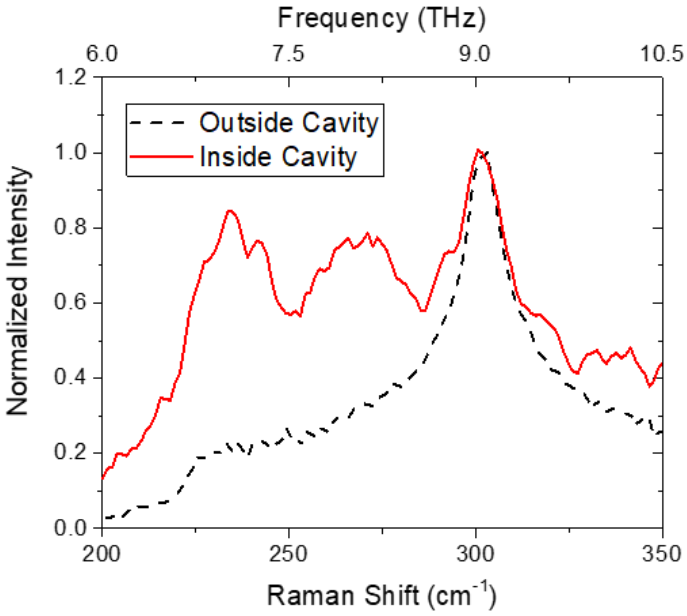

Figure 5.6 Raman spectrum inside (red solid line) and outside (black dashed line) the cavity of moon-shaped antennas with $L = 8\ \mu m$, covered with 2 layers of CdS nanocrystals.

6 Conclusion and Perspectives

The THz frequency range has been widely explored because of its promising applications in many research and industrial fields. The so called “THz-gap” is still currently in the bridging process, but very important steps have been taken to completely fill it. The first important boost came from the improvement and the optimization of sources and detectors that nowadays allows for affordable, stable and precise THz generation and detection. Thus, the interest on the use of THz waves has been further spread, and fast communication technology, non-destructive sensing and imaging, as well as industrial process control are only few examples of applications where THz technology can be potentially involved.

Spectroscopy is one of the most interesting fields of application mainly because many elementary excitations of matter lie in this frequency range. In the past, scientists had to deal with the intrinsic low sensitivity characteristic of THz waves in sensing nanoscale objects, due to the associated long-wavelength. For this reason, THz spectroscopy was initially limited to the study of bulk materials or big aggregates of nano-particles; however, THz sensitivity has been improved over the years. In the last decades, a particular physical effect has been employed to improve common spectroscopic techniques (e.g. Raman and infrared absorption) that is, the surface enhancement effect. Thanks to the use of corrugated surfaces and nano-structures, it is possible to capture and localize free-propagating light in sub-wavelength volumes, thus obtaining highly concentrated fields. By exploiting such advances, our group has demonstrated the applicability of the surface enhancement concept to THz spectroscopy, by using THz NAs. Thanks to field enhancement, it is possible to retrieve spectroscopic information of nano-matter in close proximity to the NA extremities (where the electric field is localized) as a result of the improved absorption coefficient of nano-sized material interacting with the THz localized field. Such findings have huge implication in the use of THz waves not only for spectroscopy but also, for instance, in THz strong coupling experiments. Indeed, recently, vibrational transitions of molecules placed in infrared microcavities were shown to strongly couple to the vacuum electric field [87], [88], and, as a consequence of this coupling, the structural and chemical properties of the molecules were shown to be significantly modified [89]–[91]. X. Jin *et al.*, by placing nano-particles inside a THz nanocavity, entered the phonon strong coupling regime exploiting the very high vacuum electric field that can be achieved inside the nanocavity. Phonons are the quanta of lattice vibrations and represent one of the main channel of energy dissipation in solid-state systems [92]–[95]. The phonon response is usually identified as an inherent feature of a specific material and typically limits the functionalities of devices for light emission and charge transport. Thus, with their work, X. Jin and coauthors not only

demonstrated the possibility to reach the strong coupling regime at THz frequency but also showed a path to modify the phonon response of materials in a completely novel fashion: by engineering the electromagnetic environment where the material operates, and thus creating a new hybrid entity with mixed light - matter properties.

Such envisioned advances need a continuous and deeper study to obtain better NA performances. In particular, material as well as radiative loss deeply affects the NA properties limiting the potentiality of NA-assisted THz light-matter interaction studies. Thus, I focused my work on the study, simulation, design and fabrication of plasmonic THz NAs towards the achievement of improved performance, in terms of near field enhancement and mode volume reduction. First, a simplified quasi-analytical model has been developed showing that the field localization properties of a cylindrically shaped gold NA can be effectively improved if the NA is optimally tapered. In fact, by increasing the tapering angle an initial improvement is obtained until a maximum value is reached. On the contrary, too large angles result in a decrease of the NA performance. Such improvement is related to the trade-off between a lower non-radiative loss and a higher radiative loss associated to the increase in the tapering angle. This behavior has been reproduced by an extensive FEM simulation investigation, to retrieve quantitative information for an accurate antenna design regarding gold planar end-to-end coupled bow-ties. In particular, a ~2.2 times higher near field enhancement and a 7-fold reduced mode volume inside the gap has been found when coupled bow-tie NAs are optimally tapered, in comparison with straight dipolar antennas presenting an over-damped response. Then, five samples have been fabricated with tapering angles of 0, 0.2, 0.5, 2.5 and 5° in order to experimentally study the tapered NAs response. Once fabricated, the samples have been characterized by employing a THz-TDS setup. The FWHM has been calculated from the transmission spectra, in order to retrieve information on the total NA loss as the tapering angle is varied. The FWHM of the experimental characterization decreases as the tapering angle increases, finally confirming the improvement of the NAs performance anticipated by both the quasi-analytical model and FEM simulations.

These findings open up, for example, a new route for the development of novel plasmonic nanostructures for nonlinear plasmonics. In particular, ITO is a potentially employable material for THz nonlinear plasmonic experiments, where high power sources are used, thanks to its better endurance to high power densities with respect to gold, due to the higher melting point and thermo-mechanical strength. However, ITO, as many other materials, have been avoided in the design of plasmonic antennas principally because of the high ohmic loss that hampers its use. In order to overcome such limitation, it was studied the applicability of the tapering strategy in order to reduce the loss of antennas made of ITO. In this thesis, ITO

shuttle antennas have been optimized to resonate in the THz frequency range by using the tapering angle variation technique. As a result, the ITO antennas presented a clear resonance in the THz frequency range, finally giving the possibility to conduct more comprehensive nonlinear THz studies exploiting the filed enhancement properties of resonant plasmonic structures.

Furthermore, the ability to tailor the intrinsic phonon response of nanosystems has been presented above as a crucial outcome of our NA-assisted THz strong coupling experiments. In order to fully exploit this possibility, it is of utmost importance to reach extremely high cavity vacuum electric field in the NAs employed. The tapering strategy, with its ability to greatly reduce the mode volume, has been shown to be an effective tool for the design of novel optimized nanoplasmonic resonators for the strong coupling regime. In particular, a new antenna design for strong coupling experiments, called *moon-antenna*, have been developed and designed to reduce the mode volume to extremely small values, below the geometrical volume of the antenna gap, and to increase the THz near field enhancement. The fabricated structures, characterized via THz far field spectroscopy and Raman spectroscopy, revealed a promising improvement in the platform performance and are still under study.

Future works will thus take advantage of these new designs to target improvements in nanodevice performance. On one hand, we have shown the possibility to make accessible the use of alternative materials for nonlinear plasmonics experiments [96]–[98] by reducing the antenna ohmic loss. On the other hand, the design and realization of novel photonic nano-architectures can be employed for the selective manipulation of the optical phonon response of reduced-dimensionality materials, such as not only the already investigated nano-crystals but also 2D-materials [99]–[102]. This could have beneficial effects in various fields of application, such as THz sensing and communications, as well as nano- and opto-electronics. For instance, a proper engineering of the phonon response of selected nanomaterials can induce phonons to decay coherently [103]–[105] through the emission of THz radiation, instead of losing their energy non-radiatively, as commonly occurs. In addition, phonon hybridization could also be exploited to alter the electron-phonon interaction mechanism in nano-systems, promising to significantly modify light emission/charge transport in nano-devices [106]–[109].

7 Other Projects

7.1 Project with Università degli Studi di Palermo

Beside the main project on the design, optimization and realization of THz NAs, another project has been conducted related to the research pursued at Università degli Studi di Palermo. This project consisted in the study and data analysis of the electrical response of previously fabricated memristors. Memristors are three-terminal devices (metal/insulator/metal) whose resistance changes depending on the applied electric current and/or voltage at its contacts. The devices fabricated are constituted by an anodized titanium dioxide layer (insulator) sandwiched between titanium and copper contacts (metals). First, the devices have been characterized and studied [110]. Moreover, it has been found a singular behavior when the device is stressed with high and constant values of electric current, that is the possibility to set several discrete levels of resistance, thus potentially obtaining a multilevel memory element [111].

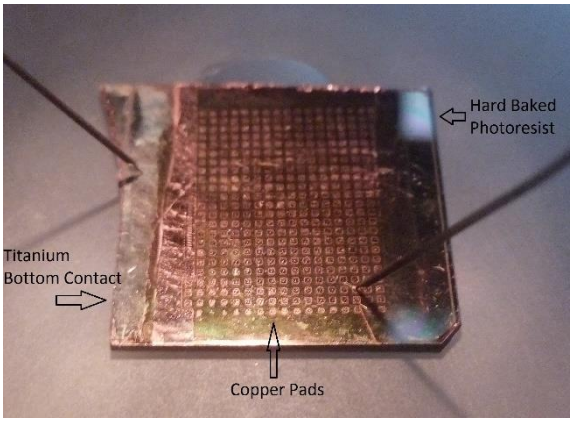

7.2 Additional Projects

During my Ph.D. so far, I also dedicated my micro- and nano-fabrication experience to prepare samples related to the research projects of my group at INRS, IIT and UniPa. In the following are shown two of them.

- Design and Fabrication of Terahertz Bragg Gratings on a Two-Wire Waveguide [112]. THz communication technology is a relatively new field of study thanks to unassigned bandwidths and higher transmission rate with respect of the nowadays available frequency ranges used in telecommunication. THz waveguides are key for the development of such new communication platform. In recent years, many THz waveguide prototypes have been proposed, nonetheless they typically suffer from

high losses. Two-wire waveguides (TWWGs) promise low loss and dispersion-free propagation, along with the capacity to allow the propagation of TEM modes, which means better coupling property with the THz radiation. In this work, a TWWGs (operating at $0.6\,\mathrm{THz}$) formed by two copper wires coated with properly engraved Kapton (to obtain the desired effective refractive index profile) has been simulated, designed and fabricated to efficiently couple and guide THz radiation.

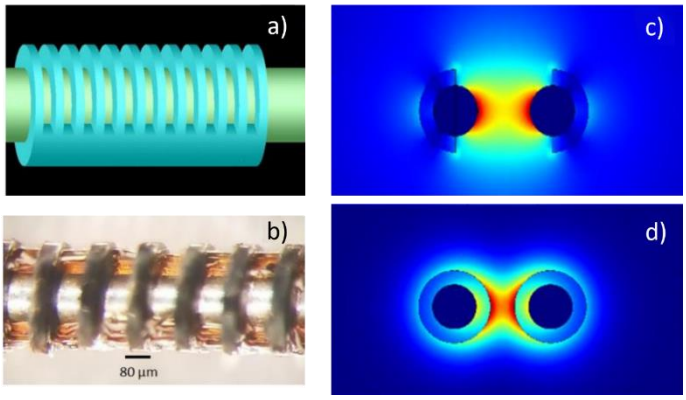

- Highly sensitive polarization rotation measurement through a high-order vector beam generated by a metasurface [113]. In this work, a judiciously designed metasurface, thanks to the generation of a vector beam with an azimuthally-dependent polarization distribution, allows for a very precise (sensitivity of 10^{-2} degrees) determination of the polarization rotation angle of incoming light with a dynamic range of 180°. While typical polarization rotation measurement setups consist of a complex assembly of instruments and devices, here the same result is achieved with a simplified platform. Such platform can also be used for the determination of the correlation between the time evolution of the high order Pancharatnam-Berry phase and the rotational Doppler frequency shift of light [114].

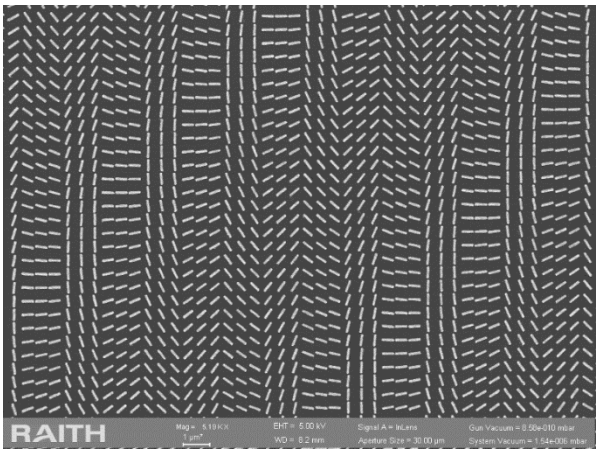

Bibliography

[1] Y.-S. Lee, *Principles of terahertz science and technology*. New York, NY: Springer, 2009.

[2] S. L. Dexheimer, *Terahertz Spectroscopy: Principles and Applications*. CRC Press, 2007.

[3] T. Kleine-Ostmann and T. Nagatsuma, “A Review on Terahertz Communications Research,” *J. Infrared Millim. Terahertz Waves*, vol. 32, no. 2, pp. 143–171, Feb. 2011, doi: 10.1007/s10762-010-9758-1.

[4] D. Zimdars and J. S. White, “Terahertz reflection imaging for package and personnel inspection,” in *Terahertz for Military and Security Applications II*, Sep. 2004, vol. 5411, pp. 78–84, doi: 10.1117/12.562216.

[5] J. F. Federici *et al.*, “THz imaging and sensing for security applications—explosives, weapons and drugs,” *Semicond. Sci. Technol.*, vol. 20, no. 7, p. S266, 2005, doi: 10.1088/0268-1242/20/7/018.

[6] C. Jansen *et al.*, “Terahertz imaging: applications and perspectives,” *Appl. Opt.*, vol. 49, no. 19, p. E48, Jul. 2010, doi: 10.1364/AO.49.000E48.

[7] H. Harde, S. Keiding, and D. Grischkowsky, “THz commensurate echoes: Periodic rephasing of molecular transitions in free-induction decay,” *Phys. Rev. Lett.*, vol. 66, no. 14, pp. 1834–1837, Apr. 1991, doi: 10.1103/PhysRevLett.66.1834.

[8] T. R. Globus *et al.*, “THz-Spectroscopy of Biological Molecules,” *Spectrosc. Biol. Mol.*, p. 12.

[9] M. Schall, M. Walther, and P. Uhd Jepsen, “Fundamental and second-order phonon processes in CdTe and ZnTe,” *Phys. Rev. B*, vol. 64, no. 9, Aug. 2001, doi: 10.1103/PhysRevB.64.094301.

[10] S. G. Carter, “Quantum Coherence in an Optical Modulator,” *Science*, vol. 310, no. 5748, pp. 651–653, Oct. 2005, doi: 10.1126/science.1116195.

[11] K. B. Nordstrom *et al.*, “Excitonic Dynamical Franz-Keldysh Effect,” *Phys. Rev. Lett.*, vol. 81, no. 2, pp. 457–460, Jul. 1998, doi: 10.1103/PhysRevLett.81.457.

[12] S. J. Park *et al.*, “Detection of microorganisms using terahertz metamaterials,” *Sci. Rep.*, vol. 4, p. 4988, May 2014, doi: 10.1038/srep04988.

[13] R. Piccoli, A. Rovere, A. Toma, R. Morandotti, and L. Razzari, “Terahertz Nanoantennas for Enhanced Spectroscopy,” in *Terahertz Spectroscopy - A Cutting Edge Technology*, J. Uddin, Ed. InTech, 2017.

[14] G. Gallot, S. P. Jamison, R. W. McGowan, and D. Grischkowsky, “Terahertz waveguides,” *JOSA B*, vol. 17, no. 5, pp. 851–863, May 2000, doi: 10.1364/JOSAB.17.000851.

[15] N. Laman, S. S. Harsha, and D. Grischkowsky, “Narrow-Line Waveguide Terahertz Time-Domain Spectroscopy of Aspirin and Aspirin Precursors,” *Appl. Spectrosc.*, vol. 62, no. 3, pp. 319–326, Mar. 2008, doi: 10.1366/000370208783759768.

[16] J. S. Melinger, N. Laman, and D. Grischkowsky, “The underlying terahertz vibrational spectrum of explosives solids,” *Appl. Phys. Lett.*, vol. 93, no. 1, p. 011102, Jul. 2008, doi: 10.1063/1.2949068.

[17] F. D’Apuzzo *et al.*, “Resonating Terahertz Response of Periodic Arrays of Subwavelength Apertures,” *Plasmonics*, vol. 10, no. 1, pp. 45–50, Feb. 2015, doi: 10.1007/s11468-014-9775-3.

[18] M. A. Seo *et al.*, “Terahertz field enhancement by a metallic nano slit operating beyond the skin-depth limit,” *Nat. Photonics*, vol. 3, no. 3, pp. 152–156, Mar. 2009, doi: 10.1038/nphoton.2009.22.

[19] H.-R. Park, K. J. Ahn, S. Han, Y.-M. Bahk, N. Park, and D.-S. Kim, “Colossal Absorption of Molecules Inside Single Terahertz Nanoantennas,” *Nano Lett.*, vol. 13, no. 4, pp. 1782–1786, Apr. 2013, doi: 10.1021/nl400374z.

[20] D.-K. Lee *et al.*, “Highly sensitive and selective sugar detection by terahertz nano-antennas,” *Sci. Rep.*, vol. 5, p. 15459, Oct. 2015, doi: 10.1038/srep15459.

[21] J. B. Khurgin and G. Sun, “Plasmonic enhancement of the third order nonlinear optical phenomena: Figures of merit,” *Opt. Express*, vol. 21, no. 22, pp. 27460–27480, Nov. 2013, doi: 10.1364/OE.21.027460.

[22] M. Fleischmann, P. J. Hendra, and A. J. McQuillan, “Raman spectra of pyridine adsorbed at a silver electrode,” *Chem. Phys. Lett.*, vol. 26, no. 2, pp. 163–166, May 1974, doi: 10.1016/0009-2614(74)85388-1.

[23] K. Kneipp, M. Moskovits, and H. Kneipp, Eds., *Surface-Enhanced Raman Scattering: Physics and Applications*. Berlin Heidelberg: Springer-Verlag, 2006.

[24] M. Chirumamilla *et al.*, “3D Nanostar Dimers with a Sub-10-nm Gap for Single-/Few-Molecule Surface-Enhanced Raman Scattering,” *Adv. Mater.*, vol. 26, no. 15, pp. 2353–2358, doi: 10.1002/adma.201304553.

[25] K. Kneipp *et al.*, “Single Molecule Detection Using Surface-Enhanced Raman Scattering (SERS),” *Phys. Rev. Lett.*, vol. 78, no. 9, pp. 1667–1670, Mar. 1997, doi: 10.1103/PhysRevLett.78.1667.

[26] S. Nie and S. R. Emory, “Probing Single Molecules and Single Nanoparticles by Surface-Enhanced Raman Scattering,” *Science*, vol. 275, no. 5303, pp. 1102–1106, Feb. 1997, doi: 10.1126/science.275.5303.1102.

[27] A. Hartstein, J. R. Kirtley, and J. C. Tsang, “Enhancement of the Infrared Absorption from Molecular Monolayers with Thin Metal Overlayers,” *Phys. Rev. Lett.*, vol. 45, no. 3, pp. 201–204, Jul. 1980, doi: 10.1103/PhysRevLett.45.201.

[28] M. Osawa, K.-I. Ataka, K. Yoshii, and Y. Nishikawa, “Surface-Enhanced Infrared Spectroscopy: The Origin of the Absorption Enhancement and Band Selection Rule in the Infrared Spectra of Molecules Adsorbed on Fine Metal Particles,” *Appl. Spectrosc.*, vol. 47, no. 9, pp. 1497–1502, Sep. 1993.

[29] R. Adato *et al.*, “Ultra-sensitive vibrational spectroscopy of protein monolayers with plasmonic nanoantenna arrays,” *Proc. Natl. Acad. Sci.*, vol. 106, no. 46, pp. 19227–19232, Nov. 2009, doi: 10.1073/pnas.0907459106.

[30] L. Razzari *et al.*, “Terahertz Dipole Nanoantenna Arrays: Resonance Characteristics,” *Plasmonics*, vol. 8, no. 1, pp. 133–138, Mar. 2013, doi: 10.1007/s11468-012-9439-0.

[31] A. Toma *et al.*, “Squeezing Terahertz Light into Nanovolumes: Nanoantenna Enhanced Terahertz Spectroscopy (NETS) of Semiconductor Quantum Dots,” *Nano Lett.*, vol. 15, no. 1, pp. 386–391, Jan. 2015, doi: 10.1021/nl503705w.

[32] X. Jin *et al.*, “Reshaping the phonon energy landscape of nanocrystals inside a terahertz plasmonic nanocavity,” *Nat. Commun.*, vol. 9, no. 1, p. 763, Feb. 2018, doi: 10.1038/s41467-018-03120-3.

[33] P. Biagioni, J.-S. Huang, and B. Hecht, “Nanoantennas for visible and infrared radiation,” *Rep. Prog. Phys.*, vol. 75, no. 2, p. 024402, Feb. 2012, doi: 10.1088/0034-4885/75/2/024402.

[34] K. B. Crozier, A. Sundaramurthy, G. S. Kino, and C. F. Quate, “Optical antennas: Resonators for local field enhancement,” *J. Appl. Phys.*, vol. 94, no. 7, pp. 4632–4642, Oct. 2003, doi: 10.1063/1.1602956.

[35] K. Ueno, S. Nozawa, and H. Misawa, “Surface-enhanced terahertz spectroscopy using gold rod structures resonant with terahertz waves,” *Opt. Express*, vol. 23, no. 22, p. 28584, Nov. 2015, doi: 10.1364/OE.23.028584.

[36] J. B. Khurgin, “How to deal with the loss in plasmonics and metamaterials,” *Nat. Nanotechnol.*, vol. 10, no. 1, pp. 2–6, Jan. 2015, doi: 10.1038/nnano.2014.310.

[37] S. V. Boriskina *et al.*, “Losses in plasmonics: from mitigating energy dissipation to embracing loss-enabled functionalities,” *Adv. Opt. Photonics*, vol. 9, no. 4, p. 775, Dec. 2017, doi: 10.1364/AOP.9.000775.

[38] P. R. West, S. Ishii, G. V. Naik, N. K. Emani, V. M. Shalaev, and A. Boltasseva, “Searching for better plasmonic materials,” *Laser Photonics Rev.*, vol. 4, no. 6, pp. 795–808, doi: 10.1002/lpor.200900055.

[39] G. V. Naik, J. Kim, and A. Boltasseva, “Oxides and nitrides as alternative plasmonic materials in the optical range [Invited],” *Opt. Mater. Express*, vol. 1, no. 6, pp. 1090–1099, Oct. 2011, doi: 10.1364/OME.1.001090.

[40] A. Boltasseva and H. A. Atwater, “Low-Loss Plasmonic Metamaterials,” *Science*, vol. 331, no. 6015, pp. 290–291, Jan. 2011, doi: 10.1126/science.1198258.

[41] P. J. Schuck, D. P. Fromm, A. Sundaramurthy, G. S. Kino, and W. E. Moerner, “Improving the Mismatch between Light and Nanoscale Objects with Gold Bowtie Nanoantennas,” *Phys. Rev. Lett.*, vol. 94, no. 1, Jan. 2005, doi: 10.1103/PhysRevLett.94.017402.

[42] J. Zuloaga, E. Prodan, and P. Nordlander, “Quantum Description of the Plasmon Resonances of a Nanoparticle Dimer,” *Nano Lett.*, vol. 9, no. 2, pp. 887–891, Feb. 2009, doi: 10.1021/nl803811g.

[43] D. Sarid and W. Challener, *Modern Introduction to Surface Plasmons: Theory, Mathematica Modeling and Applications*. Cambridge: Cambridge University Press, 2010.

[44] W. L. Stutzman and G. A. Thiele, *Antenna Theory and Design*. John Wiley & Sons, 2012.

[45] L. Novotny, “Effective Wavelength Scaling for Optical Antennas,” *Phys. Rev. Lett.*, vol. 98, no. 26, Jun. 2007, doi: 10.1103/PhysRevLett.98.266802.

[46] D. F. P. Pile and D. K. Gramotnev, “Adiabatic and nonadiabatic nanofocusing of plasmons by tapered gap plasmon waveguides,” *Appl. Phys. Lett.*, vol. 89, no. 4, p. 041111, Jul. 2006, doi: 10.1063/1.2236219.

[47] D. K. Gramotnev, M. W. Vogel, and M. I. Stockman, “Optimized nonadiabatic nanofocusing of plasmons by tapered metal rods,” *J. Appl. Phys.*, vol. 104, no. 3, p. 034311, Aug. 2008, doi: 10.1063/1.2963699.

[48] S. Thomas, G. Wachter, C. Lemell, J. Burgdörfer, and P. Hommelhoff, “Large optical field enhancement for nanotips with large opening angles,” *New J. Phys.*, vol. 17, no. 6, p. 063010, Jun. 2015, doi: 10.1088/1367-2630/17/6/063010.

[49] S. Kawata, Ed., *Near-field optics and surface plasmon polaritons*. Berlin ; New York: Springer, 2001.

[50] J. Yang, F. Kong, K. Li, and J. Zhao, “Optimizing the bowtie nano-antenna for enhanced purcell factor and electric field,” *Prog. Electromagn. Res. Lett.*, vol. 44, pp. 93–99, 2014, doi: 10.2528/PIERL13091613.

[51] G. Bi *et al.*, “Optical properties of gold nano-bowtie structures,” *Opt. Commun.*, vol. 294, pp. 213–217, May 2013, doi: 10.1016/j.optcom.2012.12.080.

[52] W. Ding, R. Bachelot, S. Kostcheev, and P. Royer, “Surface plasmon resonances in silver Bowtie nanoantennas with varied bow angles,” *J Appl Phys*, p. 7.

[53] H. Fischer and O. J. F. Martin, “Engineering the optical response of plasmonic nanoantennas,” *Opt. Express*, vol. 16, no. 12, p. 9144, Jun. 2008, doi: 10.1364/OE.16.009144.

[54] S. A. Maier, *Plasmonics: Fundamentals and Applications*. Springer US, 2007.

[55] E. Kretschmann and H. Raether, “Radiative Decay of Non Radiative Surface Plasmons Excited by Light,” *Z. Für Naturforschung A*, vol. 23, no. 12, pp. 2135–2136, 2014, doi: 10.1515/zna-1968-1247.

[56] A. Otto, “Excitation of nonradiative surface plasma waves in silver by the method of frustrated total reflection,” *Z. Für Phys. Hadrons Nucl.*, vol. 216, no. 4, pp. 398–410, Aug. 1968, doi: 10.1007/BF01391532.

[57] V. Amendola, R. Pilot, M. Frasconi, O. M. Maragò, and M. A. Iatì, “Surface plasmon resonance in gold nanoparticles: a review,” *J. Phys. Condens. Matter*, vol. 29, no. 20, p. 203002, May 2017, doi: 10.1088/1361-648X/aa60f3.

[58] S. W. Prescott and P. Mulvaney, “Gold nanorod extinction spectra,” *J. Appl. Phys.*, vol. 99, no. 12, p. 123504, Jun. 2006, doi: 10.1063/1.2203212.

[59] G. W. Bryant, F. J. García de Abajo, and J. Aizpurua, “Mapping the Plasmon Resonances of Metallic Nanoantennas,” *Nano Lett.*, vol. 8, no. 2, pp. 631–636, Feb. 2008, doi: 10.1021/nl073042v.

[60] E. Feigenbaum and M. Orenstein, “Ultrasmall Volume Plasmons, yet with Complete Retardation Effects,” *Phys. Rev. Lett.*, vol. 101, no. 16, Oct. 2008, doi: 10.1103/PhysRevLett.101.163902.

[61] R. Gordon, “Reflection of Cylindrical Surface Waves,” *Opt. Express*, vol. 17, no. 21, pp. 18621–18629, Oct. 2009, doi: 10.1364/OE.17.018621.

[62] R. Gordon, “Vectorial method for calculating the Fresnel reflection of surface plasmon polaritons,” *Phys. Rev. B*, vol. 74, no. 15, p. 153417, Oct. 2006, doi: 10.1103/PhysRevB.74.153417.

[63] T. Yoshie *et al.*, “Vacuum Rabi splitting with a single quantum dot in a photonic crystal nanocavity,” *Nature*, vol. 432, no. 7014, pp. 200–203, Nov. 2004, doi: 10.1038/nature03119.

[64] Z.-J. Yang, T. J. Antosiewicz, and T. Shegai, “Role of material loss and mode volume of plasmonic nanocavities for strong plasmon-exciton interactions,” *Opt. Express*, vol. 24, no. 18, p. 20373, Sep. 2016, doi: 10.1364/OE.24.020373.

[65] A. F. Koenderink, “On the use of Purcell factors for plasmon antennas,” *Opt. Lett.*, vol. 35, no. 24, p. 4208, Dec. 2010, doi: 10.1364/OL.35.004208.

[66] V. Aglieri *et al.*, “Improving nanoscale terahertz field localization by means of sharply tapered resonant nanoantennas,” *Nanophotonics*, vol. 9, no. 3, pp. 683–690, Feb. 2020, doi: 10.1515/nanoph-2019-0459.

[67] C.-H. Lee *et al.*, “Boosted photocatalytic efficiency through plasmonic field confinement with bowtie and diabolo nanostructures under LED irradiation,” *Opt. Express*, vol. 24, no. 16, p. 17541, Aug. 2016, doi: 10.1364/OE.24.017541.

[68] M. Walther, D. G. Cooke, C. Sherstan, M. Hajar, M. R. Freeman, and F. A. Hegmann, “Terahertz conductivity of thin gold films at the metal-insulator percolation transition,” *Phys. Rev. B*, vol. 76, no. 12, Sep. 2007, doi: 10.1103/PhysRevB.76.125408.

[69] W. Zhang, X. Cui, and O. J. F. Martin, “Local field enhancement of an infinite conical metal tip illuminated by a focused beam,” *J. Raman Spectrosc.*, vol. 40, no. 10, pp. 1338–1342, 2009, doi: 10.1002/jrs.2439.

[70] R. W. Wood, “On a Remarkable Case of Uneven Distribution of Light in a Diffraction Grating Spectrum,” *Proc. Phys. Soc. Lond.*, vol. 18, no. 1, pp. 269–275, Jun. 1902, doi: 10.1088/1478-7814/18/1/325.

[71] Lord Rayleigh, “On the Dynamical Theory of Gratings,” *Proc. R. Soc. Lond. Ser. Contain. Pap. Math. Phys. Character*, vol. 79, no. 532, pp. 399–416, 1907.

[72] J.-Y. Kim *et al.*, “Terahertz Quantum Plasmonics of Nanoslot Antennas in Nonlinear Regime,” *Nano Lett.*, vol. 15, no. 10, pp. 6683–6688, Oct. 2015, doi: 10.1021/acs.nanolett.5b02505.

[73] E. M. Purcell, “Spontaneous Emission Probabilities at Radio Frequencies,” in *Confined Electrons and Photons*, vol. 340, E. Burstein and C. Weisbuch, Eds. Boston, MA: Springer US, 1995, pp. 839–839.

[74] P. Törmä and W. L. Barnes, “Strong coupling between surface plasmon polaritons and emitters: a review,” *Rep. Prog. Phys.*, vol. 78, no. 1, p. 013901, Dec. 2014, doi: 10.1088/0034-4885/78/1/013901.

[75] H. Deng, H. Haug, and Y. Yamamoto, “Exciton-polariton Bose-Einstein condensation,” *Rev. Mod. Phys.*, vol. 82, no. 2, pp. 1489–1537, May 2010, doi: 10.1103/RevModPhys.82.1489.

[76] A. F. Kockum, A. Miranowicz, S. De Liberato, S. Savasta, and F. Nori, “Ultrastrong coupling between light and matter,” *Nat. Rev. Phys.*, vol. 1, no. 1, pp. 19–40, Jan. 2019, doi: 10.1038/s42254-018-0006-2.

[77] S. Savasta, R. Saija, A. Ridolfo, O. Di Stefano, P. Denti, and F. Borghese, “Nanopolaritons: Vacuum Rabi Splitting with a Single Quantum Dot in the Center of a Dimer Nanoantenna,” *ACS Nano*, vol. 4, no. 11, pp. 6369–6376, Nov. 2010, doi: 10.1021/nn100585h.

[78] F. P. Laussy, E. del Valle, and C. Tejedor, “Luminescence spectra of quantum dots in microcavities. I. Bosons,” *Phys. Rev. B*, vol. 79, no. 23, Jun. 2009, doi: 10.1103/PhysRevB.79.235325.

[79] M. Aspelmeyer, T. J. Kippenberg, and F. Marquardt, “Cavity optomechanics,” *Rev. Mod. Phys.*, vol. 86, no. 4, pp. 1391–1452, Dec. 2014, doi: 10.1103/RevModPhys.86.1391.

[80] S. Rudin and T. L. Reinecke, “Oscillator model for vacuum Rabi splitting in microcavities,” *Phys. Rev. B*, vol. 59, no. 15, pp. 10227–10233, Apr. 1999, doi: 10.1103/PhysRevB.59.10227.

[81] Frohlich H., *Theory Of Dielectrics*. 1949.

[82] H. S. Nalwa, Ed., *Light Scattering of Semiconducting Nanoparticles in Encyclopedia of nanoscience and nanotechnology. v. 1-10*. Stevenson Ranch, Calif: American Scientific Publishers, 2004.

[83] S. M. Hein and H. Giessen, “Tailoring Magnetic Dipole Emission with Plasmonic Split-Ring Resonators,” *Phys. Rev. Lett.*, vol. 111, no. 2, Jul. 2013, doi: 10.1103/PhysRevLett.111.026803.

[84] T. D. Corrigan, P. W. Kolb, A. B. Sushkov, H. D. Drew, D. C. Schmadel, and R. J. Phaneuf, “Optical plasmonic resonances in split-ring resonator structures: an improved LC model,” *Opt. Express*, vol. 16, no. 24, p. 19850, Nov. 2008, doi: 10.1364/OE.16.019850.

[85] A. W. Clark, A. Glidle, D. R. S. Cumming, and J. M. Cooper, “Plasmonic Split-Ring Resonators as Dichroic Nanophotonic DNA Biosensors,” *J. Am. Chem. Soc.*, vol. 131, no. 48, pp. 17615–17619, Dec. 2009, doi: 10.1021/ja905910q.

[86] X. Jin and V. Aglieri, “Moon-shaped Antennas for Enhanced Phonon Resonance Reshape of CdS Nanocrystals.” *In preparation*

[87] A. Shalabney, J. George, J. Hutchison, G. Pupillo, C. Genet, and T. W. Ebbesen, “Coherent coupling of molecular resonators with a microcavity mode,” *Nat. Commun.*, vol. 6, no. 1, May 2015, doi: 10.1038/ncomms6981.

[88] A. Shalabney *et al.*, “Enhanced Raman Scattering from Vibro-Polariton Hybrid States,” *Angew. Chem. Int. Ed.*, vol. 54, no. 27, pp. 7971–7975, 2015, doi: 10.1002/anie.201502979.

[89] A. Thomas *et al.*, “Ground-State Chemical Reactivity under Vibrational Coupling to the Vacuum Electromagnetic Field,” *Angew. Chem. Int. Ed.*, vol. 55, no. 38, pp. 11462–11466, 2016, doi: 10.1002/anie.201605504.

[90] R. M. A. Vergauwe *et al.*, “Quantum Strong Coupling with Protein Vibrational Modes,” *J. Phys. Chem. Lett.*, vol. 7, no. 20, pp. 4159–4164, Oct. 2016, doi: 10.1021/acs.jpclett.6b01869.

[91] J. George, A. Shalabney, J. A. Hutchison, C. Genet, and T. W. Ebbesen, “Liquid-Phase Vibrational Strong Coupling,” *J. Phys. Chem. Lett.*, vol. 6, no. 6, pp. 1027–1031, Mar. 2015, doi: 10.1021/acs.jpclett.5b00204.

[92] A. Beveratos, R. Brouri, T. Gacoin, J.-P. Poizat, and P. Grangier, “Nonclassical radiation from diamond nanocrystals,” *Phys. Rev. A*, vol. 64, no. 6, Nov. 2001, doi: 10.1103/PhysRevA.64.061802.

[93] Y.-S. Park, A. K. Cook, and H. Wang, “Cavity QED with Diamond Nanocrystals and Silica Microspheres,” *Nano Lett.*, vol. 6, no. 9, pp. 2075–2079, Sep. 2006, doi: 10.1021/nl061342r.

[94] K. Hennessy *et al.*, “Quantum nature of a strongly coupled single quantum dot–cavity system,” *Nature*, vol. 445, no. 7130, pp. 896–899, Feb. 2007, doi: 10.1038/nature05586.

[95] M. G. Panthani and B. A. Korgel, “Nanocrystals for Electronics,” *Annu. Rev. Chem. Biomol. Eng.*, vol. 3, no. 1, pp. 287–311, Jul. 2012, doi: 10.1146/annurev-chembioeng-062011-081040.

[96] A. F. Kockum, A. Miranowicz, V. Macrì, S. Savasta, and F. Nori, “Deterministic quantum nonlinear optics with single atoms and virtual photons,” *Phys. Rev. A*, vol. 95, no. 6, p. 063849, Jun. 2017, doi: 10.1103/PhysRevA.95.063849.

[97] E. Sánchez-Burillo, D. Zueco, J. García-Ripoll, and L. Martín-Moreno, “Scattering in the ultrastrong regime: nonlinear optics with one photon,” *Phys. Rev. Lett.*, vol. 113, no. 26, p. 263604, Dec. 2014, doi: 10.1103/PhysRevLett.113.263604.

[98] R. Stassi *et al.*, “Quantum Nonlinear Optics without Photons,” *Phys. Rev. A*, vol. 96, no. 2, p. 023818, Aug. 2017, doi: 10.1103/PhysRevA.96.023818.

[99] M.-E. Kleemann *et al.*, “Strong-coupling of WSe_2 in ultra-compact plasmonic nanocavities at room temperature,” *Nat. Commun.*, vol. 8, no. 1, Dec. 2017, doi: 10.1038/s41467-017-01398-3.

[100] W. Liu *et al.*, “Strong Exciton–Plasmon Coupling in MoS_2 Coupled with Plasmonic Lattice,” *Nano Lett.*, vol. 16, no. 2, pp. 1262–1269, Feb. 2016, doi: 10.1021/acs.nanolett.5b04588.

[101] L. Liu, L. Y. M. Tobing, J. Tong, D. H. Zhang, F. J. Garcia-Vidal, and Y. Luo, “Room temperature strong coupling of monolayer WS2 with gold nanoantennae,” in *2017*

Progress in Electromagnetics Research Symposium - Fall (PIERS - FALL), Nov. 2017, pp. 2578–2580, doi: 10.1109/PIERS-FALL.2017.8293570.

[102] L. Zhang, R. Gogna, W. Burg, E. Tutuc, and H. Deng, “Photonic-crystal exciton-polaritons in monolayer semiconductors,” *Nat. Commun.*, vol. 9, no. 1, Dec. 2018, doi: 10.1038/s41467-018-03188-x.

[103] A. Ridolfo, S. Savasta, and M. J. Hartmann, “Nonclassical Radiation from Thermal Cavities in the Ultrastrong Coupling Regime,” *Phys. Rev. Lett.*, vol. 110, no. 16, p. 163601, Apr. 2013, doi: 10.1103/PhysRevLett.110.163601.

[104] M. Cirio, K. Debnath, N. Lambert, and F. Nori, “Amplified Optomechanical Transduction of Virtual Radiation Pressure,” *Phys. Rev. Lett.*, vol. 119, no. 5, Jul. 2017, doi: 10.1103/PhysRevLett.119.053601.

[105] L. Garziano, A. Ridolfo, R. Stassi, O. Di Stefano, and S. Savasta, “Switching on and off of ultrastrong light-matter interaction: Photon statistics of quantum vacuum radiation,” *Phys. Rev. A*, vol. 88, no. 6, Dec. 2013, doi: 10.1103/PhysRevA.88.063829.

[106] M. Steiner *et al.*, “Phonon populations and electrical power dissipation in carbon nanotube transistors,” *Nat. Nanotechnol.*, vol. 4, no. 5, pp. 320–324, May 2009, doi: 10.1038/nnano.2009.22.

[107] A. A. Bakulin *et al.*, “Mode-selective vibrational modulation of charge transport in organic electronic devices,” *Nat. Commun.*, vol. 6, no. 1, Nov. 2015, doi: 10.1038/ncomms8880.

[108] D. Bozyigit *et al.*, “Soft surfaces of nanomaterials enable strong phonon interactions,” *Nature*, vol. 531, no. 7596, pp. 618–622, Mar. 2016, doi: 10.1038/nature16977.

[109] T. Chervy *et al.*, “Vibro-Polaritonic IR Emission in the Strong Coupling Regime,” *ACS Photonics*, vol. 5, no. 1, pp. 217–224, Jan. 2018, doi: 10.1021/acsphotonics.7b00677.

[110] V. Aglieri *et al.*, “Resistive switching in microscale anodic titanium dioxide-based memristors,” *Superlattices Microstruct.*, vol. 113, pp. 135–142, Jan. 2018, doi: 10.1016/j.spmi.2017.10.031.

[111] V. Aglieri *et al.*, “Forming-Free and Self-Rectifying Resistive Switching Effect in Anodic Titanium Dioxide-Based Memristors,” in *2018 IEEE 4th International Forum on Research and Technology for Society and Industry (RTSI)*, Sep. 2018, pp. 1–4, doi: 10.1109/RTSI.2018.8548396.

[112] G. Balistreri *et al.*, “Design and Fabrication of Terahertz Bragg Gratings on a Two-Wire Waveguide,” *Photonic North 2018*.

[113] F. Yue *et al.*, “Highly Sensitive Polarization Rotation Measurement through a High-Order Vector Beam Generated by a Metasurface,” *Adv. Mater. Technol.*, p. 1901008, Jan. 2020, doi: 10.1002/admt.201901008.

[114] F. Yue *et al.*, “Rotational Doppler frequency shift from time-evolving high-order Pancharatnam-Berry phase.” *In preparation*

[115] G. H. Bernstein, D. A. Hill, and W. Liu, “New high-contrast developers for poly(methyl methacrylate) resist,” *J. Appl. Phys.*, vol. 71, no. 8, pp. 4066–4075, Apr. 1992, doi: 10.1063/1.350831.

[116] G. S. May and S. M. Sze, *Fundamentals of Semiconductor Fabrication*. Wiley, 2003.

[117] C. Mack, *Fundamental Principles of Optical Lithography*. Chichester, UK: John Wiley & Sons, Ltd, 2007.

[118] L. Holland, *Vacuum Deposition of Thin Films*. Springer US, 1956.

[119] J. D. Plummer, *Silicon VLSI Technology: Fundamentals, Practice and Modeling*. Dorling Kindersley, 2009.

[120] D. F. Kyser and N. S. Viswanathan, “Monte Carlo simulation of spatially distributed beams in electron-beam lithography,” *J. Vac. Sci. Technol.*, vol. 12, no. 6, pp. 1305–1308, Nov. 1975, doi: 10.1116/1.568524.

SOMMAIRE RÉCAPITULATIF (Summary in French)

1 Introduction

Les ondes électromagnétiques dans la gamme de fréquences comprises entre 0,1 et 10 Térahertz (THz) sont caractérisées par des propriétés particulières, telles que le caractère non ionisant (qui permet de mener des expériences non destructives sur des matériaux biologiques, tels que les tissus humains), la matériaux généralement opaques dans d'autres régimes de fréquence (par exemple bois, tissu, etc.) [1], et la position de fréquence située entre les régimes électronique (GHz) et photonique (PHz) [2], promettant ainsi de grandes améliorations sur l'état actuel de la technologie de l'information. Cependant, en raison de la difficulté de produire des sources et des détecteurs ayant un coût abordable à ces fréquences, le régime THz est appelé depuis de nombreuses années le «THz-gap» [1], [2]. Ces limitations ont été surmontées au cours des dernières décennies [1] grâce à l'attention des scientifiques et de l'industrie issue de la pléthore d'applications prometteuses: technologie de télécommunication rapide [3], imagerie et détection pour le contrôle de sécurité des emballages scellés et l'inspection personnelle [4], [5], et processus industriel et contrôle de la qualité [6], pour ne citer que quelques exemples.

Parmi toutes les applications possibles de la technologie THz, la spectroscopie est l'un des outils les plus prometteurs pour l'étude des processus de physique fondamentale. Ceci parce qu'un grand nombre d'excitations élémentaires se situent dans la plage THz, telles que la transition en rotation de molécules [7], mouvement de grande amplitude de molécules biologiques [8], vibration du réseau dans les solides [9], transitions intra-bande dans les semi-conducteurs [10], [11], parmi d'autres [1], [2]. Tout cela rendre la spectroscopie THz extrêmement attrayante pour les chercheurs de nombreux domaines comme les physiciens, ingénieurs, médecins et chimistes. Néanmoins, en raison de la grande longueur d'onde associée à cette gamme de fréquences (~300 µm à 1 THz), les particules de taille micrométrique et nanométrique sont pratiquement invisibles pour les longues ondes THz [12] [13] en raison de la faible sensibilité et de la faible résolution spatiale qui limitent son utilisation à des matériaux volumineux ou à de gros agrégats de petites particules.

Pour surmonter cet obstacle, de nombreuses tentatives ont été menées. Gallot et al. [14] conçue une plate-forme de détection THz constituée de guides d'ondes circulaires et rectangulaires. Il a été constaté que, pour le guide d'onde rectangulaire, il était possible d'augmenter la sensibilité de la mesure jusqu'à 50 fois celle de la mesure par réflexion en une seule passe. Ainsi, une telle technique a été utilisée dans la détection de matériaux en

tant que molécules biologiques [15], drogues et explosifs solides [16]. Malheureusement, même s'il est possible de récupérer les informations spectroscopiques du spécimen étudié, la sensibilité accrue offerte par les guides d'ondes n'est obtenue que si le spécimen est déposé sur toute la surface de la plate-forme.

Aussi métamatériaux [17] et metasurfaces [18] ont été utilisés comme plates-formes de détection améliorées dans le régime THz. Par exemple, dans [12], une métasurface est conçue comme un petit espace au centre d'une structure métallique (le «gap») carrée régulièrement répartie sur un substrat transparent au THz. Le dispositif a été préalablement fonctionnalisé pour attirer les micro-organismes, tels que les bactéries, puis sondé par la technique THz-TDS. En comparant la caractérisation THz de l'échantillon avec et sans les micro-organismes, un décalage de la résonance de la métasurface est détecté. Un tel décalage est dû au changement d'indice de réfraction du milieu entourant la métasurface provoqué dans ce cas par la présence de microorganismes. De plus, il a été démontré qu'un changement d'indice de réfraction est détecté même pour une très petite quantité de microorganismes, obtenant ainsi finalement un capteur de changement d'indice de réfraction de haute sensibilité. Cependant, les métasurfaces ainsi conçues ne peuvent détecter qu'un changement d'indice de réfraction et ne sont pas en mesure de récupérer les informations spectroscopiques des microorganismes déposés.

Un autre développement de l'étude de l'interaction THz lumière-matière provient de la réalisation de nanoslot comme plate-forme de détection THz. Ces dispositifs ont été utilisés pour la détection de très petites quantités de matériaux grâce à la forte amélioration de champ obtenue grâce au comportement capacitif commandé par la lumière de nanoslots [18], [19]. En effet, en exploitant le facteur de rehaussement de champ élevé obtenu dans de telles structures, il est possible d'améliorer considérablement le coefficient d'absorption THz des matériaux même s'ils sont présents en très petites quantités. Park et al. [19] ont montré que des nanoslot conçues pour résonner sur le RDX (lignes d'absorption de 1,3,5-trinitroperhydro-1,3,5-triazine) et de lactose (dans le régime THz) peuvent être détectées même s'il n'y a que des dizaines de des nanogrammes de molécules projetées au-dessus des nanoslot (ce qui correspond à quelques femtogrammes de matériau à l'intérieur des nanoslot). Cette présence est observée par une chute constante de la valeur du spectre de transmission par rapport au spectre de transmission obtenu en caractérisant optiquement les nanoslots nus. De plus, dans [20], il est démontré la possibilité de faire la distinction entre différents composés chimiques en utilisant des nanoslot. Exploitant la même technique que celle utilisée dans [19], deux conceptions nanostructures (c.-à-d. des longueurs de nanoslot différentes) ont été configurées sur deux échantillons séparés. Les deux ensembles de nanotubes ont été choisis afin de résonner près de la raie d'absorption des

sucres D-glucose et fructose. Ainsi, recouvrant le même échantillon de sucres D-glucose et de fructose (un demi échantillon recouvert de D-glucose et l'autre recouvert de fructose), seules les molécules de sucre dont la raie d'absorption est proche de la fréquence de résonance de la nanotache de cet échantillon sont détectée. Cela est dû au fait que les nanoslot accumulent un rehaussement de champ capable d'augmenter considérablement le coefficient d'absorption du sucre avec une ligne d'absorption plus proche. De cette manière, il a également été démontré la haute sélectivité de cette plate-forme de détection THz, non seulement pour les molécules de sucre, mais également pour d'autres composés chimiques. Néanmoins, même si ces derniers cas ont montré une amélioration considérable de l'utilisation de l'onde THz pour la détection, il n'était toujours pas suffisant de récupérer les informations spectroscopiques du spécimen étudié.

Au cours des dernières décennies, les effets de rehaussement de surface ont été largement utilisés pour améliorer la sensibilité de la spectroscopie traditionnelle en utilisant des surfaces ondulées et des particules métalliques dont la taille caractéristique est bien inférieure à la longueur d'onde d'excitation entrante. Par exemple, la spectroscopie Raman est connue pour être un processus intrinsèquement inefficace [21], mais en utilisant la spectroscopie Raman améliorée en surface (SERS) [22], [23] il est possible d'améliorer considérablement sa sensibilité, de sorte qu'il est possible de caractériser peu de molécules ou même de simples particules [24]–[26]. La même approche a été utilisée pour améliorer la spectroscopie infrarouge. L'absorption infrarouge en surface améliorée (SEIRA) est capable d'atteindre une sensibilité élevée pour la spectroscopie par absorption directe, là encore sur une petite quantité de matériau [27]–[29]. SERS et SEIRA sont particulièrement sensibles aux valeurs de champ local et tirent donc un grand avantage de l'effet d'amélioration de surface en raison du champ très élevé obtenu dans ce type de structures.

En suivant les progrès récents en matière de détection de métasurface améliorée dans le régime THz et les techniques d'amélioration de surface, Razzari et al. [30] ont proposé une nouvelle plate-forme consistant en un réseau des nanoantennes (NAs) dipolaires en or résonnant dans la gamme THz. Ils démontrent des valeurs de rehaussement de champ élevées aux extrémités NA qui peuvent être utilisées pour améliorer considérablement la sensibilité des techniques de spectroscopie à base de THz. Quelques années plus tard, Toma et al. [31], ont montré qu'en modifiant correctement la structure matricielle de la réf. [30] il est possible d'obtenir une résonance large bande et un champ plus proche amélioré dans la zone de l'intervalle. Grâce au couplage, l'augmentation a atteint un niveau tel que la section efficace d'absorption des matériaux de taille nanométrique placés dans l'espace était plus de un million de fois supérieure à celle non assistée par spectroscopie THz. Ainsi, en plaçant des points quantiques de séléniure de cadmium (CdSe) sur des espaces NA, ses

informations spectroscopiques ont été rapidement récupérées en raison du couplage entre le champ NA fortement amélioré et la résonance de phonons des points quantiques CdSe, aboutissant enfin à une résonance de type Fano visible dans les spectres de transmission THz. De tels progrès ont été récemment exploités par Jin et al. [32] où ils ont non seulement été capables de détecter les informations spectroscopiques des nano-cristaux de sulfure de cadmium (CdS), mais également de remodeler leur résonance phononique sous couplage fort lumière-matière (de plus amples informations à ce sujet sont présentées à la Section (4.3)).

Ces avancées ont été obtenues grâce à la capacité unique des NAs plasmoniques de convertir le rayonnement à propagation libre en champ proche fortement localisé [33]–[35], faisant ainsi interagir de très longues ondes THz avec des nano-objets [13], [30], [31]. Cependant, malgré les bons résultats obtenus jusqu'à présent, il est encore possible d'améliorer les performances des NA plasmoniques, en raison de la perte subie par les ondes de surface [36], [37] parcourant ces dispositifs. Néanmoins, en mettant au point des structures NA plasmoniques précises, il sera démontré qu'il est possible d'augmenter le champ proche et de réduire le volume de mode (le volume contenant le champ proche), pour atteindre enfin des performances améliorées de la capacité NA capables de détecter - idéalement - jusqu'à un seul nano-objet.

1.1 Amélioration des Performances de Nanoantennes

Malgré les expériences réussies qui viennent d'être présentées sur l'étude des informations spectroscopiques de matériaux et de composés dans le régime THz, les performances des NA pourraient être améliorées pour obtenir de meilleurs résultats et donc plus d'informations.

La raison pour laquelle les NA n'ont pas encore été entièrement optimisées est principalement due à la nature intrinsèquement destructrice des métaux à ces fréquences [36]. De nombreux métaux ont été étudiés en tant que matériaux pour la fabrication d'NA, tels que l'aluminium, l'argent, les métaux alcalins et l'or [38], etc. Les semi-conducteurs ont également été étudiés en tant que matériaux alternatifs pour les NA en raison de la possibilité d'accorder la concentration en porteurs par l'introduction d'impuretés (dopage) et de leur température de fusion plus élevée (paramètre souhaitable, en particulier pour les expériences non linéaires). Néanmoins, les semi-conducteurs souffrent également de pertes très élevées [39]. Parmi ces matériaux, l'un des plus largement utilisé est l'or en raison de sa bonne conductivité [40], mais principalement pour sa stabilité chimique par rapport à d'autres matériaux (par exemple, l'aluminium est caractérisé par une conductivité plus élevée mais une stabilité chimique médiocre).

Alternativement, il est possible d'assouplir les pertes à l'intérieur de la NA en adoptant une stratégie géométrique. En particulier, il a été démontré théoriquement et expérimentalement que la longueur de l'antenne influe sur le renforcement du champ proche produit par la NA [41], [42]. Dans le même temps, la longueur de l'antenne est le paramètre qui détermine la fréquence de résonance de NA et la plupart du temps, celle-ci doit résonner dans une plage de fréquences spécifique. Par conséquent, la longueur de l'antenne ne peut pas être modifiée et cette méthode ne peut pas être utilisée pour améliorer le renforcement du champ NA dans la plupart des cas.

Comme on le voit dans les travaux de Toma et al. [31], en couplant les NAs, il est possible d'améliorer considérablement l'amélioration du champ dans l'écart entre les NAs. D'autres études sur la taille de l'écart ont montré qu'en modifiant les caractéristiques, telles que la largeur et la hauteur de l'écart, il était possible d'améliorer le champ amélioré. Supposons avoir une paire des NAs couplée de bout en bout. La largeur de l'intervalle est déterminée par la distance entre les NAs formant la paire couplée. Pour obtenir des valeurs de rehaussement de champ plus élevées, les NAs peuvent se rapprocher les uns des autres [43]. Cependant, même si les techniques modernes de nanofabrication permettent la création d'un espace d'antenne minuscule, une largeur d'espace trop réduite conduit à la tunnellisation des électrons à travers l'espace, formant ainsi une antenne plus longue unique [44] et rendant cette stratégie inefficace. La hauteur de l'intervalle, déterminée par la largeur de NA, peut également être modifiée pour améliorer la mise en valeur du champ. En réduisant notamment la largeur de l'antenne (ou l'équivalent de la hauteur de l'intervalle), on obtient une amélioration du champ plus élevée, mais des NAs trop étroites entraînent à leur tour des écarts très étroits, générant ainsi une perte importante [45]. Ce dernier problème affecte particulièrement la performance des NAs employées dans le régime THz, en raison du très grand facteur de forme des NAs de THz. En fait, comme nous le verrons en détail dans le chapitre suivant, la longueur de NA est liée à la longueur d'onde de résonance sous la forme $L \approx \lambda_{\mathrm{res}}/2n_{\mathrm{eff}}$, donc si le NA résonne à 1 THz, soit 300 µm, le rapport de format $AS = L/w$, avec une largeur d'antenne w, s'avère extrêmement grand [46], [47].

Il convient de noter que la largeur et la hauteur de l'écart doivent être conçues en tenant compte également de l'application dans laquelle les NAs seront utilisées. Par exemple, si des NA sont utilisées pour l'étude des caractéristiques spectroscopiques des nanocristaux, la taille de l'intervalle doit être suffisamment grande pour contenir un nombre suffisant de nano-cristaux, de sorte à pouvoir restituer un signal cohérent à partir des caractérisations optiques, introduisant enfin une autre contrainte dans les caractéristiques géométriques des NA.

L’amélioration du champ proche est alors un défi de taille, difficile à réaliser. Les matériaux à faibles pertes disponibles et les contraintes géométriques rendent les stratégies d'amélioration vues jusqu'à présent limitées. Néanmoins, pour obtenir une localisation et une mise à niveau de champ plus élevées, des géométries alternatives ont également été proposées dans le passé pour améliorer les performances de NA. Par exemple, il a été démontré numériquement que des guides d’onde effilés de longueur semi-infinie produisaient une densité d’énergie plasmonique 20 fois plus élevée à la pointe [48], et des tiges coniques en or non résonantes ont été simulées, offrant une forte amélioration du champ proche tout en optimisant l'angle de conicité [49], [50]. Les géométries coniques ont donc attiré beaucoup d'attention grâce au champ très localisé à leurs extrémités les plus petites [33], [48], qui permet en principe de mener des expériences améliorées d'imagerie et de spectroscopie à l'échelle nanométrique [51]. Cependant, il a été démontré que les antennes NA coniques, appelées antennes «bowtie», produisaient dans le régime IR une plus grande largeur de bande aux dépens de l’amélioration de champ plus faible par rapport aux antennes droites dipolaires [34], [41], [42], [52], [53]. On peut en conclure que la structure effilée n'est pas la meilleure stratégie pour atteindre de meilleures performances.

Dans cette thèse, il est montré, à la fois théoriquement et expérimentalement, qu’une amélioration du champ proche peut être obtenue en effilant soigneusement les NAs bowtie. En fait, en choisissant les valeurs correctes pour l'angle de conicité, il est possible d'optimiser le compromis entre les pertes radiatives et les pertes non radiatives, permettant ainsi une nette amélioration des performances globales de l'antenne. La stratégie de l'angle de conicité adoptée ne comporte qu'une modification géométrique partielle. En particulier, les caractéristiques de gap restent inchangées, offrant ainsi une grande liberté au concepteur d'antenne en fonction de ses priorités expérimentales, tout en améliorant la mise en valeur du champ et le volume de mode (le volume contenant le champ localisé à l'intérieur de l'espace entre les bowtie) produites par les NAs. Dans un premier temps, on montrera ici comment une telle amélioration affecte les performances des antennes dans le régime THz, mais cela sera également présenté comme une stratégie efficace dans la gamme de fréquences IR. Ensuite, nos résultats seront également montrés ici améliorer de manière prometteuse les résultats de l'expérience de couplage fort réalisée précédemment avec une antenne directe non optimisée [32]. Enfin, grâce à l'effet de réduction de perte de la stratégie de réduction progressive, il sera démontré qu'il est possible d'utiliser des matériaux alternatifs pour la fabrication de NA. En fait, il a été démontré que le matériau semi-conducteur oxyde d’étain-indium (ITO), généralement trop dommageable pour la fabrication de NA, résonne dans le régime THz en raison de la stratégie de l'angle de conicité. Les NAs de l'ITO ont d'énormes potentialités dans, par exemple, le régime non

linéaire en tant que matériau alternatif à l'or, qui fond habituellement au cours d'expériences non linéaires en raison des hautes énergies impliquées.

2 Nanoantennes Plasmoniques[3]

Les nanoantennes plasmoniques sont des dispositifs capables de localiser la lumière à propagation libre dans un volume inférieur à la longueur d'onde. Grâce à cette propriété, la limite de diffraction n'empêche plus la longue onde THz d'interagir avec le nano-objet. Les NAs se comportent différemment des antennes habituelles et leur étude a été réalisée à l'aide du modèle Fabry-Perot. En supposant un NA parfaitement cylindrique en métal et entouré d'un diélectrique, un tel modèle considère les extrémités de NA comme deux miroirs semi-transparents caractérisés par leur coefficient de réflexion. Ceci permet de calculer le champ proche aux extrémités de NA comme

$$E_{\text{tip}} = E_0 \frac{\left(1 - Re^{2j\phi}\right)\left(1 - e^{2j\phi}\right)}{1 - R^2 e^{4j\phi}},$$

avec amplitude de champ électrique externe de référence E_0, coefficient de réflexion R aux

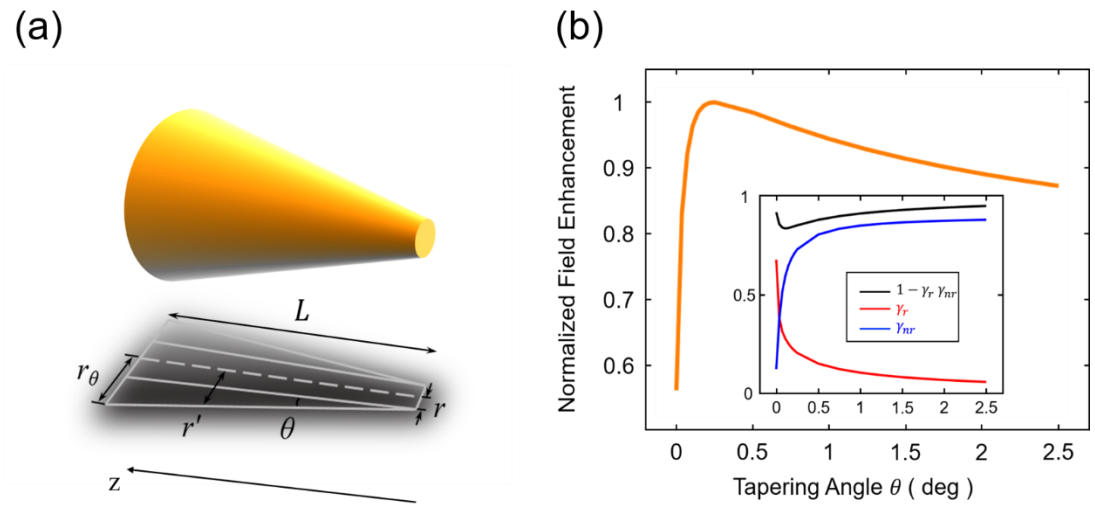

Figure S.7.1 (a) Schéma du cône tronqué, avec une longueur d'antenne L, un angle de conicité θ, un rayon r de la petite extrémité fixe, un rayon r_θ de la plus grande extrémité et un $r' = r + z' tan(\theta)$ est le rayon à la coordonnée arbitraire z'. (b) Rehaussement normalisé du champ proche pour un cône tronqué en or de $100\ \mu m$ de long, avec un rayon de $r = 50\ nm$ de la pointe la plus petite et un angle de conicité θ compris entre $0°$ et $2,5°$. Le champ proche augmente initialement en augmentant l'angle de dépouille, atteignant un maximum. Pour des angles plus fins, le champ proche diminue. Encart: évolution du coefficient de puissance pour les pertes radiatives (rouge) et non radiatives (bleu); en noir, le comportement de perte de puissance totale révèle un minimum dans la perte totale due à un compromis optimal entre perte décroissante non radiative et perte radiative croissante.

[3] La discussion et les images de ce chapitre ont été modifiées à partir de l'article publié par V. Aglieri et al., "Improving nanoscale terahertz field localization by means of sharply tapered resonant nanoantennas," Nanophotonics, vol. 9, no. 3, pp. 683–690, Feb. 2020, doi: 10.1515/nanoph-2019-0459 [66]. Cet article est sous licence Attribution 4.0 International (CC BY 4.0).

extrémités de l'antenne et

$$\phi = \kappa_0 \, n_{\text{eff}} \, L,$$

déphasage accumulé par le mode oscillant sur l'antenne en alternance. Tirant parti de l'efficacité de ce modèle pour étudier une méthode permettant d'améliorer les performances de l'antenne, le même modèle a été appliqué aux cylindres coniques comme celui illustré à la **Figure S.7.1 (a)**. Dans ce cas, le champ à la pointe est calculé en considérant le coefficient de réflexion à la pointe la plus grande R_θ en fonction de l'angle de conicité θ, ainsi:

$$E_{\text{tip}} = E_0 \, \frac{\left(1 - Re^{2j\phi}\right)\left(1 - e^{2j\phi}\right)}{1 - RR_\theta e^{4j\phi}},$$

et la phase est calculée comme

$$\phi = \kappa_0 \int_0^L n_{\text{eff}}(z) \, dz.$$

La phase est obtenue par intégration car l'indice effectif ressenti par le mode oscillant n'est plus constant le long du cylindre effilé, mais est fonction de la valeur du rayon local $r' = r + z' \tan(\theta)$.

Les résultats pour un tronc de cône en or, de longueur $L = 100\,\mu\text{m}$ (résonnant ainsi autour de 1 THz), petit rayon fixe $r = 50\,\text{nm}$, avec fréquence plasma $f_p = 2080\,\text{THz}$ et durée de vie du porteur $\tau = 18\,\text{fs}$ [68], sont illustrés à la **Figure S.7.1 (b)** en fonction de l'angle de conicité θ. Dans ce cas, l'amélioration de champ augmente lorsque l'angle de conformation θ augmente jusqu'à ce qu'un maximum soit atteint, en correspondance de l'angle optimal θ_{opt}. Cependant, pour $\theta > \theta_{\text{opt}}$, l'amélioration de champ diminue. Ce comportement est dû au compromis entre diminution de la perte non radiative α_{nr} et augmentation de la perte radiative α_{r}. Dans l'encadré de la **Figure S.7.1 (b)** sont montrés les coefficients de puissance pour la perte non radiative γ_{nr} et radiative γ_{r}. Ces quantités sont liées aux pertes comme suit:

$$\alpha_{\text{nr}} = 1 - e^{-4\kappa_0 \int_0^L \text{Im}\{n_{\text{eff}}(z)\} dz} = 1 - \gamma_{\text{nr}},$$

$$\alpha_{\text{r}} = (1 - R^2)(1 - R_\theta^2) = 1 + R^2 + R_\theta^2 + \gamma_{\text{r}}.$$

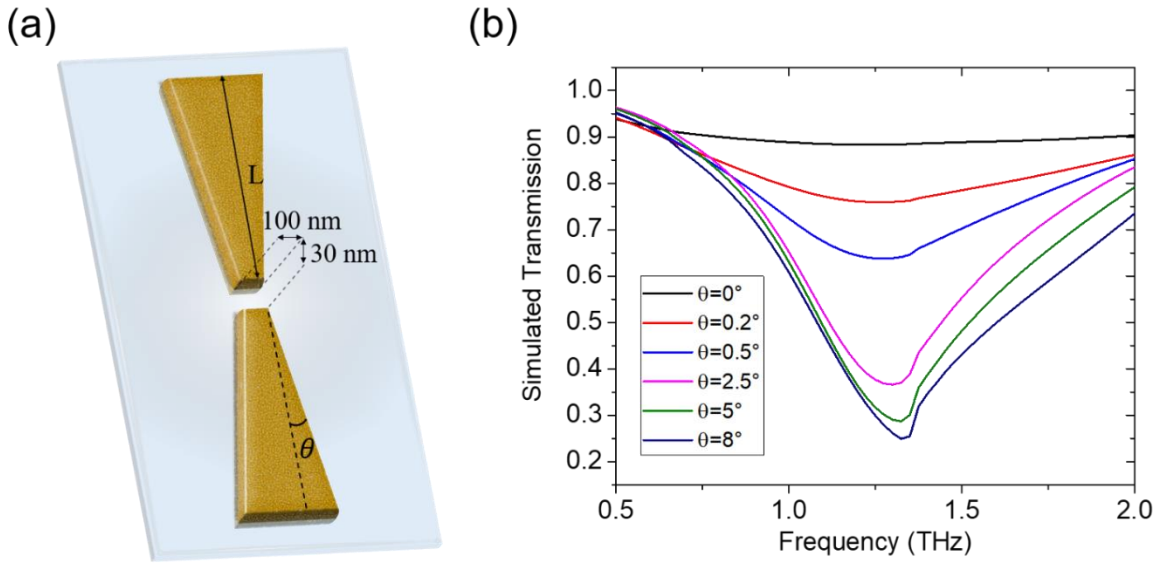

Figure S.7.2 (a) Esquisse de la paire NA sur le substrat de silicium. (b) Spectres de transmission simulés pour un nombre sélectionné d'angle d'atténuation. La transmission augmente parallèlement à l'angle d'atténuation en raison de la quantité plus importante de matériau absorbant le rayonnement entrant THz.

3 Conception, Fabrication et Caractérisation de Nanoantennes THz[4]

Grâce à l'évaluation qualitative de l'amélioration obtenue grâce à la stratégie de réduction progressive, il est maintenant possible de se lancer dans la fabrication et la caractérisation de NA résonant aux fréquences THz avec des performances améliorées dans une configuration plane plutôt que cylindrique. Premièrement, les NAs ont été conçus pour avoir une longueur de $45\ \mu\mathrm{m}$, une épaisseur de $60\ \mathrm{nm}$ et une largeur de $100\ \mathrm{nm}$ aux extrémités les plus petites (les deux extrémités dans le cas d'un angle décroissant $\theta = 0°$). De plus, les bowties appariés ont été pris en compte avec un intervalle de $30\ \mathrm{nm}$ de large, comme illustré à la **Figure S.7.2 (a)**. Les logiciels COMSOL Multiphysics a été utilisé pour simuler les NA THz sous éclairage THz en faisant varier l'angle de conicité θ entre $0°$ et $8°$. Les spectres de transmission sont illustrés à la **Figure S.7.2 (b)**. Le spectre de transmission diminue à mesure que l'angle de conicité θ augmente. Cela est dû à la plus grande surface de la paire de bowtie d'or NA pour les grands angles effilés. Le champ proche produit dans l'espace entre les deux bowtie est illustré sur la carte en 2D de la **Figure S.7.3 (a)**. On peut voir que dans le cas d'une antenne dipolaire droite ($\theta = 0°$), le champ proche ne présente aucune résonance dans la plage de fréquences à l'étude. Ceci est dû à la très grande perte non radiative qui caractérise les NA en or avec un rapport de forme de $AS \approx 450$. En

[4] La discussion et les images de ce chapitre ont été modifiées à partir de l'article publié par V. Aglieri et al., "Improving nanoscale terahertz field localization by means of sharply tapered resonant nanoantennas," Nanophotonics, vol. 9, no. 3, pp. 683–690, Feb. 2020, doi: 10.1515/nanoph-2019-0459 [66]. Cet article est sous licence Attribution 4.0 International (CC BY 4.0).

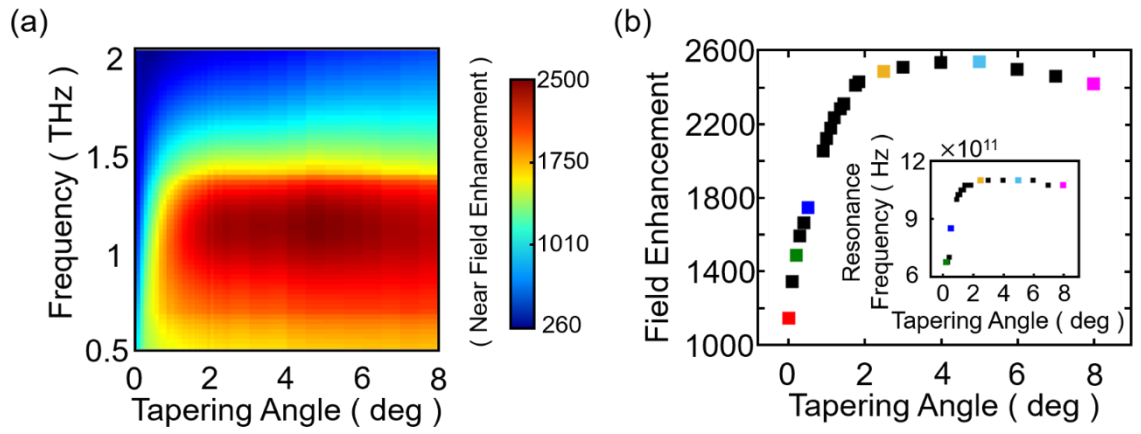

Figure S.7.3 (a) Carte 2D d'amélioration du champ proche en fonction de l'angle et de la fréquence de réduction. (b) Pic d'amélioration de champ en fonction de la fréquence. Dans l'encart, la fréquence de résonance des bowties NAs varie en fonction de l'angle conicité.

particulier, le couple de NA bowtie se comporte comme un “paratonnerre”, caractérisé par une résonance large bande avec une mise en valeur de champ mauvaise.

Cependant, en augmentant l'angle à $0{,}2°$, une résonance apparaît et la valeur du champ proche augmente. Une augmentation supplémentaire de l'angle de conicité entraîne une augmentation de l'amélioration du champ jusqu'à ce qu'un maximum soit atteint en correspondance de l'angle optimal θ_{opt}, celui pour la paire de NAs d'or s'est avéré être $\theta_{\mathrm{opt}} = 4 - 5°$. Pour des angles plus grands, le champ proche diminue. La **Figure S.7.3 (b)** montre les pics d’amélioration de champ en fonction de l’angle de conicité: l’amélioration maximale du champ proche (pour $\theta = \theta_{\mathrm{opt}}$) est environ 2,2 fois supérieure à l’amélioration obtenue du couple d’aides linéaires droites et environ 1,7 fois supérieure à le premier couple NA de bowties résonants à $\theta = 0{,}2°$. Ainsi, la stratégie de réduction progressive est confirmée expérimentalement et s'avère être une stratégie efficace pour améliorer les

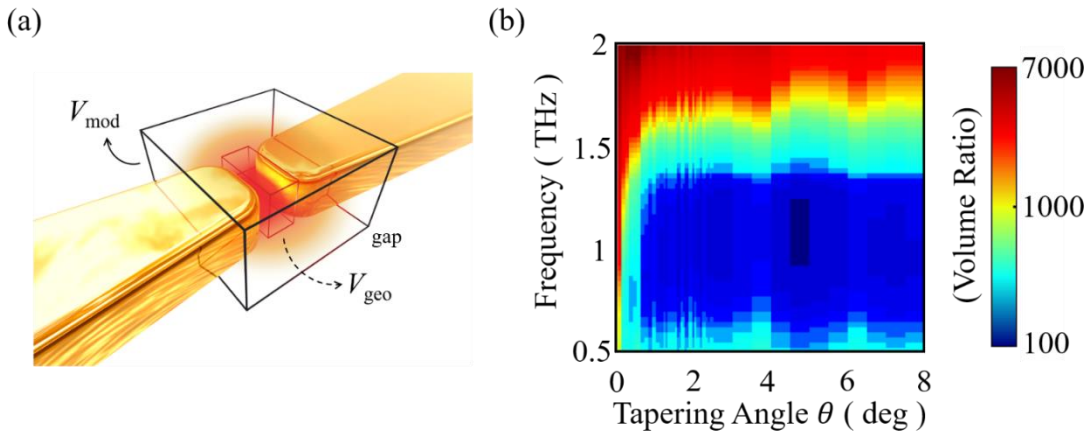

Figure S.7.4 (a) Volume de mode V_{mod} et volume géométrique de l'écart V_{geo}^{gap}, représenté dans l'esquisse de l'écart entre les NAs. (b) Carte 2D du rapport de volume en fonction de l'angle de conicité et de la fréquence.

performances des NA.

Outre l'amélioration du champ, la deuxième amélioration importante consiste en la diminution du volume du mode. La **Figure S.7.4 (a)** représente un schéma du volume de mode V_{mod} et du volume géométrique de l'intervalle $V_{\mathrm{geo}}^{\mathrm{gap}}$ (c'est-à-dire 30×60×100 nm). La **Figure S.7.4 (b)** présente une carte 2D du rapport de volume $V_{\mathrm{ratio}} = V_{\mathrm{mod}}/V_{\mathrm{geo}}^{\mathrm{gap}}$ en fonction de l'angle de conicité et de la fréquence de résonance. La carte révèle une réduction du rapport de volume de 7 fois par rapport à une antenne dipolaire droite, avec un volume en mode légèrement supérieur à 100 fois le volume géométrique $V_{\mathrm{geo}}^{\mathrm{gap}}$. C'est un résultat vraiment impressionnant si l'on considère que le $V_{\mathrm{geo}}^{\mathrm{tot}}$ des NA est énorme comparé à l'écart de $V_{\mathrm{geo}}^{\mathrm{gap}}$ (variant entre 3000 (pour les NA avec $\theta = 0°$) à ~190000 (pour les NA avec $\theta = 8°$) fois le $V_{\mathrm{geo}}^{\mathrm{gap}}$).

Les processus de fabrication ont été réalisés dans les salles blanches de l'Istituto Italiano di Tecnologia (Gênes, Italie). À partir des résultats de la simulation, cinq échantillons ont été choisis pour la validation expérimentale de la stratégie de réduction progressive, c'est-à-dire des paires de bowtie d'or avec angle de réduction: $0, 0{,}2, 0{,}5, 2{,}5$ et $8°$, Substrat en silicium de 500 µm d'épaisseur caractérisé par une résistivité élevée ($10000\ \Omega \cdot \mathrm{cm}$). Le matériel et l'équipement principaux utilisés pour la fabrication des NAs de bowtie d'or sont:

- Résine électronique, aluminium, or et titane,
- Spin Coater,
- Système de dépôt physique en phase vapeur,
- Système de dépôt physique en phase vapeur à faisceau d'électrons,
- Lithographie par faisceau d'électrons.

Les étapes du flux de processus suivies pour cette fabrication sont résumées à la **Figure S.7.5**. Le processus commence par la coupe d'une tranche de silicium en substrats de $1 \times 1\ \mathrm{cm}^2$ et en par le nettoyage à ultrasons dans de l'acétone, de l'alcool isopropylique (IPA) et de l'eau hautement purifiée (obtenue à partir d'un système Milli-Q®). Ensuite, les substrats ont subi un traitement final au plasma d'oxygène pour éliminer les impuretés restantes sur la surface du substrat.

La résine électronique PMMA A4 2:1 (2 parties de PMMA A4 et 1 partie d'Anisole) a été enduite par centrifugation à l'aide du système de centrifugation à 1800 rpm/min pendant 1 minute. Ensuite, l'échantillon est cuit à $180°$ pendant 7 minutes (**Figure S.7.5 (a)**) pour évaporer le solvant liquide restant. Sur le résine électronique, on dépose une fine couche d'aluminium par dépôt en phase vapeur (**Figure S.7.5 (b)**) nécessaire pour éviter un effet de charge dû au caractère isolant du substrat de silicium utilisé.

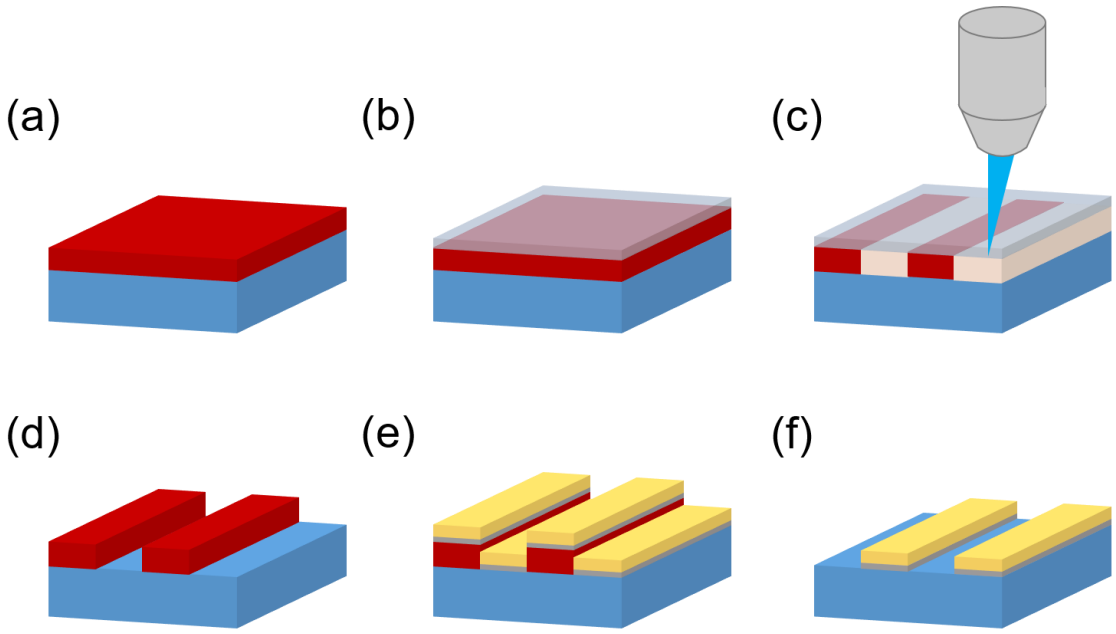

Figure S.7.5 Étapes du flux de processus utilisées lors de la fabrication des NA appariées. (a) Un substrat de silicium est nettoyé et préparé pour la lithographie en déposant une couche de PMMA. (b) Sur la résine électronique est déposé un film mince d'aluminium pour éviter les problèmes de charge pendant l'étape de lithographie. (c) La couche de PMMA est lithographiée à l'aide du système de lithographie E-Beam. (d) Le film d'aluminium est retiré et la couche de PMMA est développée en obtenant le masque souhaité. (e) Une couche d'adhésion de titane et un film d'or sont déposés sur le masque. (f) Le masque est retiré et les structures en or sont obtenues.

Une fois la couche conductrice en aluminium déposée, l'échantillon est chargé à l'intérieur du système de lithographie à faisceau d'électrons Raith 150-two. Ici, grâce à la résolution extrêmement élevée du système, des fonctionnalités aussi petites que 7 nm sont réalisables. La lithographie a été réalisée avec des paramètres de haute résolution, requis par les petites caractéristiques de l'espace. Le faisceau était réglé pour délivrer $500 \mu C/cm^2$ à $20\ keV$, avec une ouverture de $10\ \mu m$ et une taille de champ d'écriture de $100 \times 100\ \mu m^2$ (**Figure S.7.5 (c)**). Après la lithographie, la couche d'aluminium est éliminée dans de l'hydroxyde de potassium (KOH) à 1 molaire (de l'eau hautement purifiée a été utilisée comme étape d'arrêt pour la gravure au KOH). Après la lithographie, la couche d'aluminium est éliminée dans de l'hydroxyde de potassium (KOH) à 1 molaire (de l'eau hautement purifiée a été utilisée comme étape d'arrêt pour la gravure au KOH). Ensuite, la résine électronique est développée en MIBK/IPA 1:3 (**Figure S.7.5 (d)**).

L'échantillon a été recouvert d'une couche d'adhésion de titane de $5\ nm$, puis d'un film d'or de $60\ nm$ d'épaisseur par dépôt en phase vapeur à faisceau d'électrons (**Figure S.7.5 (e)**). Ensuite, la résine électronique a été soulevée dans de l'acétone chaud à $120°C$ et finalement nettoyée avec un traitement au plasma à l'oxygène (**Figure S.7.5 (f)**). Le résultat final est illustré par des images au microscope électronique à balayage (MEB) de la **Figure S.7.6**: l'image principale montre les NA de bowtie en or fabriqués au-dessus d'un substrat de silicium sur une surface totale de $5 \times 5\ mm^2$ de large. La partie supérieure de l'encadré

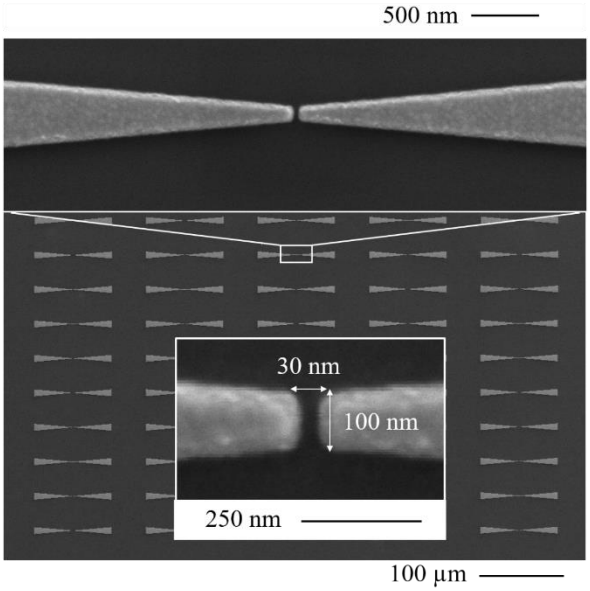

Figure S.7.6 Image au MEB d'une partie de l'échantillon de $5 \times 5\ mm^2$ recouverte des bowties en or dont l'angle est effilé $\theta = 5°$. La partie supérieure de l'encadré montre une image de NA proche de l'écart. La partie inférieure de l'encadré montre une image à fort grossissement de l'écart entre 30 nm de large et 100 nm de hauteur entre les bowties.

montre une vue rapprochée des bowties près de l'écart et la vue du bas un grossissement élevé de l'écart entre les NA mettant en évidence les caractéristiques de l'écart.

4 Caractérisation expérimentale dans le régime THz[5]

Les caractérisations expérimentales ont été effectuées en mode de transmission en utilisant la technique de spectroscopie dans le domaine temporel THz au laboratoire de spectroscopie THz et IR de l'INRS-EMT (Varennes, Québec). Les spectres de transmission ont été récupérés en normalisant les spectres des matrices des NAs par rapport aux spectres de transmission du substrat de silicium nu, afin d'éliminer toute influence possible de ce dernier. Les résultats pour les bowties en or, $\theta = 0; 0{,}2; 0{,}5; 2{,}5\ et\ 5°$ sont présentés à la **Figure S.7.7**. Le couple des NAs dipolaires droits ($\theta = 0°$) ne présente aucune résonance, principalement en raison des pertes très élevées caractérisant ce cas. Au lieu de cela, en partant de la paire bowtie à $\theta = 0{,}2°$, une résonance apparaît à 1,24 THz. En augmentant l'angle de conicité, la transmission subit une diminution, principalement en raison de la plus grande surface de l'antenne avec un angle de plus en plus grand, ce qui entraîne une absorption plus élevée du rayonnement et donc une moindre transmission du signal THz.

[5] La discussion et les images de ce chapitre ont été modifiées à partir de l'article publié par V. Aglieri et al., "Improving nanoscale terahertz field localization by means of sharply tapered resonant nanoantennas," Nanophotonics, vol. 9, no. 3, pp. 683–690, Feb. 2020, doi: 10.1515/nanoph-2019-0459 [66]. Cet article est sous licence Attribution 4.0 International (CC BY 4.0).

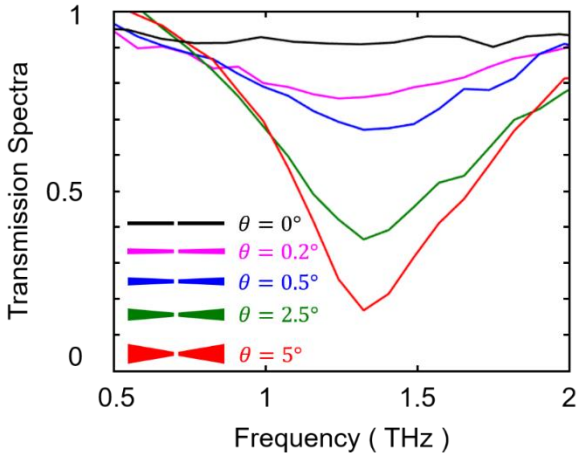

Figure S.7.7 Spectres de transmission expérimentaux obtenus par caractérisation THz-TDS de bowties en or. Le minimum de transmission diminue avec l'augmentation de l'angle de conicité, en raison de la plus grande surface en or absorbant le rayonnement THz entrant.

THz-TDS est une technique utile pour récupérer des informations dans le domaine THz. Cependant, il ne donne que des informations de champ lointain sur l'échantillon à l'étude. Par conséquent, il n'est pas possible de récupérer des informations sur le comportement en champ proche des NAs fabriquées. Afin de comparer la caractérisation expérimentale aux résultats de la simulation, il est important de récupérer les valeurs de largeur totale à mi-

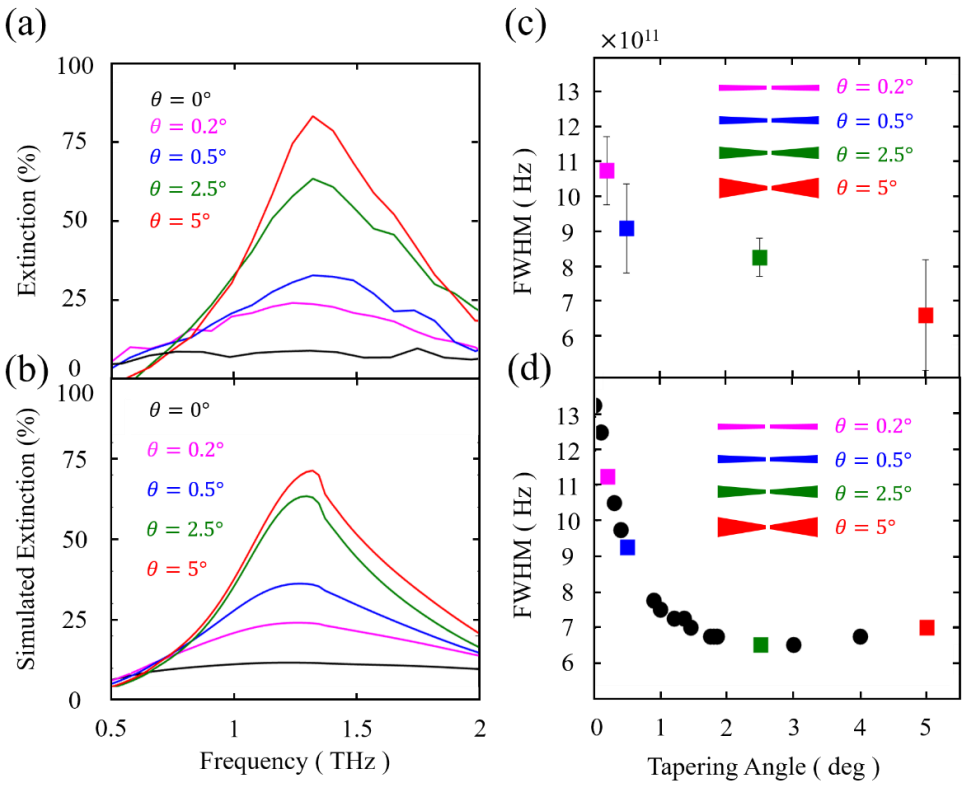

Figure S.7.8 Spectre d'extinction simulés et expérimentals, respectivement. (c)-(d) Valeurs FWHM obtenues à partir des spectres d'extinction: les carrés colorés correspondent à l'échantillon fabriqué avec $\theta = 0.2, 0.5, 2.5\ et\ 5°$. La configuration $\theta = 0°$ n'a pas été prise en compte car il n'a pas été possible de récupérer une valeur FWHM significative.

maximum (FWHM) des spectres expérimentals et simulés. En effet, la FWHM est directement proportionnelle à la perte totale du système, c'est-à-dire aux pertes radiatives α_{r} et non radiatives α_{nr}, et peut donc être utilement utilisée pour évaluer la perte des antennes fabriquées. Les **Figure S.7.8 (a)-(b)** montrent les spectres d'extinction, définis comme 1-T, avec le spectre de transmission T, des résultats expérimentaux et simulés, respectivement. Les deux spectres sont très similaires et présentent le même comportement en faisant varier l'angle de conicité. Les **Figure S.7.8 (c)-(d)** montrent les valeurs de FWHM obtenues à partir des spectres d'extinction expérimental et de simulation, respectivement. Comme on peut le constater, il existe un bon accord sur le comportement des pertes. En fait, dans le cas expérimental, une réduction de la FWHM se produit alors que l'angle d'atténuation est augmenté, ce qui révèle une réduction de la perte totale des NA. Après de tels résultats, on peut affirmer que la prédiction du modèle quasi-analytique et la réponse des structures simulées sont confirmées expérimentalement.

Une fois obtenue la validation expérimentale de l'effet bénéfique de la stratégie de réduction progressive, cette méthode a été appliquée aux antennes de navette ITO de conception et aux NA d'or pour les expériences de couplage fort, illustrées ci-après.

5 Applications

5.1 Nanoantennes de ITO

Nous exploitons également la stratégie de réduction progressive pour la fabrication d'antennes-navettes en oxyde d'étain-indium (ITO). L'ITO est un matériau prometteur pour

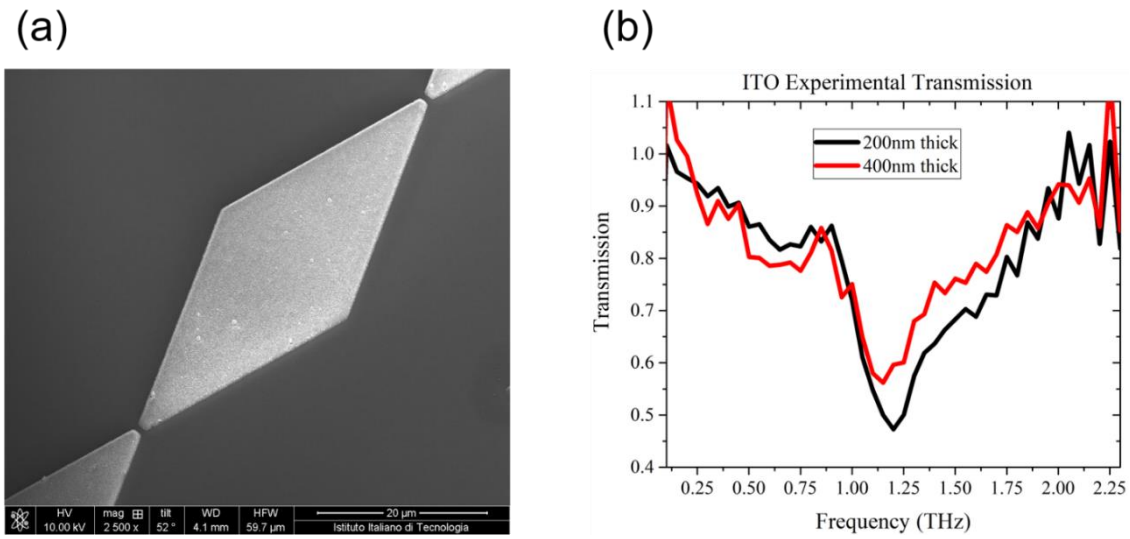

Figure S.7.9 (a) Antenne shuttle de ITO dans une image MEB. La largeur de l'intervalle entre les antennes est de $1 \times 1\ \mu m^2$. (b) Spectres de transmission THz des antennes shuttle de ITO épaisses de 200 nm (ligne continue noire) et de 400 nm (ligne continue rouge). Une résonance claire se produit entre 1 et 1,25 THz pour les deux échantillons.

la fabrication d'antennes plasmoniques en raison de sa robustesse par rapport aux autres matériaux couramment utilisés pour la plasmonique. Cette propriété fait de l'ITO un bon substitut de l'or pour la fabrication d'une antenne plasmonique pour les expériences non linéaires. En fait, il est bien connu que l'antenne en or fond lors d'expériences non linéaires en raison du très haut pouvoir d'excitation impliqué. Cependant, l'ITO se caractérise par une concentration de porteurs de charge beaucoup plus faible et, même correctement dopé, il n'est pas possible d'atteindre la même concentration en porteurs d'or [39]. Néanmoins, la stratégie de réduction progressive était déjà appliquée avec succès aux antennes de navette ITO et une résonance se produit dans le régime THz. La **Figure S.7.9 (a)** présente une image au MEB d'un échantillon fabriqué d'antennes de navette ITO. Les antennes de navette résultent de la fusion des paires de bowties uniques observées pour le cas NA. L'angle de conicité optimal a été calculé par simulation à l'aide du logiciel CST Studio Suite. Les résultats de la spectroscopie expérimentale de transmission THz sont présentés à la **Figure S.7.9 (b)**, pour deux échantillons de navette ITO, caractérisés par des antennes navette ITO de 200 nm (ligne noire) et de 400 nm (ligne rouge). Comme on peut le constater, même si l'ITO souffre toujours de pertes très élevées, une résonance se produit entre 1 et 1,25 THz grâce à l'optimisation de la structure. À l'avenir, une caractérisation non linéaire de l'antenne ITO sera réalisée pour démontrer enfin son utilité dans les expériences non linéaires, pour deux échantillons de navette ITO, caractérisés par des antennes navette ITO de 200 nm (ligne noire) et de 400 nm (ligne rouge). Comme on peut le constater, même si l'ITO souffre toujours de pertes très élevées, une résonance se produit entre 1 et 1,25 THz grâce à l'optimisation de la structure. À l'avenir, une caractérisation non linéaire de l'antenne ITO sera réalisée pour démontrer enfin son utilité dans les expériences non linéaires.

5.2 Nanoantennes Moon

Une fois validée, la stratégie de réduction progressive a été appliquée aux expériences de couplage fort. Dans les travaux de Jin et al [32], il est présenté le fort couplage entre le mode de surface des NAs d'or et le mode de phonons des nano-cristaux de CdS dans l'espace entre les ‘‘gap’’. Les NAs utilisés ont été conçus sous forme de chaîne d'antennes droites.

La stratégie des antennes coniques a été utilisée pour améliorer les performances de l'antenne et pour extraire plus d'informations des expériences de couplage fort conduites dans [32]. Dans ce cas, l'antenne utilisée est appelée *antenne moon*. Elle est illustrée à la **Figure S.7.10 (a)**. La stratégie a été appliquée en modifiant la longueur $W2$ et en laissant inchangées les fonctions d'espacement. L'image MEB de l'échantillon fabriqué est reportée

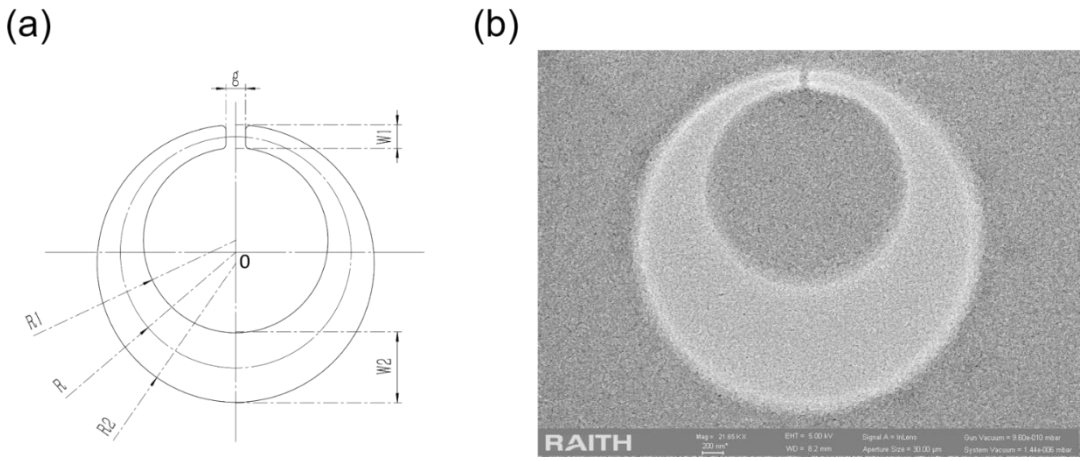

Figure S.7.10 (a) NA en forme de lune (antenne moon) pour un schéma de couplage fort en vibration. Le paramètre g est la largeur de l'écart, $W1$ la hauteur de l'écart, $W2$ le paramètre de conicité, R, $R1$ et $R2$ sont le rayon des circonférences centrale, interne et externe, respectivement. (b) Images au MEB d'une antenne moon fabriquée après le dépôt des couches de nanocristaux CdS.

à la **Figure S.7.10 (b)**. Les résultats obtenus grâce aux mesures sont actuellement à l'étude. Cependant, il a déjà été constaté une réponse plus nette des moon antennes, qui se traduit par un couplage plus fort, puis par une empreinte digitale forte du couplage THz-nanocristal dans la région du gap.

5.3 Nanoantennes IR

Une autre application intéressante de cette stratégie est son utilisation dans une autre

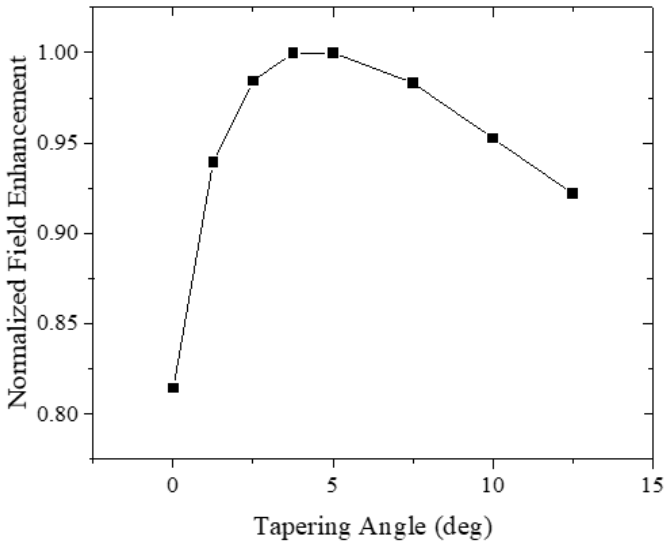

Figure S.7.11 Les pics d'amélioration du champ proche en fonction de l'angle de conicité θ. L'antenne a une longueur de 2 µm, une épaisseur de 40 nm et une largeur de 50 nm. La fréquence de résonance se situe autour de λ = 6.6 µm.

gamme de fréquences. En fait, cette méthode a pu être appliquée au régime IR, comme le montre la **Figure S.7.11**, où la simulation de l'amélioration du champ proche en fonction de l'angle a également révélé une amélioration des performances de l'antenne.

6 Conclusion et Perspectives

La gamme de fréquences THz a été largement explorée en raison de ses applications prometteuses dans de nombreux domaines de la recherche et de l'industrie. Le soi-disant «THz-gap» en est encore au stade de la transition, mais des étapes très importantes ont déjà été franchies pour le combler complètement. Le premier coup de pouce important provient de l'amélioration et de l'optimisation des sources et des détecteurs qui permettent aujourd'hui une génération et une détection de THz abordables, durables et précises. Ainsi, l'intérêt pour l'utilisation des ondes THz s'est répandu de sorte que la technologie de communication rapide, la détection et l'imagerie non destructives, ainsi que le contrôle des processus industriels ne sont que quelques exemples d'applications dans lesquelles des champs THz sont impliqués.

La spectroscopie est l'un des domaines d'application les plus intéressants, principalement parce que de nombreuses excitations élémentaires de la matière se situent dans cette gamme de fréquences. Dans le passé, les scientifiques devaient faire face à la caractéristique de faible sensibilité intrinsèque des ondes THz lors de la détection de petits objets, en raison de la longueur d'onde relativement longue associée à cette gamme de fréquences. Initialement, la spectroscopie THz était limitée à l'étude de matériaux en vrac ou de gros agrégats de nanoparticules. Cependant, la sensibilité au THz s'est améliorée au fil des ans. Premièrement, il a été démontré que les guides d'ondes métalliques supportaient la spectroscopie THz grâce à une sensibilité améliorée, mais le spécimen étudié devait être déposé sur l'ensemble de la plate-forme de détection du guide d'onde afin d'exploiter l'amélioration de la sensibilité. Ensuite, il a été démontré que les métamatériaux et les métasurfaces pouvaient détecter de très petites quantités de matériaux en évaluant le changement d'indice de réfraction. Malheureusement, même si le changement d'indice de réfraction est appréciable en présence aussi d'une seule particule proche de ces structures, il ne donne aucune information spectrale sur le spécimen étudié. Même résultat pour les nanoslots les plus récents configurés dans une couche métallique qui exploite les valeurs de champ élevé accumulées à l'intérieur de telles structures. Ces appareils sont capables de détecter la présence de quelques nanogrammes de sucre grâce à une modification du signal transmis par rapport aux nano-slots nus, et ils sont même capables de discriminer différents types de sucres. Cependant, aucune information spectroscopique ne peut être obtenue.

Au cours des dernières décennies, un effet physique particulier a été utilisé pour améliorer les techniques spectroscopiques courantes, à savoir l'effet d'amélioration de la surface. Grâce à l'utilisation de surfaces ondulées et de nanoparticules, il est possible de capturer et de localiser de la lumière à propagation libre dans des volumes inférieurs à la longueur d'onde, obtenant ainsi un champ très concentré. La spectroscopie Raman et l'absorption infrarouge sont deux techniques qui tirent grand parti des effets d'amélioration de surface, car elles sont très sensibles à l'amplitude du champ local. Ainsi, grâce aux valeurs de champ élevées produites par l'effet d'amélioration de surface, il est possible d'améliorer considérablement la spectroscopie traditionnelle. En exploitant de telles avancées, Razzari et al. [30] d'abord, puis Toma et al. [31] ont ensuite démontré l'applicabilité du concept d'amélioration de surface à la spectroscopie THz en utilisant des NAs THz. Ils ont conçu des NAs capables de localiser la lumière aux extrémités d'antennes de taille inférieure à la longueur d'onde, où l'intensité du champ électrique local atteint des valeurs extrêmement élevées. Grâce à cette amélioration du champ, il est possible de récupérer des informations spectroscopiques de nano-matière à proximité immédiate des extrémités de NA (où le champ électrique est localisé) grâce au coefficient d'absorption amélioré de la nano-matière en interaction avec le champ localisé THz. De tels résultats impliquent énormément l'utilisation des ondes THz, non seulement pour la spectroscopie, mais également, par exemple, dans les études d'interaction THz lumière-matière. En effet, Xin et al. [32] en employant la technique de localisation de champ dans la gamme THz qui vient d'être exposée, a démontré la possibilité non seulement de récupérer des informations spectroscopiques de nanocristaux, mais également de modifier et de remodeler leur résonance phononique, c'est-à-dire que les ondes THz, lorsqu'elles sont extrêmement localisées, peuvent également modifier la propriétés matérielles.

Des avancées aussi importantes nécessitent une étude continue et approfondie pour obtenir des meilleures performances des NAs. En fait, les pertes matérielles tant que les pertes de rayonnement affectent les propriétés de la NA, limitant ainsi le potentiel des études d'interaction lumière-matière assistées par THz. Ainsi, mon travail de doctorat à porté à l'étude, à la simulation, à la conception et à la fabrication des NAs THz plasmoniques en vue de l'amélioration des performances, du champ proche et du volume de mode produit par les NAs. Premièrement, un modèle quasi analytique simplifié a été mis au point, montrant que l'amélioration du champ proche et le volume de mode d'une NA en or de forme cylindrique peuvent être efficacement améliorés si la NA est effilée de manière optimale. En fait, en augmentant l'angle de conicité, une amélioration initiale est obtenue jusqu'à atteindre une valeur maximale, mais des angles trop grands entraînent plutôt une diminution des performances de la NA. Une telle amélioration naît de compromis entre une perte non

radiative plus faible et une perte radiative plus élevée en faisant varier l'angle de diminution. Ce comportement a été reproduit par une activité de simulation FEM intensive afin de récupérer des informations quantitatives pour une conception d'antenne précise pour des bowties couplés en or. En particulier, il a été trouvé un rehaussement du champ proche environ 2,2 fois supérieur et un volume de mode réduit de 7 fois à l'intérieur de l'intervalle lorsque les NAs bowties couplés en sont effilées de manière optimale par rapport à une antenne dipolaire droite, ce qui présente une réponse suramortie. Ensuite, il a été choisi de fabriquer cinq échantillons avec un angle d'atténuation à 0, 0,2, 0,5, 2,5 et 5° afin de montrer de manière expérimentale l'amélioration de la performance des NAs en fonction de l'angle de conicité. Une fois fabriqués, les échantillons ont été caractérisés en utilisant une technique THz-TDS. Le FWHM a été calculé à partir des spectres de transmission afin de récupérer les informations relatives au comportement de perte totale lors de la variation de l'angle de conicité. La FWHM de la caractérisation expérimentale décroît avec l'augmentation de l'angle de conicité, confirmant enfin l'amélioration des performances des NAs, prévue à la fois par modèle quasi-analytique et par simulation FEM. Ces découvertes ouvrent de nouvelles voies pour le développement de la technologie THz d'interaction lumière-matière à l'échelle nanométrique et pour toutes ces applications qui reposent sur des valeurs élevées d'amélioration de champ proche et de localisation de champ sous-onde d'onde, telles que la détection et le régime de couplage fort études.

Dans le cadre des développements futurs, nous travaillons actuellement sur les antennes en forme de lune (moon antenne) présentées dans le dernier chapitre. Autres caractérisations seront effectuées sur des antennes en forme de lune pour récupérer des informations sur la réponse locale des nanocristaux dans l'espace en termes d'amélioration du champ.

APPENDIX

1 The Clean Room environment and equipment

1.1 Clean Room Environment

The Clean Room is a laboratory where temperature, pressure and humidity are controlled to maintain constant the properties of the materials and chemicals used during the fabrication processes. Further, illumination is set on specific wavelengths to avoid accidental photoresist exposure.

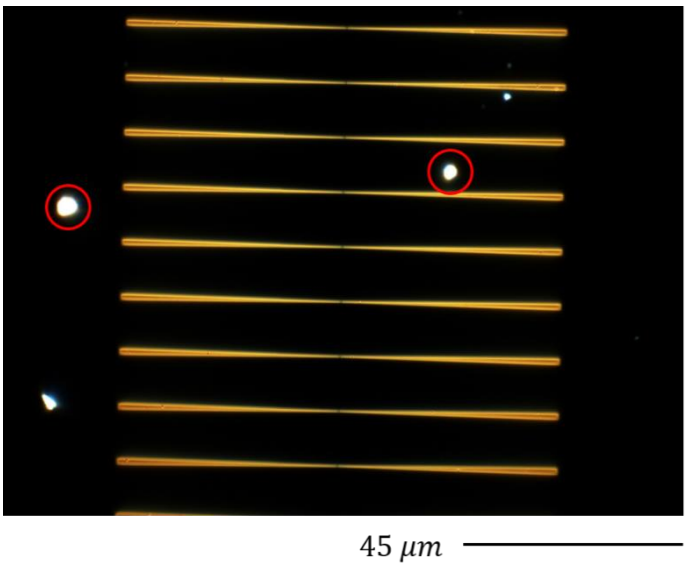

Figure A.7.12 Dark field optical microscope image of gold bow-tie NAs. The red circles contain dust particles with diameter slightly less then tens of microns. At the center of the bow-tie pairs the 30-nm-wide and 100-nm-height gap, thus with much smaller features than the ones characterizing dust particles.

The fabrication process has been performed in the class 10.000 and class 1.000 rooms of the Clean Room, where it is implemented a strict dust particle concentration control. This control is maintained through a continuously purified air flux obtained through the use of special filters designed to block particles of different sizes. To avoid contamination from the outside environment, the air pressure inside the Clean Room is set higher than the atmospheric pressure. Moreover, in order to avoid contamination from humans, all the Clean room users wear special overall suites capable to avoid the contamination due to dust particles attached to their garments and skin and coming from their breath.

Contamination control is of crucial importance to avoid the contamination of sample obtained through micro- and nano-fabrication techniques. Generally, the diameter of a generic dust particle is around hundreds of nanometers up to tens of microns, i.e. larger than the features of nano-devices. As an example, **Figure A.7.12** shows a dark field optical microscope image

of a sample covered with gold bow-tie pairs and some dust particles (highlighted by red circles) with a diameter of few micrometers. The particle contamination has been due to the exposure at external environment. By looking at the particle size, it becomes obvious that the gap in the center of the antenna pairs (that is, $30\times60\times100$ nm) can be completely filled with dust if a particle fall close to it. Further, the dust is usually electrically conductive, thus capable to short-circuit the two antennas and then making the sample useless.

1.2 Electronic Resist

The fundamental element of lithography is the *photoresist* or *electron-resist*. It consists of polymeric chains dissolved in a liquid solvent that can be deposited on top of substrates by spin-coating. Its main property is the ability to form a mask with micro- and nano-metric features patterned by the help of photon or electron beam lithography systems. The resist can be either positive or negative. In the first case, polymer chain bonds are broken as a consequence of photon/electron beam exposure, leading to a local decrease of the molecular weight. This allows to remove with high selectivity only the exposed resist in suitable developers, finally obtaining the desired pattern transferred onto the resist film [115]. In the second case, the opposite effect is obtained: the chains are tightly bounded as a consequence of an photon/electron beam exposure. Thus, if soaked in the developer, the non-impressed resist will be removed [116].

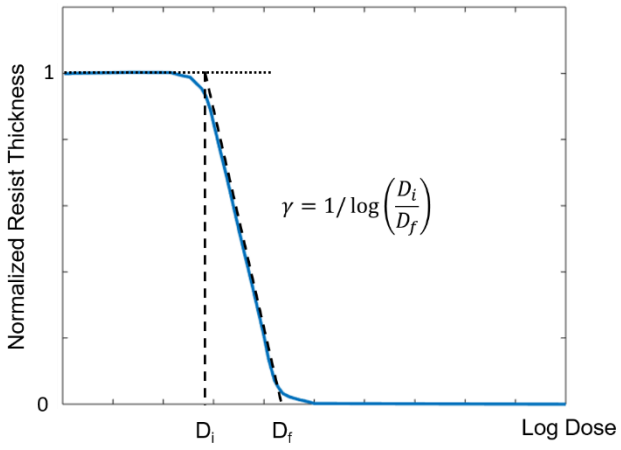

Figure A.7.13 Normalized resist thickness as a function of the received dose (in logarithmic scale) after the development. The slope γ of the curve is not perfectly vertical as it should be in an ideal situation. The slope value, the contrast γ, helps in the choice of the resist depending on the feature size of the desired pattern: the higher the absolute value of γ, the higher the contrast.

One of the most important parameter in the development of exposed resist is the ability of the developer to distinguish between exposed and non-exposed resist, that is, the selectivity. **Figure A.7.13** shows the normalized profile of a developed resist film after e-beam exposure: close to the origin the resist has not been exposed and remains intact (thickness equals 1), while far from the origin the resist has instead been exposed with increasingly

higher electron dose ($\mu C/cm^2$) and the film is completely removed (thickness equals 0). Ideally, the curve traced in the graph of **Figure A.7.13** should be perfectly vertical at the border between removed and unremoved resist. In an actual situation, the curve is not perfectly vertical and the slope can be calculated as

$$\gamma = \frac{1}{\log\left(\frac{D_i}{D_f}\right)}, \tag{7.1}$$

where D_i and D_f are the electron doses, calculated at the intersection between the line with the same angle of the steepest part of the slope (oblique dashed line) and its maximum (dotted horizontal line where thickness equals one) and at the intersection of its minimum (Log Dose axis where thickness equals zero), respectively. The parameter γ is called *contrast*, and its finite value (non perfectly vertical) is mainly due to the proximity effect over the resist film during the lithography (more on this issue will be discussed in Section (1.5)) [115].

Thus, it is not possible to obtain an infinite contrast, and the precision of the edges between removed and unremoved resist can greatly affect the quality of the result. It is then important to choose the resist that presents sufficiently high contrast relatively to the desired features. Taking into account the nanometric geometry of the NAs designed in this work, the electronic resist chosen is Poly(methyl methacrylate) (PMMA) dissolved in Anisole, a positive tone resist characterized by very high contrast when developed in methyl isobutyl ketone (MIBK), thus suitable for the nanometric resolution lithography.

1.3 Spin-coating Deposition System

Spin-coating is a deposition technique used when a material dissolved in liquid solvents have to be deposited on top of a solid samples, very useful to coat flat samples with resist. The sample is placed at the center of a chuck disk and is hold fixed by a vacuum system. The liquid solvent containing the resist is dropped on the sample surface, and the chuck is then forced to rotate at high speed. During the spinning process, the liquid homogenously distributes over the sample surface thanks to centrifugal forces, while the solvent evaporates, leaving the material deposited [117]. The thickness of the deposited material mainly depends on the spinning speed, usually expressed in round per minute (rpm), spinning time and resist viscosity. An empirical formula can be used to determine the film spin-coated as a function of the rotation speed:

$$t \propto \frac{v^{0.4}}{\omega^{0.5}} \tag{7.2}$$

where t is the thickness, ν is the kinematic viscosity of the deposited material and ω is the rotation speed [117]. As an example, **Figure A.7.14** shows a qualitative normalized thickness behavior as a function of the rotation speed at different viscosities.

A drawback of such technique consists in the formation of thicker regions at the sample edges due to the surface tension at the air-resist interface [117]. For this reason, when photoresist or electronic resist is deposited through spin-coating, the lithography is performed at the center of the sample to exploit the homogenous part of the deposited resist.

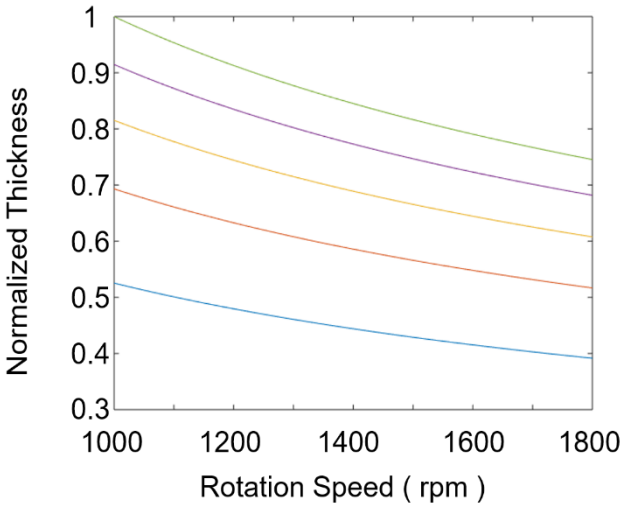

Figure A.7.14 Normalized thickness dependence on the rotation speed of the chuck disk in a spin-coating system for several kinematic viscosity values of the material deposited.

1.4 Physical Vapor Deposition and E-Beam Physical Vapor Deposition

Physical vapor deposition is a deposition technique performed in high vacuum chamber. The material to be deposited is placed in a conductive crucible or spiral usually made of tungsten. Applying a very high current, the crucible is heated up to the material melting point. When the material starts to evaporate, its vapors reach the target sample as shown in the sketch of **Figure A.7.15**, placed on top of the vacuum chamber. The reason of high vacuum values (or low pressure values) in the chamber derives from two needs: (1) the control of the impurities in the air that can contaminate the deposited film composition and (2) the isotropic direction of the melted material vapors in its route towards the substrate. In this last case, it is worth to note the relation [118]

$$N = N_0 e^{-l/L}, \tag{7.3}$$

where N is the number of evaporated particles that did not experience any collision within a distance l from the crucible, L is the distance between crucible and substrate, and N_0 is the total number of evaporated particles. Then the higher the vacuum, the lower the collision

number, finally obtaining a rectilinear evaporation towards the substrate and a uniform film deposition on the substrate/wafer. However, even in ultra-high vacuum conditions (10^{-10} mbar) the evaporation of the deposition material is not perfectly isotropic. This is due to many factors, such as the geometry of crucible, the irregular surface of the melted material, the variation of the vapor pressure of the evaporated material during its motion from the crucible to the substrate, etc. To partially contrast such phenomenon and obtain a homogeneous deposition, the substrate holder is rotated at constant speed [119].

It is worth to mention that tungsten, usually employed as crucible material, reacts with one very common deposition material: aluminum [118]. In this case, small clips of aluminum are placed on a tungsten spiral instead of tungsten crucible, because the spiral can better resist to the aluminum corrosion thanks to the reduced contact area.

Physical vapor deposition presents one main drawback related to the heating system: it allows to deposit material with melting temperature below 1200 – 1500°C. The deposition of material with melting temperature higher than the one allowed by hot crucible system, can be obtained by using an alternative heating system: the electron beam. By using this method, the beam can be precisely pointed on the material and its power can be finely tuned allowing to melt materials characterized by very high melting temperature with also much more efficiency with respect of hot crucible method [118].

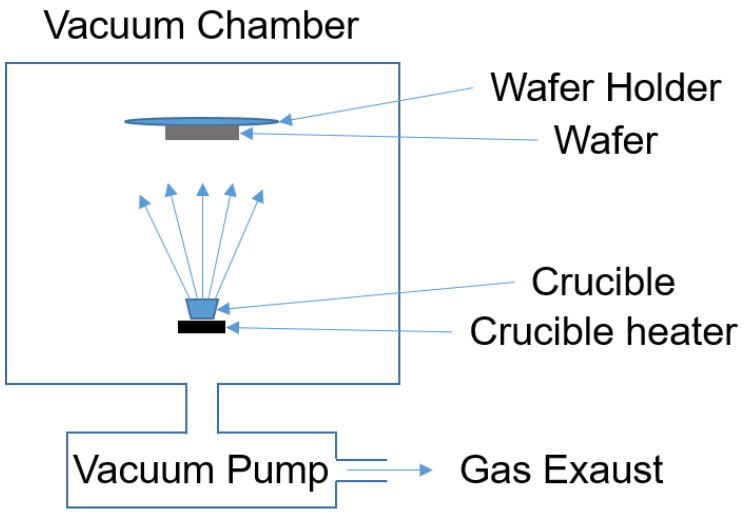

Figure A.7.15 Sketch of a physical vapor deposition system. Inside the vacuum chamber the wafer is fixed on a rotating wafer holder. The crucible containing the material to evaporate is heated up by either electric current passing through the crucible or by an electron beam impinging on the deposition material. The gases inside the chamber are evacuated by using a vacuum pump.

1.5 Electron Beam Lithography

Electron beam lithography is the lithography system chosen for the fabrication of tapered NA pairs because of its extreme resolution and precision. In particular, a Raith 150 two e-beam lithography system has been employed. This instrument is able to produce beam size as small as 2 nm, and a minimum line width of 10 nm. The extremely high resolution of e-beam systems is allowed by the small wavelength of the electrons in the beam. In fact, transferring energies of few keV, the electrons are already characterized by wavelength on the order of tens of Angstrom.

In **Figure A.7.16** is shown a simplified internal scheme of the column in an e-beam system from Ref. [116]. Between the top and bottom extremities of the column high voltage is applied ranging from few keV up to 100 keV. On the top of the column, the electron gun produce electrons that are accelerated by the high voltage applied towards the sample holder plate, the latter able to move with nanometric precision thanks to an interferometric laser control system. In between, alignment coils, condenser lens and apertures are implemented to accurately deflect and focus the beam, and to remove astigmatisms and other spurious effects.

As said in the previous, electron beam is used to pattern an electronic resist film that, once developed, forms a mask on top of a substrate. Unfortunately, the resolution at which is possible to patter the resist film is not in range of tens of Angstrom as potentially allowed by the electron beam, but it suffers of the so called *proximity effect*. Such effect born from the

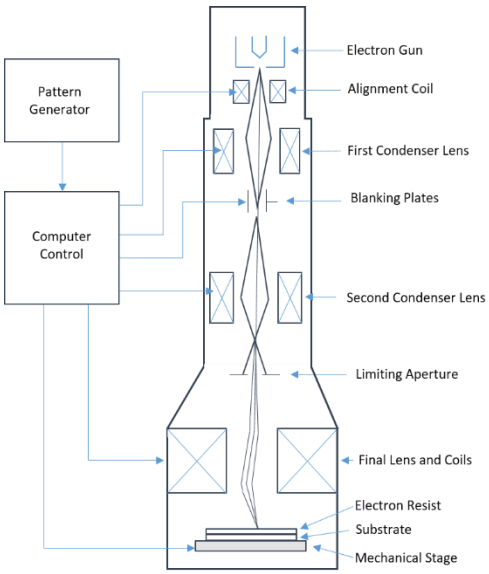

Figure A.7.16 Electron beam lithography column scheme. From the electron gun, at the top of the column, electrons are generated. Thanks to the applied high voltage between electron gun and sample holder stage, electrons are accelerated towards the sample to be patterned. Alignment coil, condenser lens and limiting apertures shape the electron beam to remove beam imperfections. Thanks to a computer control and a pattern generator, the electron beam is properly deviated on the sample resist to perform the lithography.

forward and backward scattering of the electrons inside the resist and substrate materials. In **Figure A.7.17 (a)** is sketched how an electron beam enlarges as a result of the electron scattering: when the very thin electron beam (represented on the top of the sketch by a short black line) reaches the resist film it assumes the shape of an oblong pear. This occurs because the electrons of the resist atoms are able to deviate the electron of the incoming beam, thus increasing the beam size already once inside the resist layer. Furthermore, when the electrons of the beam reach the substrate, they gain high probability to be backscattered, thus increasing even more the exposed area. In **Figure A.7.17 (b)** is reported a Monte Carlo simulation, from Ref. [120], where the trajectories of 100 electrons impinging on a resist film are calculated giving an accurate representation of what actually happen to the electrons entering the sample during lithography.

The forward scattering can be mitigated by using resist layers characterized by low electron density, while the backscattering can be reduced by using light substrate materials (small atomic number). Another and effective method usually employed to reduce the proximity effect is to increase the acceleration voltage. As it can be seen from **Figure A.7.17 (a)**, the oblong pears for three acceleration voltages are superimposed to highlight the difference of

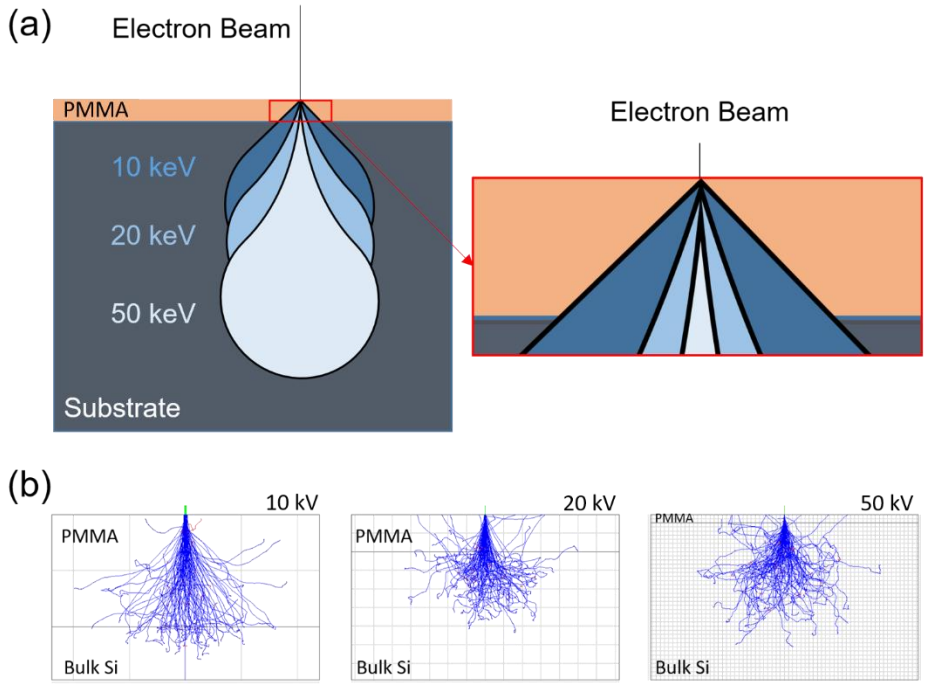

Figure A.7.17 (a) sketch of the electron beam enlargement due to the forward and backward scattering. The tiny electron beam (black line from the top) is enlarged inside the resist layer assuming the shape of an oblong pear. Aas it is possible to observe from the inset, increasing the acceleration voltage, the electron beam inside the resist layer becomes thinner whereas going deeper in the substrate because of the higher energy. (b) Monte Carlo simulation of 100 electrons delivered to a PMMA layer on silicon substrate: at 10 kV the electrons are heavily scattered both in the resist and in substrate, resulting in a pronounced proximity effect; rom 20 kV to 50 kV the electron beam is progressively less enlarged in the PMMA layer leading to less pronounced proximity effect. The Monte Carlo simulations have been performed using the software "Elenctron Interaction with Solids – Single Scattering Monte Carlo simulation." Version 3.0. (c) J. Baussells 2004-2008.

the beam enlargement in the resist layer when the acceleration voltage is varied. As the acceleration voltage is increased the pear become sharper in the resist region, thus limiting the proximity effects. This method allows to greatly reduce the forward scattering, but, at the same time the backward scattering is increased (as shown in the Montecarlo simulation at 20 kV of **Figure A.7.17 (b)**). Nonetheless, the backscattering is distributed in a very large area; consequently, the resist exposed by backscattering did not receive enough electrons to produce molecular changes thanks to the non-ideal contrast γ characterizing the resist film.

1.6 Software Limitation to Resolution

The resolution can be affected also by software constrains. For example, during the pattern design the user is asked to choose the size of the so called *writing field* (e.g. $100 \times 100\ \mu m^2$, $200 \times 200\ \mu m^2$, etc.). Once the desired writing field is selected, the entire pattern is divided in writing fields, for instance if a $100 \times 100\ \mu m^2$ writing field size has been chosen, then an hypothetical pattern of $5 \times 5\ mm^2$ is divided in 2500 writing fields with area of $100 \times 100\ \mu m^2$ each. This is necessary because during the lithography the beam has to be deflected only within a certain solid angle (that determines the maximum writing field size allowed) generally too small to write area larger than as $1 \times 1\ mm^2$. During the lithography, the sample holder stage is moved to align the e-beam with the center of the first writing field to write on the sample. Once completed, in order to write the features of the subsequent writing field, the sample holder stage moves to align the e-beam with the center of the next one, and this process is repeated until the overall pattern is scanned. Each writing field is divided in points at which correspond a certain dose and deviation angle of the beam. Now, independently from the extension of the area chosen for the writing field, the number of points that the software allocates for the beam deviation remains the same because of a limited memory capacity. As a consequence, if the maximum memory allocation possible is e.g. 10.000 positions, then for a line of $100\ \mu m$ in a $100 \times 100\ \mu m^2$ writing field, the distance between two adjacent points in that line results to be $10\ nm$ ($100\ \mu m/10.000$), while if the line is $200\ \mu m$ in length the distance becomes $20\ nm$ and so on. Thus, the smaller the writing field the higher the lithography resolution, and the longer the exposure time. In fact, the processing of small writing field is a very long process and long exposures are considered detrimental for the final result because of the drift of the system parameters, such as beam current, temperature, etc. For this reason, a good trade-off between exposure time and resolution has to be found to correctly choose the most suitable writing field.

1.7 Stitching Effect

It is worth to mention another source of error that may affect the accuracy of lithography especially in our case. As mentioned, the laser controlled stage moves among many writing fields during the lithography. If the stage movement and the electron beam are not perfectly aligned, then stitching errors occurs. In **Figure A.7.18** is shown an example of this effect: the structures were designed at the border between four adjacent writing fields. Because of the non-perfect alignment between the stage movement and the electron beam the final structure resulted misaligned, eventually becoming useless. This problem can be reduced or completely removed by fine aligning the system through the system software procedure called *writing field alignment*.

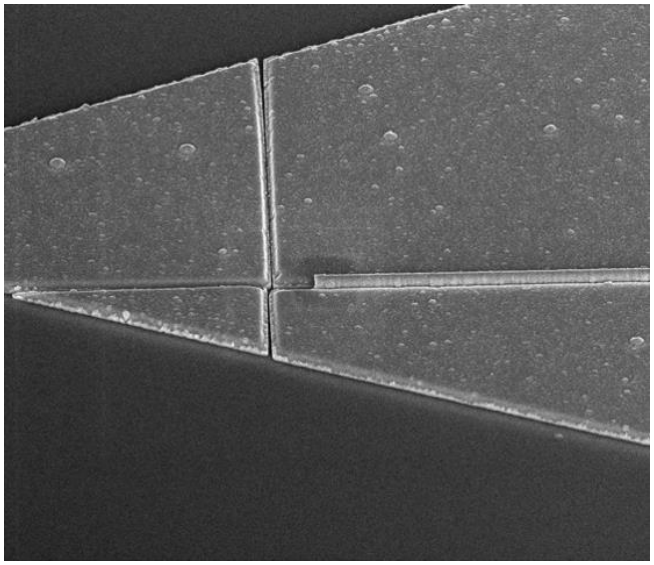

Figure A.7.18 SEM image of an indium tin oxide structure written at the border between four writing fields. Due to a bad alignment between sample holder stage and electron beam, the structure is separated in four sectors, while it was supposed to be a unique structure.

1.8 Charging Effect

Charging effect contributes to the proximity effect due to forward and backward scattering. It occurs when the high resistivity substrate are employed. In this case the electrons coming from the electron gun accumulates in the region exposed and cannot flow because of the insulating nature of the sample. Such accumulation leads to a much higher features than the one expected. In order to avoid this problem, conductive samples are usually employed. If high resistivity substrate has to be used, a thin conductive layer can be deposited over the PMMA layer. In this way, the electrons can flow reducing the charging effect, but the resolution results to be lower with respect of the case of conductive substrate because of the introduction of some scattering events of the electrons colliding with the conductive layer surface.

2 Reflection coefficient calculation at the metallic cylinder extremity

Here is presented the calculation theory of the reflection coefficients at the metallic cylinders end as shown in Ref. [61]. A cylinder of radius r has its main axis laying in the negative z-axis, and its extremity at $z = 0$. Assuming that a radially polarized mode impinges at the wire end from $z = 0^-$ and that the reflection at this end occurs entirely into the same mode, the electric field and the azimuthal magnetic field can be written in cylindrical coordinates as

$$E_\rho(\rho, \phi, z = 0^-) \simeq (1 + R)\frac{\beta}{\omega\varepsilon_0\varepsilon_R(\rho)}F(\rho) \tag{1}$$

$$H_\phi(\rho, \phi, z = 0^-) \simeq (1 + R)F(\rho) \tag{2}$$

with R reflection coefficient, $\beta = n_{\text{eff}}\,\kappa_0$ is the propagation constant of the mode reflecting at the cylinder end, ω frequency in $\mathrm{rad/s}$, ε_0 dielectric constant of vacuum, and $\varepsilon_R = \varepsilon_d$ dielectric permittivity of the surrounding medium when $\rho > r$, and $\varepsilon_R = \varepsilon_m$ dielectric permittivity of the cylinder when $\rho < r$. Finally, the function $F(\rho)$ is defined as

$$F(\rho) = f(x) = \begin{cases} \dfrac{I_1(\psi_m\rho)}{I_1(\psi_m r)}, & \rho < r \\ \dfrac{K_1(\psi_d\rho)}{K_1(\psi_d r)}, & \rho > r \end{cases} \tag{3}$$

whit I_n and K_n modified Bessel, with n order of the function of first (I) and second (K) kind, and

$$\psi_{m,d} = \sqrt{\left(\beta^2 - \kappa_0\varepsilon_{m,d}\right)} = \kappa_0\sqrt{n_{\text{eff}}^2 - \varepsilon_{m,d}}, \tag{4}$$

where $\kappa_0 = \omega/c$, c speed of light in vacuum. These equations allow to retrieve the value of the mode propagation constant and then the value of the effective index felt by the propagating mode, on the lateral curved surface of the cylinder. This can be done by applying the boundary condition

$$\frac{K_0(\psi_d r)\, I_1(\psi_m r)}{K_1(\psi_d r)\, I_0(\psi_m r)} = -\frac{\varepsilon_d\psi_m}{\varepsilon_m\psi_d}. \tag{5}$$

Once retrieved the value of the propagating constant it is possible to calculate the reflection coefficient. First of all, the electric and the azimuthal magnetic field just outside ($z = 0^+$) the cylinder are

$$E_\rho(\rho, \phi, z = 0^+) = \int_0^\infty t(\kappa)\frac{\sqrt{\kappa_0^2\varepsilon_d' - \kappa^2}}{\omega\varepsilon_0\varepsilon_d'}\,J_1(\kappa\, R)d\kappa \tag{6}$$

$$H_\phi(\rho, \phi, z = 0^+) = \int_0^\infty t(\kappa)\, J_1(\kappa\, R) d\kappa \tag{7}$$

where $J_1(\kappa\, R)$ is the first order Bessel function of the first kind and $\varepsilon_d{}'$ is the dielectric permittivity of the dielectric just outside the flat cylinder end that may not be the same as the dielectric material surrounding the cylinder curved walls ($\varepsilon_d = \varepsilon_d{}'$ if the cylinder is surrounded by the same dielectric material). Now, equating the electric fields at $z = 0^-$ and at $z = 0^+$, multiplying both sides for $J_1\,(\kappa'\rho)$ supposing the orthogonality of both free-space ($z = 0^+$) and wire ($z = 0^-$) modes, integrating ρ between 0 and ∞, and finally using the orthogonality of the Bessel function of first kind, one obtains

$$t(\kappa) = (1 + R)\frac{\kappa r \beta \varepsilon_d{}'}{\omega \varepsilon_0 \sqrt{\kappa_0^2 \varepsilon_d' - \kappa^2}}[A_1(\kappa) + A_2(\kappa)] \tag{8}$$

where

$$\begin{aligned} A_1(\kappa) &= \frac{\psi_m I_2(\psi_m r) J_1(\kappa r) + \kappa I_1(\psi_m r) J_2(\kappa r)}{I_1(\psi_m r)\varepsilon_m(\kappa^2 + \psi_m^2)} \\ A_2(\kappa) &= \frac{\psi_d K_2(\psi_d r) J_1(\kappa r) + \kappa K_1(\psi_d r) J_2(\kappa r)}{K_1(\psi_d r)\varepsilon_d(\kappa^2 + \psi_d^2)}. \end{aligned} \tag{9}$$

Similar procedure for the magnetic field, where in this case the fields at $z = 0^-$ and $z = 0^+$ are both multiplied by $F(\rho)\rho/\varepsilon_R(\rho)$. Finally, the reflection coefficient can be calculated as

$$R = \frac{1 - U}{1 + U} \tag{10}$$

with

$$U = \frac{\int_0^\infty \frac{2\kappa\beta\varepsilon_d{}'}{\sqrt{\kappa_0^2\varepsilon_d' - \kappa^2}}\,[A_1(\kappa) + A_2(\kappa)]^2 d\kappa}{\frac{I_1(\psi_m r)^2 - I_0(\psi_m r) I_0(\psi_m r)}{\varepsilon_m I_1(\psi_m r)^2} - \frac{K_1(\psi_d r)^2 - K_0(\psi_d r) K_0(\psi_d r)}{\varepsilon_d K_1(\psi_d r)^2}}. \tag{11}$$